eXPRESS Polymer Letters Vol.8, No.3 (2014) 142
Available online at www.expresspolymlett.com
DOI: 10.3144/expresspolymlett.2014.17

Editorial corner – a personal view
Carbon dioxide 'management' by polymers

J. Karger-Kocsis[*]

MTA–BME Research Group for Composite Science and Technology and Department of Polymer Engineering, Faculty of Mechanical Engineering, Budapest University of Technology and Economics, Műegyetem rkp. 3., H-1111, Budapest, Hungary

Carbon dioxide (CO_2) is the major 'greenhouse' gas, responsible for global climate warming. Unfortunately, its emission will further increase in the following two decades which fuels the already existing public concerns. Major sources of the CO_2 emissions are the biomass and among the anthropogenic ones, the power plants fired by fossil fuels. Therefore the sequestration (ab- and adsorption processes to produce CO_2 in high purity) and utilization of CO_2 are actual and challenging tasks of great importance.

As capturing media of the chemical absorption/regeneration processes of the flue gases other polymer-based ab- and adsorption materials (liquid-like materials containing polyetheramine-grafted nanoparticles, polymeric ionic liquids, (micro)porous organic polymers (DOI: 10.1002/pi.4407), solid microporous carbons from polymer-containing precursors) than the present amine-based solvents, are explored. They offer lower vapor pressure, less corrosiveness, improved chemical stability and easy regeneration compared to the state-of-art monoethanolamine. Polymer-based membranes with high selectivity are other tools for efficient CO_2 separation.

However, CO_2 may be a valuable chemical feedstock, especially for polymer synthesis. Owing to its chemical inertness, it has to be combined with highly reactive reagents under proper conditions. The pioneering work in this field has to be credited to Inoue et al (1969) who produced poly (propylene carbonate) (PPC) using CO_2 and propylene oxide. PPC is biocompatible and biodegradable, and today already commercially available. Its properties resemble to those of low density polyethylene and plasticized polyvinyl chloride. To synthesize really alternating PPC copolymers with high molecular mass, and to improve their resistance to thermal degradation are, however, still open issues. That is the reason why ongoing research efforts are dedicated to the synthesis of various CO_2 containing co- and terpolymers, which are aliphatic polycarbonates. As comonomers, cyclohexene oxide, oxetane, ε-caprolactone, epichlorohydrin, glycidyl ether derivatives have already been tried (DOI: 10.1021/ma3019574 and 10.1021/ma400090m). It is worth of mentioning that inorganic polymers are also involved in the CO_2 'immobilization': Just one example is the hardening/silicification process of water glass (DOI: 10.1016/j.eurpolymj.2007.01.010), widely used in building and construction.

There are a lot of opportunities to contribute to the sequestration and utilization of CO_2. In the case of the latter the most straightforward is to focus on polymer synthesis (polycarbonates, polyurethanes, polyureas) and modification of the resulting polymers to meet the requested performance. This may result in valuable contributions to the fight against global warming and to the reduction of mankind's 'carbon footprint' – so, why not to make your own homework?

Prof. Dr. Dr. h.c. József Karger-Kocsis
Editor-in-Chief

[*]Corresponding author, e-mail: karger@pt.bme.hu

eXPRESS Polymer Letters Vol.8, No.3 (2014) 143–153
Available online at www.expresspolymlett.com
DOI: 10.3144/expresspolymlett.2014.18

Light-controlled drug releasing polymer films combining LbL self-assembly and host-guest interactions

J. Li[1], *L. He*[1], *J. Wang*[1], *Z. T. Zhang*[1], *J. Shi*[1], *X. Z. Zhang*[3], *Y. P. Cao*[1*], *Y. Chen*[1,2]

[1]Institute for Interdisciplinary Research & Key Laboratory of Optoelectronic Chemical Materials and Devices of Ministry of Education, Jianghan University, 430056 Wuhan, China
[2]Département de Chimie, Ecole Normale Supérieure, 24 Rue Lhomond, F-75231 Paris Cedex 05, France
[3]Key Laboratory of Biomedical Polymers of Ministry of Education & Department of Chemistry, Wuhan University, 430072 Wuhan, China

Received 24 August 2013; accepted in revised form 14 October 2013

Abstract. By combining LbL (layer-by-layer) self-assembly approach and host-guest interactions, a unique multilayer film was constructed and employed for a light-controlled drug release system. The drug molecules can be loaded and released into the resulting polyelectrolyte multilayers containing azobenzene (Azo) function groups by using the irradiation of visible light and UV light alternately. The photo-sensitivity of the multilayer films was studied through UV-vis spectrum, fluorescence spectrum and confocal microscopy. The target molecules could be rapidly released from the multilayers after 300 W UV light irradiation for 20 minutes. Moreover, they could be readsorbed into the multilayers uniformly when illuminated under the 300 W visible light for 10 minutes confirmed by the observation of confocal microscopy, and the readsorption ratio exceeds 100% evidenced from UV–vis spectroscopy. After several cycles of the above-mentioned process, the multilayer films show good fatigue resistance. All these results indicate the photo-sensitivity and high-efficiency of the multilayer films, which have great potential in controlled drug delivery platform and biomedical applications.

Keywords: *coatings, layer-by-layer, host-guest interactions, light response, drug delivery*

1. Introduction

In the past decade, supramolecular chemistry has attracted more and more attention and gradually penetrated into various areas of material and biomedical science [1–3]. The supramolecular system based on host-guest interactions have seen a significant breakthrough, which was shown to be partially successful for drug release [4], biological sensors [5], optically controlled catalytic system [6], molecular shuttles [7], hydrogels [8], and micelles and vesicles [9]. Particularly, photo-controlled molecular recognition of cyclodextrin (CD) with Azobenzenes (Azo) has been widely used for host-guest inclusion compound. Cyclodextrin, a typical host molecule, is a kind of polysaccharides with good biocompatibility and water-solubility. As one of the most widely used guest molecule to cyclodextrin, Azo constitute a class of light-responsive compounds that can undergo *trans-cis* photoisomerization in response to UV and visible (Vis) light [10, 11]. It is well-known that the apolar and rodlike *trans*-Azo can form a stable inclusion complex with CD, while the bent and polar *cis*-Azo cannot. This process is fully reversible under irradiation with UV and Vis light alternately. Reports about the reversible and photo-responsive supramolecular system have come to the fore [6, 12–14]. For example, Zou *et al.* [15] first put forward supramolecular type amphiphilic molecule concept and prepared a series of rotaxane-like supramolecular amphiphiles. Alter-

*Corresponding author, e-mail: softmatter@163.com

nating irradiation with UV and Vis light allows for reversible sliding of α-CD along the surfactant, leading to the formation of rotaxane-like vesicles. Based on this principle, light-responsive host–guest assembly and disassembly between Azo and CD hold great potential to design a reversible drug delivery profile [16, 17].

Layer-by-layer (LbL) self-assembly approach is particularly well-suited for fabricating functional multilayer thin films with ultrafine nanometer-scale structure for use as drug delivery vehicles [18–21]. The traditional means of loading drugs on layers of LbL platform always uses physical adsorption or chemical bonding. However, these methods of loading drugs have a common drawback: drug loading and release is irreversible. This is a critical problem in LbL multilayers for drug delivery. Therefore, it's desired to devise a reversible LbL-based system to manipulate the drug release in a more controllable manner. In the past decade, the pioneering work on LbL assembly with supramolecular interaction has been established by Ikeda *et al.* [22]. Subsequently, Smith *et al.* [23] have reported that loading small-molecule drugs on the layers of LbL-based system using supramolecular interaction. On another front, the light-induced drug release from a LbL-based system is the most elegant way to combine reversibly and efficiency, because light as an attractive stimulus can be applied rapidly, remotely, and locally [24, 25]. While numerous well-established photo-responsive LbL-based systems are available [26, 27], their applications in drug release based on polyelectrolyte multilayers or coatings is scarce and little progress.

Thus, all mentioned above inspires us to develop a reversible light-controlled drug releasing thin film by combining polyelectrolyte LbL technique and host-guest interactions, which is capable of addressing the demand for small-molecule delivery with highly controlled release kinetics. Our basic approach is to conjugate drugs with α-CD through chemical bonding due to the availability of functional groups on their surface. Meanwhile, by introducing the Azo to the layers of LbL system, multiple drugs or functional groups can be loaded into the Azo polymers directly and mildly *via* host-guest interactions. Thus, α-CD–drug complexes will be released and loading from the polyelectrolyte multilayers under alternating irradiation with UV and Vis light. Moreover, the usefulness of cyclodextrin conjugated with drugs offers a simple method to increase drugs solubility, bioavailability, stability. Herein, α-CD modified rhodamine B (α-CD-RhB) was selected as a drug model. We believe that the ability of α-CD to complex with multiple drugs gives these LbL films available versatility to many traditional drug delivery systems [28].

Previously, we have demonstrated that an intelligent 'PnP' (Plug and play) polyanionic template driven by the photo-switchable host-guest interactions was first prepared for the light controlled loading/unloading of small molecule drugs. We have shown that the antineoplastic drug and other functional moieties such as target ligand can be simultaneously released and loaded into the template by using UV and Vis light irradiation alternately [29]. Herein, we describe polyelectrolyte LbL multilayers based on Poly(diallydimethylammonium chloride) (PDAC) and azo-modified polyacrylic acid (PAA-C_6-Azo) loaded α-CD-RhB *via* host-guest interactions as a drug carrier that can reversibly capture and release small drugs. From the investigation, α-CD-RhB could be rapidly released from the multilayers after 300 W UV light (365 nm) irradiation for 20 minutes and they could be adsorbed into the substrate uniformly when illuminated under 300 W Vis lamp (455 nm) for 10 minutes. Moreover, a 'forever'-pattern was presented onto this LbL film surface *via* area-selective release and the obtained results may be of great potential for applications in biomedical device based on well-defined nano-sized materials surface of arbitrary topography. Light-responsivity of the host-guest interactions based on Azo and α-CD-RhB and schematic illustration of α-CD-RhB-loading polyelectrolyte multilayers are illustrated in Figure 1. Multilayers are denoted as (PAA-C_6-Azo/PDAC)n where *n* is the number of deposited bilayers.

2. Experimental details

2.1. Materials and characterization

Acryloyl chloride (AC), rhodamine B (RhB) and 3-aminopropyltriethoxysilane (APTES), PDAC (poly (diallydimethylammonium chloride) solution, M_v = 20 000–35 000, 20%) were obtained from Shanghai Aladin Co., Ltd. (China) and used directly. N-(3-dimethylaminopropyl)-N′-ethylcarbodiimide hydrochloride (EDC.HCl, 98.5%), 1-azobiscyclo-hexanecarbonitrile (ABCN), N,N′-dimethylformamide (DMF), 1,4-dioxane and dimethyl sulfoxide (DMSO)

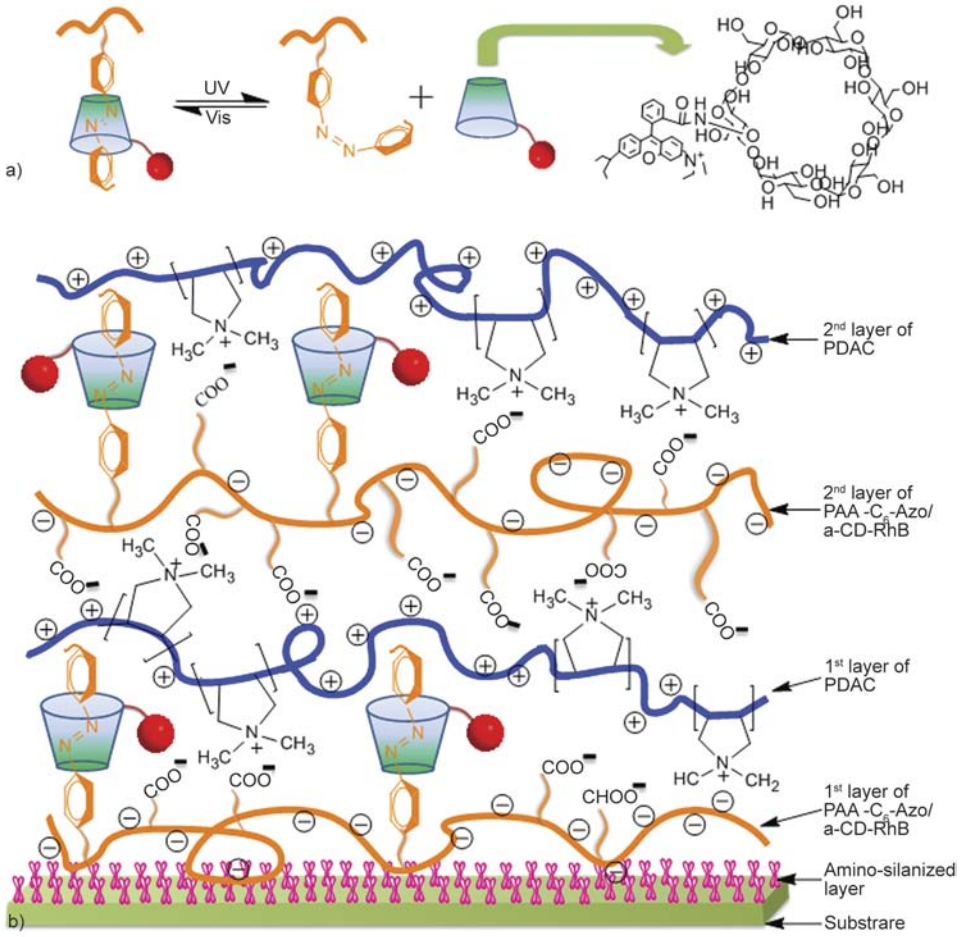

Figure 1. (a) Photoresponse of the host-guest system of Azo group and α-CD-RhB. (b) Schmatic representation of polyelectrolyte multilayers loaded with α-CD-RhB.

were purchased from Aldrich. DMF was azeotropically distilled with benzene for dehydration and then distilled under vacuum. DMSO and 1,4-dioxane were previously dried with molecular sieves. ABCN was recrystallized from methanol before use. All other chemicals were used without further purification. All absorption and fluorescence measurements were performed on solutions in 1 cm^2 quartz cuvettes. Absorption spectra were measured on a Shimadzu UV-2550 spectrometer. Fluorescence spectra were measured on a Photon Technologies International LS-55 luminescence spectrometer. Solutions were made into 1 mg/mL aqueous. The fluorescence images of multilayer films before and after UV light irradiation were viewed using confocal laser scanning microscopy with BD Laser at 543 nm.

2.2. Preparation of poly (acryloyl chloride) (PAC)

PAC was synthesized according to the literature [30]. Briefly, Acryloyl chloride (20 mL), dry 1,4-dioxane (20 mL), and ABCN (0.668 g) were added into a flask under N_2 protection. The flask was sealed and then heated in an oil bath (50°C) for 14 h. The polymer was precipitated by adding petroleum ether (100 mL), collected by filtration, and washed twice with petroleum ether. The product was dried at 60°C under vacuum for 48 h.

2.3. Preparation of PAA-C_6-Azo

PAA-C_6-Azo was prepared as described elsewhere [31, 32]. PAC (0.3 g, 0.0033 mol), triethylamine (0.56 mL, 0.0040 mol), and 2-[4-(4-ethoxyphenylazo) phenoxy] ethanol (whose amount was determined by the required degree of functionalization) were dissolved in anhydrous DMF (33 mL). The mixture was stirred at room temperature for 12 h under N_2 protection. Then suitable amount of water was added into the mixture and stirred for 10 min. The product was precipitated from HCl water solution (0.01 mol/L), collected by filtration, washed several times with water, and dried under vacuum.

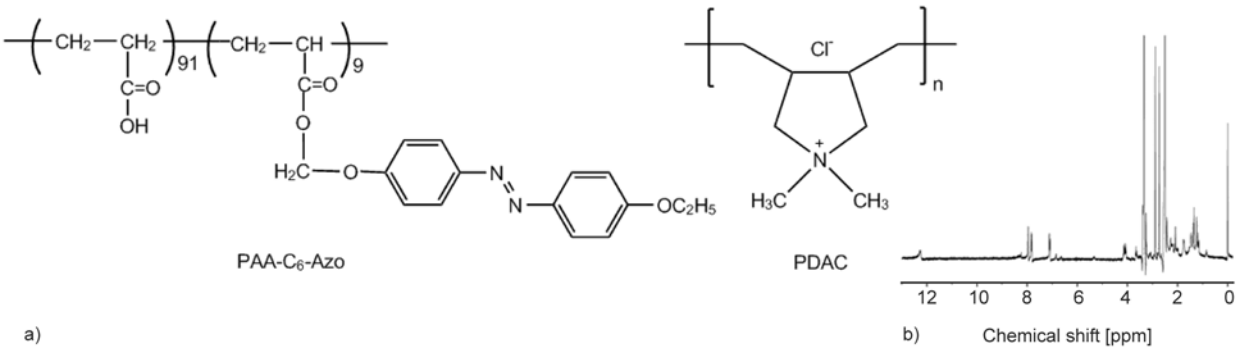

Figure 2. (a) The molecular structure of linear polymer PAA-C_6-Azo and polypositive charge polymer PDAC. (b) The ^{1}H NMR spectra of PAA-C_6-Azo.

The polymer was further purified by dissolving in THF and precipitated from petroleum ether, collected by filtration, and washed twice with petroleum ether. The final product was dried at 70°C under vacuum for 24 h. The molecular weight of PAA-C_6-Azo was determined by GPC measurement (M_n: ~28.6 kDa, PDI: 1.98), and the degree of modification (the number of Azo molecules to one acrylic acid unit of PAA) was calculated to be 9 mol% by ^{1}H NMR as shown in Figure 2b.

2.4. Synthesis of α-CD-rhodamine B (α-CD-RhB)

α-CD-RhB was synthesized according to our previous paper [29]. Briefly, 60 mg 3-NH_2-α-CD and 148 mg RhB were dissolved in 5 mL deionized water, after the solution's pH value was adjusted to 5, 80 mg EDC was added into this solution and stirred for 24 h at room temperature. The reaction mixture was poured into a large excess of acetone to recover the product. The residue was washed with acetone four times and dried for 2 days under vacuum drying.

2.5. Inclusion complex formation

The drug complex of PAA-C6-Azo/α-CD-RhB was prepared as follows: 32.2 mg ($1.1\cdot10^{-3}$ mmol) PAA-C_6-Azo was respectively dissolved in 40 mL H_2O (a suitable amount of sodium hydrogen carbonate was added into the solution to promote the solubility of PAA-C_6-Azo). After completely dissolving, the pH values of the solution were adjusted to be 7.0 by adding a few drops of HCl dilute solution. Then 40 mg (0.0286 mmol) α-CD-RhB was respectively added under ultrasonic condition at room temperature. The mixtures were stirred overnight at room temperature and then dialysis against uncomplexed α-CD-RhB for 48 h in a dialysis tube.

2.6. Substrate preparation

Quartz slides were used as substrates for the UV-vis absorption. A quartz substrate was immersed into a fresh piranha solution (30% H_2O_2:98% H_2SO_4 (v/v) =1:3; CAUTION: Piranha solution is a very aggressive, corrosive solution, and appropriate safety precautions should be utilized, including the use of acid-resistant gloves and adequate shielding) and heated until no bubbles were released. The substrate was rinsed carefully with deionized water and dried with nitrogen. The cleaned quartz slide was treated in 2% (v/v) APTES/95% ethanol solution for 20 min, and then was dehydrated at 110°C for 1 h to obtain the amino-silanized quartz slide.

2.7. PAA-C_6-Azo/PDAC multilayer fabrication and characterization

Linear polymers we used in the experiments are shown in Figure 2a. First, 32.2 mg ($1.1\cdot10^{-3}$ mmol) PAA-C_6-Azo and 80 mg ($4.0\cdot10^{-4}$ mmol) PDAC were respectively dissolved in 40 mL H_2O (a suitable amount of sodium hydrogen carbonate was added into the solution to promote the solubility of PAA-C_6-Azo). After completely dissolving, the pH values of the solution were adjusted to be 7.0 by adding a few drops of HCl dilute solution. Next, a freshly treated quartz wafer was alternately dipped in the PAA-C_6-Azo solution and the PDAC solution each for 10 min. After each dipping, the wafer was washed with enough Milli-Q water for 30 s.

2.8. The extraction of α-CD-RhB from multilayers

It has been reported [33] that the release of small molecules from the LbL film through pH sensitive, ion strength, thermo-sensitive and so on. Here we use the UV light to control the release and uptake of

the model molecule. The UV irradiating light was from a high-intensity 365 nm UV lamp equipped with 5 in. diameter filter. The intensity of the lamp was 8000 μW/cm^2 at distance of 15 in. A 300 W xenon lamp equipped with a filter (λ = 455 nm) was used as visible light source. The sample was placed 15 cm away from the lamp. The surrounding temperature of the samples was controlled at 25°C using a cold plate.

2.9. The reversibility of unloading/loading behavior

To examine the reversibility of unloading/loading behavior, a quartz substrate with 12 assemble monolayers was transferred into a 20.0 mL water and then irradiated by UV light. After 20 minutes of UV light irradiation, the sample was placed into a cuvette with 20.0 mL of α-CD-RhB aqueous solution (0.38 mmol) and then irradiated by visible light for another 10 minutes. The unloading/loading curve of α-CD-RhB at λ = 566 nm was monitored for more than 8 cycles of UV/visible light irradiation.

3. Results and discussion

3.1. The characterization of the host-guest interactions

UV-vis spectroscopy is a widely applicable means for charactering the formation or dissociation of a host-guest system [34, 35]. We firstly carried UV-vis studies in aqueous solution to understand the inclusion complex of Azo with α-CD-RhB, as shown in Figure 3a. Distinct inclusion complex effects on absorption were encountered for dye molecules exhibiting host-guest stoichiometry-dependent shifts in their spectra. In the same concentration (7.8·10^{-6} M), the maximum absorbance of the RhB, α-CD-RhB and host-guest system (Azo/CD-RhB) are located in 552, 563 and 565 nm respectively, which means that the three solutions tagged by RhB happen red shift gradually. We can observe the difference by comparing the molecular structure of RhB with α-CD-RhB. For α-CD-RhB, the carboxyl group in RhB turns into amido linkage, and chromophores are unchanged but the auxochromes vary, leading to the obvious decrease for the energy of the electronic transition. Therefore, the maximum absorbance undergoes red shift. It has been established that the formation of the host-guest system would affect the maximum absorbance as well as the characteristic absorption [36]. With the addition of the guest molecule, the maximum absorption wavelength of the guest molecule (Azo function molecule) is red shifted and its absorbance increases, reflecting that the Azo functional groups have dropped from hydrophilic conditions into the hydrophobic environment. These data provide enough evidence for the formation of supramolecular system based on Azo and α-CD [37]. In case of the formation of the host-guest interactions, the environment of the chromophoric group has changed and the polarity becomes weaker. As a result, the hydrophobic environment leads to the maximum absorbance red shift as well [38].

Rhodamine B emits strong fluorescence in the specific excitation wavelength (λ_{Ex} = 550 nm). This directly provides us with the opportunity of detecting the characteristic emission wavelength of RhB, α-CD-RhB and Azo/α-CD-RB solution in the same concentration using fluorescence spectrum. Figure 3b shows their maximum characteristic emission wavelengths are located in 575, 579 and 582 nm,

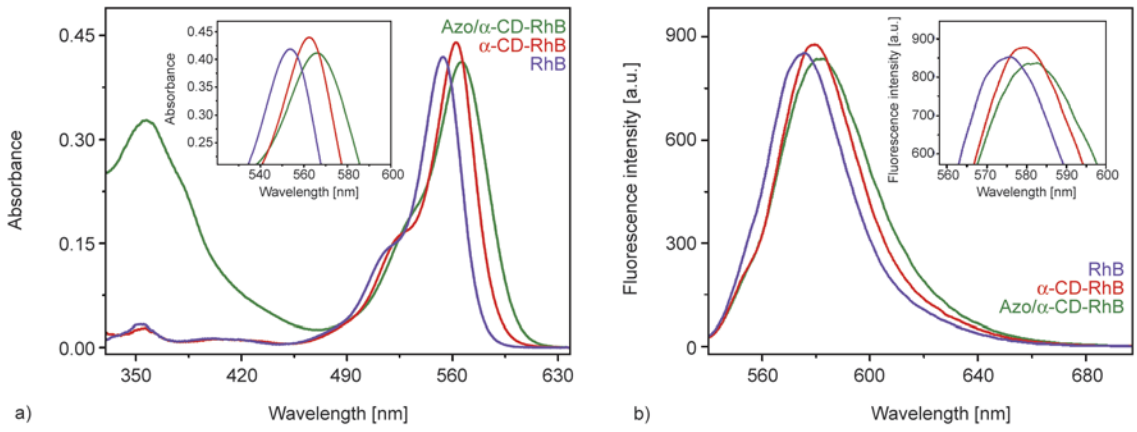

Figure 3. The host-guest interaction characterized by UV-vis spectroscopy (a) and fluorescence spectrophotometer (b).The inset shows the magnification of the characteristic absorption. The violet line is the absorption curve of RhB; the red line is the adsorption of α-CD-RhB and the olive one stands for the supramolecular Azo/α-CD-RhB.

indicating gradual red shift for the three solutions. Obviously, the fluorescence spectrum result is consistent well with that of UV-vis spectroscopy. In addition, the result can confirm our conclusion above that the formation of the amido bond change the electronic environment. As described by Wagner, the cause of further red shift for the host-guest system and LbL film should be attributed to the surrounding from aqueous solution state to dry LbL film after nitrogen blow [39]. Overall, although there is no direct proof for formation of a true host-guest inclusion complex, the data observed by fluorescence spectrum, as well as the results from UV-vis spectroscopy, does provide compelling indirect evidence that such inclusion complex based Azo and α-CD-RB is indeed formed.

3.2. Fabrication of multilayer films *via* electrostatic interaction

As well-known, electrostatic interaction is the most common driving force to build self-assembly multilayer films [40]. Water-soluble and multiple charge are required for the components to construct the electrostatic LbL multilayers. However, strict matching in position between the charges is not necessary, so it is unavoidable to introduce more than one building components into multilayer film with specific sequence [41]. In our work, photosensitive multilayers were prepared by alternately deposition of polyanion PAA-C6-Azo and polycation PDAC in aqueous. The stepwise self-assembly of the multilayers is characterized by UV-vis spectroscopy, as shown in Figure 4a. The absorbance maximum of α-CD-RhB in the film at 566 nm is taken as the reference for monitoring the film growth. A linear increase with the number of layers is observed, which indicates this is a regular deposition process. Additionally, the absorption bands between 300 and 370 nm is mainly attributed to the π-π* transition of the Azo groups in PAA-C_6-Azo. Moreover, we observe a similar linear relationship between the peak intensity of Azo at 355 nm and number of bilayers. It should be noted that the α-CD-RhB-loading multilayer desorbs abundantly during the deposition of the PDAC layer. After further deposition of an additional PAA-C_6-Azo/α-CD-RhB layer, the characteristic absorbance of α-CD-RhB increase again. A possible explanation for this phenomenon could be related to the ionic strength of the PDAC solution [28, 42].

We have further investigated the self-assembly process from fluorescence spectrum (Figure 4b). It is clear seen that quartz/multilayers as well as solution of the host-guest system emit characteristic fluorescence, which are similar to RhB, whereas quartz without self-assembly are not fluorescent (λ_{Ex} = 550 nm). This confirms α-CD-RhB-loading linear polymers have been successfully assembled on the surface of quartz wafers. Further, as the number of layers increases, the fluorescence intensity for the quartz slide also grows (data not shown). These results are in good agreement with that of UV-vis spectroscopy. However, in comparison with the solution of the supramolecular system, the characteristic emission peak for Azo/α-CD-RB has moved from 580 to 587 nm. The reason for this red shift

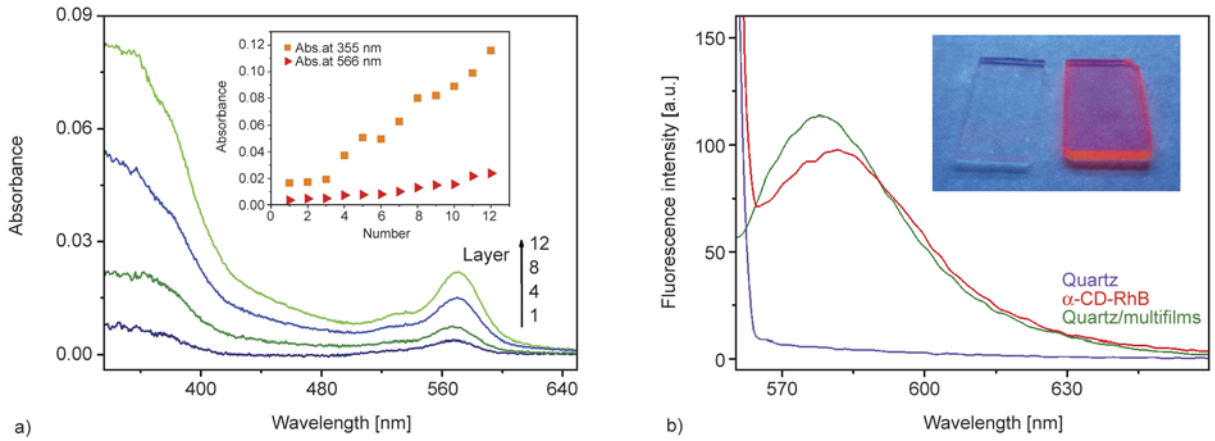

Figure 4. (a) The multilayers assembled on a quartz substrate and measured after each deposition treatment. The inset scatter diagram shows growth tendency of Azo (orange) and RhB (red), respectively. (b) Fluorescence spectra of Quartz, α-CD-RB solution and Quartz/multilayers (α-CD-RhB-loading 8-bilayer multilayers assembled on the quartz slide). The inset shows the photographs of a quartz slide before (left) and after (right) assembly treatment under a 28 W UV light (365 nm) in a dark environment.

may be the change of surrounding environment from dryness to aqueous, so does the polarity [43, 44].

3.3. Light-triggered release and loading

The multilayers were observed with confocal laser scanning microscopy (CLSM) (Nikon C1-si, BD Laser at 543 nm). It is clear seen that the red fluorescent surface of the $(PAA\text{-}C_6\text{-}Azo/PDAC)_8$ film confirmed α-CD-RhB is loaded on the layers before the irradiation of the UV light (Figure 5a). While the fluorescence almost disappears after irradiation with UV light (365 nm) for 20 minutes, indicating the release of α-CD-RhB from the films (Figure 5b). Before release, an average surface coverage of 0.91 drug molecules per nm^2 is calculated from the Beer–Lambert law, while the value drops below 0.05 after release. This reveals that the release process is complete and obvious, which is attributed to disassemble of the specific host-guest interactions between Azo and α-CD-RhB upon UV irradiation.

Further, the surface morphology of multilayer films has been characterized by scanning electron microscopy (SEM). The SEM image of the α-CD-RhB-loading 8-bilayer film shown in Figure 5b illustrates a coarse surface morphology and some massive substance is observed, which may be the results of uniform assembly. After UV light irradiation, the α-CD-RhB-released multilayer shows a smooth and uniform surface coverage. We assume the irregular topography surface is a result of the fast assembly process. Therefore, the linear Azo polymers get behind in adjusting their configurations, but it definitely deserves further investigation, which is outside of the scope of this work. After illumination of

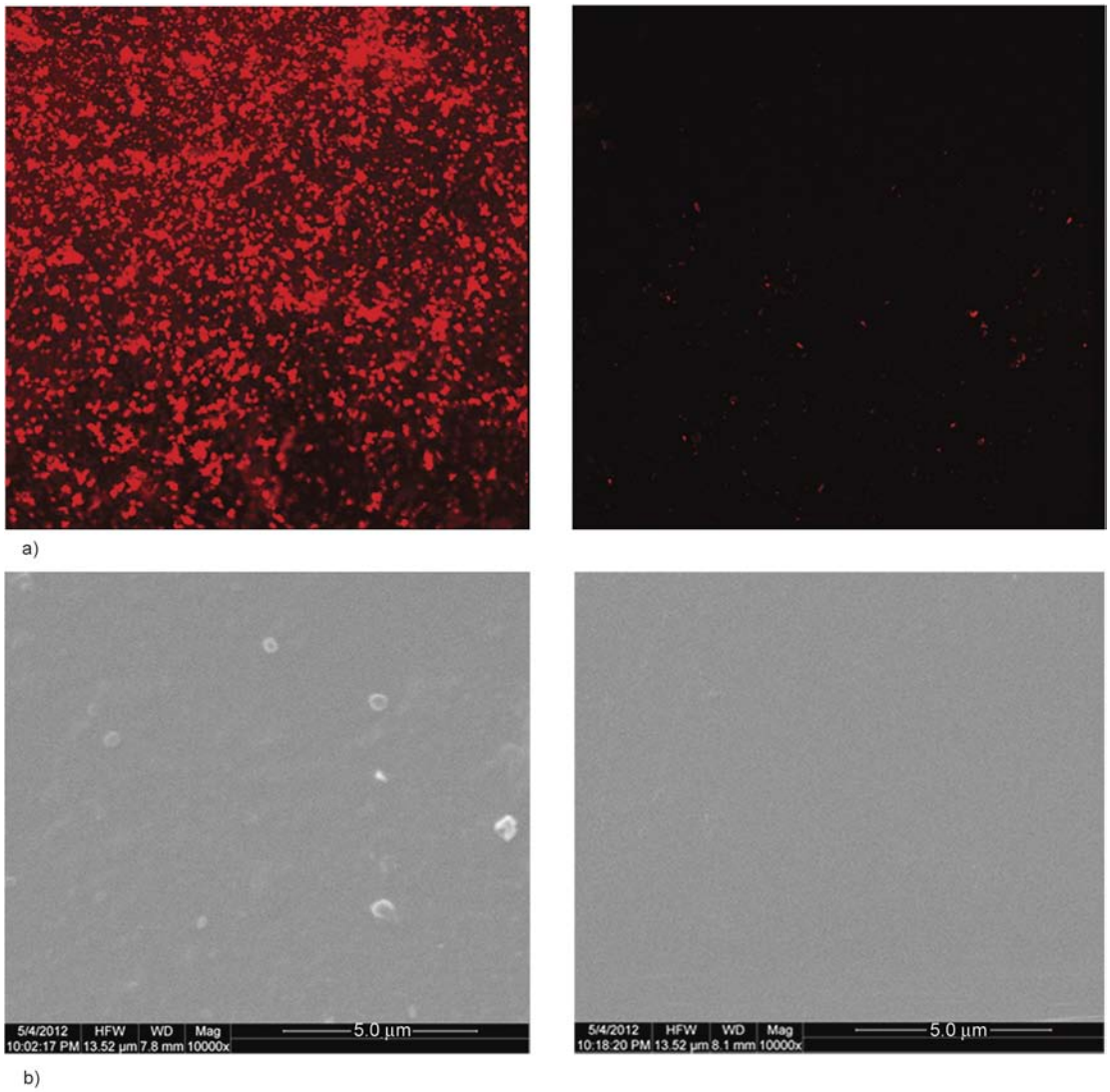

Figure 5. (a) CLSM images of multilayer films before (left) and after (rihgt) UV irradiation (the scale bar is 100 μm). (b) SEM images of multilayers before (left) and after (right) UV irradiation (the scale bar is 5 μm).

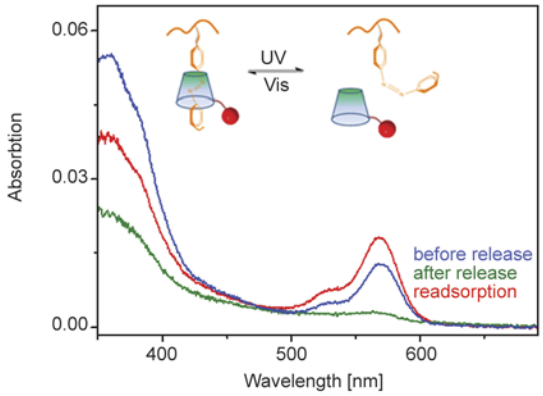

Figure 6. Absorption spectra of the α-CD-RhB loading multilayers before and after UV light irradiation for 20 minutes, then Vis light irradiation for 10 minutes in 40 mL α-CD-RhB aqueous solution for loading (1 mg/mL).

the UV light, the photoisomerization of the Azo resulted in the release of α-CD-RhB from the film, then the surface become smooth and even.

UV-vis spectrum was employed to monitor the release and reloading of multilayers (Figure 6). Application of 20 min UV irradiation induces a clear and rapid loss of dye from the 8-bilayer film. The absorbance of multilayer at 568 nm is about 0.026 before release, while the absorbance almost disappears after UV light treatment. It can be concluded that the loaded α-CD-RhB is almost completely washed out. For reloading studies, the film was immersed into 1 mg/mL of α-CD-RhB solutions for 10 min Vis light (455 nm) irradiation. Surprisingly, irradiation of Vis light for the multilayers after released introduces much more drug molecules move back into the multilayers. This is likely to be caused by a small number of free Azo molecules without assembling with α-CD-RhB during the fabrication of multilayers [32]. It should be mentioned that drugs release rate for PAA-C_6-Azo/PDAC film is rapid. 98 wt% of α-CD-RhB is released within 50 min for 20-bilayer film under UV irradiation, while 10-bilayer film takes 28 min to release of ca. 99% drugs. Hence, it is difficult to get detailed release rate, but the release trends can be attained. For 20-bilayer film, after 6 min of UV light irradiation, the release percentage starts to increase sharply, which raises to ca. 50% after 22 min. 88% of the loaded drugs is released in 40 min under UV irradiation and it reaches ca. 98% in 50 min. These results strongly demonstrate that the film exhibits a rapid response for light-triggered release.

3.4. Reversible loading and release

In order to investigate the potential of the α-CD-RhB-loading multilayers as a reversible light-triggered release platform, a quartz substrate with 8 assembled bilayers was transferred into 20.0 mL water and then irradiated by UV light. After 20 minutes of UV light irradiation, the sample was placed into a cuvette with 20.0 mL of α-CD-RhB aqueous solution (0.38 mM) and then irradiated by visible light for 10 minutes. The absorbance of (PAA-C_6-Azo/PDAC)$_6$ film was recorded, as shown in Figure 7. As expected, the multilayers exhibit good photo-responsive properties. It is shown that the absorption efficiency of the PAA-Azo/PDAC film is almost unchanged after 16 times of release and loading under irradiation with UV and Vis light alternately. This result demonstrates that the film is stable in these loading and release conditions, and can be used for a reversible drug delivery system.

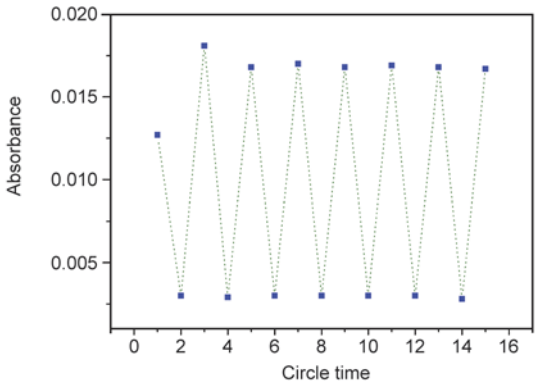

Figure 7. The cyclic absorbance features of (PAA-C_6-Azo/PDAC)$_6$ multilayer film at 566 nm as a result of the cyclic loading and release.

3.5. Surface patterning

Finally, to further verify the ability of light-sensitive of the LbL deliver platform, we presented a pattern onto the LbL film surface *via* area-selective release. Demonstration of the LbL film in area-selective release was conducted using a 'forever'-shaped mask (Figure 8b). The procedures of pattern formation are described as follows. Briefly, a quartz slide with as-prepared (PAA-C_6-Azo/PDAC)$_{20}$ film was transferred into a cuvette with 20.0 mL deionized water at room temperature. Next, a 'forever'-shaped mask was also immersed in water and positioned on the film. Then, they were irradiated by UV light for 40 minutes, followed by a brief wash-

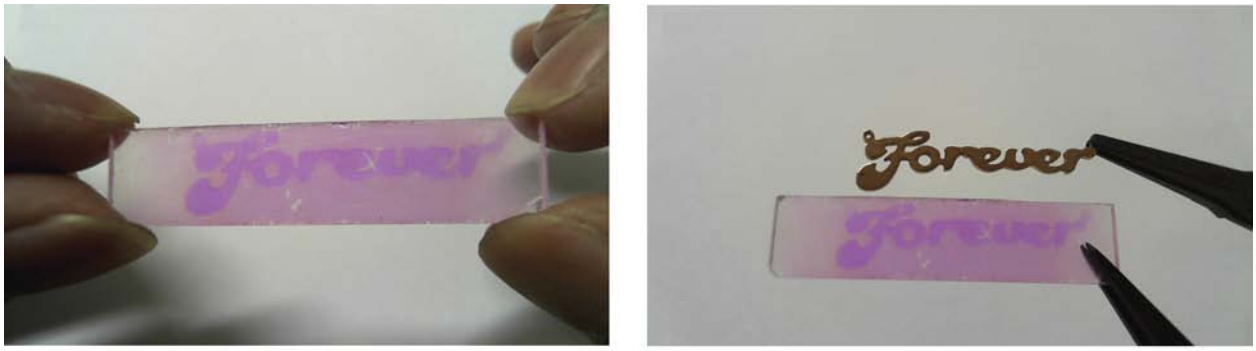

Figure 8. The patterned photograph of (PAA-C_6-Azo/PDAC)$_{20}$ multilayer film as a result of local release. (a) The well-patterned 'forever' on a quartz slide. (b) The contrast between the mask and the resulting pattern.

ing with neutral water and drying under a nitrogen stream. This process yielded a fluorescent display of 'forever'-shaped pattern. As seen clearly in Figure 8a, The UV irradiation areas are almost colourless, while the UV-free parts are red, indicating the area-selective release of α-CD-RhB from the LbL film. The well-patterned 'forever' is distinct with a clearly outline, which attributes to the photo-sensitivity of the multilayer film for release.

4. Conclusions

In summary, we have demonstrated a polyelectrolyte polymer film by combining LbL self-assembly and host-guest interactions for light-controlled drug release. The multilayer film based on electrostatic interactions between PDAC and PAA-C_6-Azo showed high stability under neutral conditions. Compared with traditional drug-loading methods of using physical uptake and chemical bonding, our supramolecular drug-loading approach of the LbL-based film exhibits convenient drug loading, ideal bonding strength, and light-controlled drug release. Moreover, the resulting film can catch and release multidrug, or other functional groups, as exemplified here by loading and release of α-CD-RhB. The process for loading and release is reversible for at least eight cycles investigated so far. Equipped with these smart features, this LbL-based film affords useful information for the development of intelligent drug delivery platforms and appropriate biological studies. Currently we are planning to apply this LbL-based system for the light-controlled release in biodegradable poly(lactic acid), which provides an ideal substrate for therapeutic delivery using surgical implantion.

Acknowledgements

We thank Chinese Key Basic Research Program (2010CB529906), Wuhan Key Technologies R&D Program (201250499145-10, 2013011001010483), and the Opening Project of Key Laboratory of Optoelectronic Chemical Materials and Devices of Ministry of Education (JDGD-2013-16) for funding. One of the authors wish to thank CongCong Ni for helping in UV-vis measurement.

References

[1] Zhou S-L., Matsumoto S., Tian H-D., Yamane H., Ojida A., Kiyonaka S., Hamachi I.: pH-responsive shrinkage/swelling of a supramolecular hydrogel composed of two small amphiphilic molecules. Chemistry A European Journal, **11**, 1130–1136 (2005). DOI: 10.1002/chem.200400677

[2] Zhao Y., Yokoi H., Tanaka M., Kinoshita T., Tan T.: Self-assembled pH-responsive hydrogels composed of the RATEA16 peptide. Biomacromolecules, **9**, 1511–1518 (2008). DOI: 10.1021/bm701143g

[3] Ge Z., Xu J., Hu J., ZhangY., Liu S.: Synthesis and supramolecular self-assembly of stimuli-responsive water-soluble Janus-type heteroarm star copolymers. Soft Matter, **5**, 3932–3939 (2009). DOI: 10.1039/B907906H

[4] Isenbügel K., Gehrke Y., Ritter H.: Photo-switchable behavior of azobenzene-dye-modified silica nanoparticles and their assembly with cyclodextrin derivatives. Macromolecular Chemistry and Physics, **213**, 227–233 (2012). DOI: 10.1002/macp.201100601

[5] Sun T., Qing G.: Biomimetic smart interface materials for biological applications. Advanced Materials, **23**, H57–H77 (2011). DOI: 10.1002/adma.201004326

[6] Zhang X., Wang C.: Supramolecular amphiphiles. Chemical Society Reviews, **40**, 94–101 (2011). DOI: 10.1039/b919678c

[7] Wenz G., Han B-H., Müller A.: Cyclodextrin rotaxanes and polyrotaxanes. Chemical Reviews, **106**, 782–817 (2006).
DOI: 10.1021/cr970027+

[8] Peng K., Tomatsu I., Kros A.: Light controlled protein release from a supramolecular hydrogel. Chemical Communications, **46**, 4094–4096 (2010).
DOI: 10.1039/c002565h

[9] Zou J., Guan B., Liao X., Jiang M., Tao F.: Dual reversible self-assembly of PNIPAM-based amphiphiles formed by inclusion complexation. Macromolecules, **42**, 7465–7473 (2009).
DOI: 10.1021/ma901276c

[10] Chen C-J., Liu G-Y., Liu X-S., Li D-D., Ji J.: Construction of photo-responsive micelles from azobenzene-modified hyperbranched polyphosphates and study of their reversible self-assembly and disassembly behaviours. New Journal of Chemistry, **36**, 694–701 (2012).
DOI: 10.1039/c2nj20882b

[11] Ercole F., Davis T. P., Evans R. A.: Photo-responsive systems and biomaterials: Photochromic polymers, light-triggered self-assembly, surface modification, fluorescence modulation and beyond. Polymer Chemistry, **1**, 37–54 (2010).
DOI: 10.1039/b9py00300b

[12] Such G., Evans R. A., Yee L. H., Davis T. P.: Factors influencing photochromism of spiro-compounds within polymeric matrices. Journal of Macromolecular Science Part C: Polymer Reviews, **43**, 547–579 (2003).
DOI: 10.1081/mc-120025978

[13] Chen L., Xu S., Li J.: Recent advances in molecular imprinting technology: Current status, challenges and highlighted applications. Chemical Society Reviews, **40**, 2922–2942 (2011).
DOI: 10.1039/C0CS00084A

[14] Lee S-W., Takahara N., Korposh S., Yang D-H., Toko K., Kunitake T.: Nanoassembled thin film gas sensors. III. Sensitive detection of amine odors using TiO_2/poly (acrylic acid) ultrathin film quartz crystal microbalance sensors. Analytical Chemistry, **82**, 2228–2236 (2010).
DOI: 10.1021/ac901813q

[15] Zou J., Tao F., Jiang M.: Optical switching of self-assembly and disassembly of noncovalently connected amphiphiles. Langmuir, **23**, 12791–12794 (2007).
DOI: 10.1021/la702815h

[16] Dsouza R. N., Pischel U., Nau W. M.: Fluorescent dyes and their supramolecular host/guest complexes with macrocycles in aqueous solution. Chemical Reviews, **111**, 7941–7980 (2011).
DOI: 10.1021/cr200213s

[17] Ferris D. P., Zhao Y-L., Khashab N. M., Khatib H. A., Stoddart J. F., Zink J. I.: Light-operated mechanized nanoparticles. Journal of the American Chemical Society, **131**, 1686–1688 (2009).
DOI: 10.1021/ja807798g

[18] Hu X., Ji J.: Covalent layer-by-layer assembly of hyperbranched polyether and polyethyleneimine: Multilayer films providing possibilities for surface functionalization and local drug delivery. Biomacromolecules, **12**, 4264–4271 (2011).
DOI: 10.1021/bm201137x

[19] Tong W., Song X., Gao C.: Layer-by-layer assembly of microcapsules and their biomedical applications. Chemical Society Reviews, **41**, 6103–6124 (2012).
DOI: 10.1039/c2cs35088b

[20] Mohanta V., Madras G., Patil S.: Layer-by-layer assembled thin film of albumin nanoparticles for delivery of doxorubicin. The Journal of Physical Chemistry C, **116**, 5333–5341 (2012).
DOI: 10.1021/jp209479n

[21] Ariga K., Ji Q., Hill J. P., Bando Y., Aono M.: Forming nanomaterials as layered functional structures toward materials nanoarchitectonics. NPG Asia Materials, **4**, e17/1–e17/11 (2012).
DOI: 10.1038/am.2012.30

[22] Ikeda A., Hatano T., Shinkai S., Akiyama T., Yamada S.: Efficient photocurrent generation in novel self-assembled multilayers comprised of [60]fullerene–cationic homooxacalix[3]arene inclusion complex and anionic porphyrin polymer. Journal of the American Chemical Society, **123**, 4855–4856 (2001).
DOI: 10.1021/ja015596k

[23] Smith R. C., Riollano M., Leung A., Hammond P. T.: Layer-by-layer platform technology for small-molecule delivery. Angewandte Chemie International Edition, **48**, 8974–8977 (2009).
DOI: 10.1002/anie.200902782

[24] Mei X., Yang S., Chen D., Li N., Li H., Xu Q., Ge J., Lu J.: Light-triggered reversible assemblies of azobenzene-containing amphiphilic copolymer with β-cyclodextrin-modified hollow mesoporous silica nanoparticles for controlled drug release. Chemical Communications, **48**, 10010–10012 (2012).
DOI: 10.1039/c2cc33995a

[25] Wu Y., Wu S., Tian X., Wang X., Wu W., Zou G., Zhang Q.: Photoinduced reversible gel–sol transitions of dicholesterol-linked azobenzene derivatives through breaking and reforming of van der Waals interactions. Soft Matter, **7**, 716–721 (2011).
DOI: 10.1039/C0SM00330A

[26] Gong C. B., Lam M. H-W., Yu H. X.: The fabrication of a photoresponsive molecularly imprinted polymer for the photoregulated uptake and release of caffeine. Advanced Functional Materials, **16**, 1759–1767 (2006).
DOI: 10.1002/adfm.200500907

[27] Wan P., Jiang Y., Wang Y., Wang Z., Zhang X.: Tuning surface wettability through photocontrolled reversible molecular shuttle. Chemical Communications, **2008**, 5710–5712 (2008).
DOI: 10.1039/b811729b

[28] Davis M. E., Brewster M. E.: Cyclodextrin-based pharmaceutics: Past, present and future. Nature Reviews, Drug Discovery, **3**, 1023–1035 (2004).
DOI: 10.1038/nrd1576

[29] Xiao W., Chen W-H., Xu X-D., Li C., Zhang J., Zhuo R-X., Zhang X-Z.: Design of a cellular-uptake-shielding 'plug and play' template for photo controllable drug release. Advanced Materials, **23**, 3526–3530 (2011).
DOI: 10.1002/adma.201101806

[30] Yang Y. S., Qi G. R., Qian J. W., Yang S. L.: Acryloyl chloride polymer. Journal of Applied Polymer Science, **68**, 665–670 (1998).
DOI: 10.1002/(sici)1097-4628(19980425)68:4<665::aid-app18>3.0.co;2-q

[31] Wu L., Tuo X., Cheng H., Chen Z., Wang X.: Synthesis, photoresponsive behavior, and self-assembly of poly(acrylic acid)-based azo polyelectrolytes. Macromolecules, **34**, 8005–8013 (2001).
DOI: 10.1021/ma002215z

[32] Wu M., Cao Y., Zhang X., Zhang Y., Chen Y., He L., Qian Z.: Double 'plug and play' templates technology for photo controllable drug release polyelectrolyte multilayers. Chemical Communications, **48**, 9846–9848 (2012).
DOI: 10.1039/c2cc35274e

[33] Becker A. L., Johnston A. P. R., Caruso F.: Layer-by-layer-assembled capsules and films for therapeutic delivery. Small, **6**, 1836–1852 (2010).
DOI: 10.1002/smll.201000379

[34] Ferreira I. R., Ando R. A.: Shifting the azo–hydrazone tautomeric equilibrium of methyl yellow in acidic medium by the formation of inclusion complexes with cyclodextrins. Chemical Physics Letters, **522**, 51–53 (2012).
DOI: 10.1016/j.cplett.2011.12.011

[35] Chen Z., Dong S., Zhong C., Zhang Z., Niu L., Li Z., Zhang F.: Photoswitching of the third-order nonlinear optical properties of azobenzene-containing phthalocyanines based on reversible host–guest interactions. Journal of Photochemistry and Photobiology A: Chemistry, **206**, 213–219 (2009)
DOI: 10.1016/j.jphotochem.2009.07.005

[36] Park J. W., Song H. J.: Association of anionic surfactants with .beta.-cyclodextrin: Fluorescence-probed studies on the 1:1 and 1:2 complexation. The Journal of Physical Chemistry, **93**, 6454–6458 (1989).
DOI: 10.1021/j100354a035

[37] Choudhury S. D., Mohanty J., Upadhyaya H. P., Bhasikuttan A. C., Pal H.: Photophysical studies on the noncovalent interaction of thioflavin T with cucurbit[*n*]uril macrocycles. The Journal of Physical Chemistry B, **113**, 1891–1898 (2009).
DOI: 10.1021/jp8103062

[38] Fedorova O. A., Chernikova E. Y., Fedorov Y. V., Gulakova E. N., Peregudov A. S., Lyssenko K. A., Jonusauskas G., Isaacs L.: Cucurbit[7]uril complexes of crown-ether derived styryl and (bis)styryl dyes. The Journal of Physical Chemistry B, **113**, 10149–10158 (2009).
DOI: 10.1021/jp903289q

[39] Wagner B. D., Fitzpatrick S. J., Gill M. A., MacRae A. I., Stojanovic N.: A fluorescent host-guest complex of cucurbituril in solution: A molecular Jack O'Lantern. Canadian Journal of Chemistry, **79**, 1101–1104 (2001).
DOI: 10.1139/v01-094

[40] Yang S. Y., Rubner M. F.: Micropatterning of polymer thin films with pH-sensitive and cross-linkable hydrogen-bonded polyelectrolyte multilayers. Journal of the American Chemical Society, **124**, 2100–2101 (2002).
DOI: 10.1021/ja017681y

[41] Matsusaki M., Ajiro H., Kida T., Serizawa T., Akashi M.: Layer-by-layer assembly through weak interactions and their biomedical applications. Advanced Materials, **24**, 454–474 (2012).
DOI: 10.1002/adma.201103698

[42] Song X., Perlstein J., Whitten D. G.: Supramolecular aggregates of azobenzene phospholipids and related compounds in bilayer assemblies and other microheterogeneous media: Structure, properties, and photoreactivity[1]. Journal of the American Chemical Society, **119**, 9144–9159 (1997).
DOI: 10.1021/ja971291n

[43] Chakraborty B., Basu S.: Deciphering the host–guest chemistry of acridine yellow and cucurbit[7]uril: An integrated spectroscopic and calorimetric study. Chemical Physics Letters, **507**, 74–79 (2011).
DOI: 10.1016/j.cplett.2011.03.014

[44] Zhang Y., Sun X-Y., Liu B.: Fluorescent recognition for single- and double-stranded oligonucleotides based on rhodamine B-modified self-assembled bilayers. Chinese Journal of Analytical Chemistry, **37**, 665–670 (2009).
DOI: 10.1016/s1872-2040(08)60103-6

eXPRESS Polymer Letters Vol.8, No.3 (2014) 154–163
Available online at www.expresspolymlett.com
DOI: 10.3144/expresspolymlett.2014.19

Effect of fibre spinning conditions on the electrical properties of cellulose and carbon nanotube composite fibres spun using ionic liquid as a benign solvent

C. Zhu[1], *J. Chen*[2], *K. K. Koziol*[2], *J. W. Gilman*[3], *P. C. Trulove*[4], *S. S. Rahatekar*[1*]

[1]Advanced Composites Centre for Innovation and Science (ACCIS), Aerospace Engineering, University of Bristol, BS8 1TR Bristol, UK
[2]Department of Materials Science & Metallurgy, University of Cambridge, CB3 0FS Cambridge, UK
[3]Material Measurement Laboratory, Materials Science Division, National Institute of Standards and Technology, MD 20899 Gaithersburg, USA
[4]Chemistry Department, U.S. Naval Academy, MD 21402 Annapolis, USA

Received 12 August, 2013; accepted in revised form 21 October 2013

Abstract. The aim of this study was to develop electrically conductive fibres from cellulose. To achieve this, the effect of fibre extrusion speed and fibre winding speed on the degree of alignment of multiwall carbon nanotubes (MWNTs), as well as the resulting electrical properties of the cellulose/MWNTs composite fibres were systematically studied. 1-Ethyl-3-Methylimidazolium Acetate (EMIMAc) was used as an environmentally benign solvent for dissolution of cellulose as well as for dispersion of MWNTs in the solution dope. To achieve good dispersion of MWNTs in the cellulose solution dope, MWNTs were non-covalently functionalized using carboxymethyl cellulose (CMC). This significantly improved the dispersion of MWNTs in the solution dope. The degree of alignment of MWNTs after both fibre extrusion and winding, was studied using scanning electron microscopy (SEM) and wide angle X-ray diffraction (WAXD). The degree of alignment of MWNTs was correlated with the electrical properties. A significant decrease in electrical conductivity accompanied the increase in degree of alignment of MWNTs when fibres were spun with higher extrusion speed. The decrease was also measured when fibres were spun with higher winding speed using a constant extrusion speed. However, the decrease in conductivity due to winding was low relative to fibres spun at highest extrusion speed.

Keywords: *nanocomposites, cellulose, ionic liquid, fibre spinning, conductivity*

1. Introduction

Electrically conductive polymer textile fibre is desirable in applications such as electronic textiles (smart shirt) [1] which can measure body temperature and heart rate, as well as in textiles which can be used as electrically conducting implantable electrodes for brain stimulation [2]. Carbon nanotubes offer a great potential to be used as electrically conducting inclusions in textiles due to their excellent electrical conductivity and high aspect ratio [3]. Many researchers have studied the properties of nylon/nanoparticle [4] and PBO/carbon nanotube textiles [5], as well as others with improved electrical properties [6, 7]. Cellulose textiles reinforced with carbon nanotubes can offer a combination of good biocompatibility, electrical conductivity, and the ability to be easily spun and woven into textile fabrics [8]. However, there are three main challenges to achieving highly conductive cellulose/carbon nanotubes composite fibres, namely, 1) dissolution and fibre spinning of cellulose using a benign solvent, 2) uniform dispersion of carbon nanotubes

*Corresponding author, e-mail: Sameer.Rahatekar@bristol.ac.uk

in cellulose and 3) avoiding alignment of carbon nanotubes (which will result in lower electrical conductivity) during the fibre spinning process. To overcome the first challenge, room temperature ionic liquids such as EMIMAc can be employed as environmentally benign solvent, which is safer and easier to handle than traditionally used solvents such as carbon disulphide [9], sulphuric acid [10] and *N*-methylmorpholine-*N*-oxide (NMMO) [11]. A number of researchers have used ionic liquids for fibre stretching/spinning of cellulose [12–18], wool [19, 20], chitin [21–24] and other natural polymers [25–28], as well as composite fibres of cellulose [8, 29]. Despite this progress, the remaining two challenges, uniform dispersion of carbon nanotube in cellulose solution dope and avoidance of high degree of alignment of carbon nanotubes during fibre spinning, still remain largely unaddressed. In the present study, we look at methods of improving the dispersion of carbon nanotubes in EMIMAc and in cellulose solution dope. We also carefully study the effect of fibre spinning parameters such as fibre extrusion speed and fibre winding speed on the electrical conductivity of the cellulose/carbon nanotube composite fibres. This study will be specifically useful for improving the degree of dispersion of carbon nanotubes in cellulose fibres, electrical conductivity of cellulose/nanotubes composite fibres and their potential use for other applications such as conducting textiles and for implantable electrodes for stimulation of tissues.

2. Experimental

2.1. Materials and methods

The ionic liquid (IL) 1-Ethyl-3-Methylimidazolium Acetate (EMIMAc) and carboxymethyl cellulose (CMC) were obtained from Sigma-Aldrich (419273, Gillingham, UK). The cellulose pulp sheets with a degree of polymerisation (DP) of 890 were provided by Rayonier (Jacksonville, United States). The MWNT forest, with average MWNT outer diameter of 80 nm and length of 1 mm [8], were kindly supplied by Department of Materials Science & Metallurgy in University of Cambridge with synthesis details and characterisation published elsewhere [30].

A magnetic stirrer hotplate (Fisher scientific, Loughborough, UK) with oil bath was used for solution preparation. The dissolution processing was carried out in a hood. The cellulose pulp sheets were fine chopped into small pieces with scissors and ground with a grinder.

2.2. CMC/MWNTs preparation

300 mg CMC was grounded uniformly in a few millilitres of distilled water using mortar and pestle. Then 300 mg MWNTs forest was mixed and grounded together with the CMC/H_2O suspension. The MWNTs/CMC/H_2O mixture was added in a 250 mL conical flask with 200 mL distilled water, and sonicated for 30 min using 40% amplitude of power at 80°C with stirring at 10.5 rad/s for 24 h until all water evaporated, leaving only dry and thin CMC/MWNTs film. The dry CMC/MWNTs film was added into 20 g EMIMAc and heated at 80°C with stirring at 10.5 rad/s for 2 h, then kept stirred without heating for 24 h to get the uniform 15 mg/g concentration MWNTs/EMIMAc suspension.

2.3. Fibre spinning

For fibre spinning, we used 0.08 mass fraction cellulose in EMIMAc to make high viscosity (415.5 Pa·s) solution, which was easily spun. 2 g cellulose (0.08 mass fraction with respect to the total amount of 25 g EMIMAc) was added into 11.66 g EMIMAc in an 80 mL glass reagent bottle and heated at 85°C with stirring at 10.5 rad/s for 2 h. Then 13.34 g MWNTs/EMIMAc suspension (0.10 mass fraction MWNTs with respect to cellulose) was added into the cellulose/ EMIMAc solution and heated at 85°C with stirring at 10.5 rad/s for 5 h.

After complete dissolution, the MWNTs/cellulose/EMIMAc fibre solution was transferred into a 20 mL luer lock syringe (Terumo, UK). The solution in syringe was vacuumed in a vacuum oven at 80°C for 16 hours before spinning. Lab-built spinning equipment, which consisted of a syringe pump, a water bath and a winding drum with monitor, was used for fibre spinning. Two different fibre spinning conditions were used as shown in Figure 1. In the first set up, the fibres were simply extruded at varying extrusion velocities (V_1) and were immediately coagulated without fibre winding (Figure 1a). In the second set up, the cellulose/MWNTs solution dope was injected into water bath at fixed extrusion velocity (V_1), while the winding drum and electric motor were continuously winding the fibres at varying winding velocities (V_2) downstream (Figure 1b). The first series of fibres were manufactured without winding ($V_2 = 0$) using different extrusion speeds (V_1)

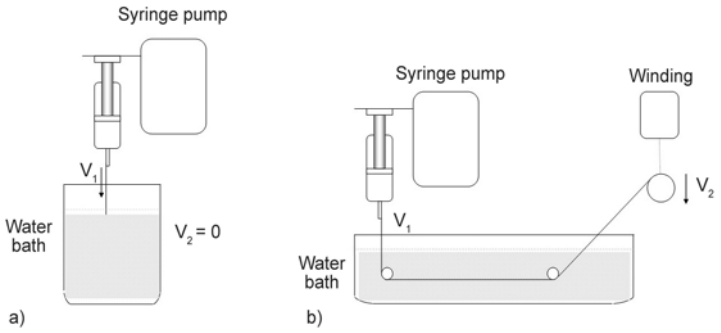

Figure 1. Spinning equipment for (a) the first series of cellulose/MWNTs fibres and (b) the second series of cellulose/MWNTs fibres

of $2.65 \cdot 10^{-3}$, $5.3 \cdot 10^{-3}$, $7.95 \cdot 10^{-3}$ and $1.06 \cdot 10^{-2}$ m/s. The second series of fibres was manufactured using a constant extrusion speed of $V_1 = 5.3 \cdot 10^{-3}$ m/s with different winding speeds (V_2) of 0 and $2.5 \cdot 10^{-2}$ m/s. The air gap between the nozzle and water surface was 1 cm. After spinning, the fibres were merged in distilled water for two days, with a change of water every 24 h. Then the fibres were rolled and dried in a fume hood for a further 48 h. For each kind of fibre, two 5 mm long lengths, 2 mm apart, were coated using conductive silver paint (Electrolube, UK). The painted fibres were dried at room temperature for 8 h.

2.4. Film preparation

We kept fixed concentration of MWNTs (0.10 mass fraction) in cellulose/MWNTs film and fibre's preparation for comparison. There was no external shear or extensional force applied during processing in film preparation, thus the MWNTs dispersion in film could be considered as random status. The film study was carried out only as one special case where there was no external shear or extensional force applied during processing (unlike the fibre spinning process which involved both shear and extensional deformations of polymer solution).

For film preparation, we used 0.015 mass fraction cellulose to make low viscosity solution which was easily spread into a film. 0.075 g cellulose (0.015 mass fraction with respect to the total amount of 5 g EMIMAc) was added into 4.5 g EMIMAc in a 10 mL glass bottle and heated at 85°C with stirring at 10.5 rad/s for 2 h. Then 0.5 g MWNTs/EMIMAc suspension (0.10 mass fraction MWNTs with respect to cellulose) was added into the cellulose/ EMIMAc solution and heated at 85°C with stirring at 10.5 rad/s for 2 h.

After complete dissolution, the MWNTs/cellulose/EMIMAc solution was poured into a 75 mm diameter glass petri dish to form a film, covering the bottom of the petri dish uniformly. The film was put in the hood at room temperature for 24 h to gel by absorbing moisture from the air. Then, the film was put into distilled water to remove the EMIMAc (water was changed every day). After two days, the film was dried in the hood at room temperature for 5 days.

Five pieces of rectangular films whose widths were about 5 mm were· cut and labelled as Sample 1 through Sample 5. Two 5 mm long parts on each sample were coated using conductive silver paint (Electrolube, UK), leaving a 2 mm gap between them. The painted films were dried at room temperature for 8 h.

2.5. Characterization of cellulose/MWNTs films and fibres

The width and height of the film sample were measured using a calliper. Three different locations' widths and heights were measured on the film to obtain the average width and height. The fibre's diameter was measured using a microscope. The microscopy analysis was carried out using a DMI 3000B microscope produced by Leica Microsystems CMS GmbH (Wetzlar, Germany) under TL-BF (bright field transmitted light) method. Three photos on different locations were taken on the 2 mm long part of fibre between the two silver painted parts. For each microscope picture, three different locations' diameters were measured using the ImageJ software package. Thus, for all cellulose/MWNTs composite fibre samples, nine different locations' fibre diameters on the 2 mm long part were measured. The average diameter and the standard deviation were calculated and obvious die-swell behavior in first series of fibres with only extrusion is shown in Figure 2 [31].

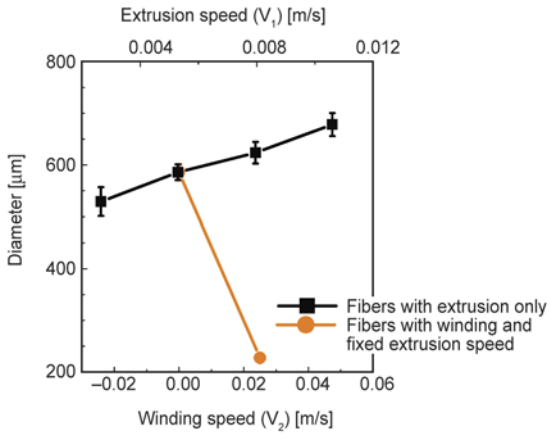

Figure 2. Fibre diameter measurements of cellulose/MWNTs fibres as a function of extrusion speed and winding speed

The Fourier Transform Infrared Spectroscopy (FTIR) reflection was performed on a Spectrum 100 FTIR spectrometer (PerkinElmer). A total of 4 cumulative scans were taken, with a resolution of 4 cm^{-1}, in the wavenumber range between 4000 to 650 cm^{-1} under absorbance mode.

The electrical conductivity testing was conducted with a 2-point conductivity rig to fix the samples and a precision LCR400 bridge (Thurlby Thandar instruments, UK). The two silver painted parts of films or fibres were fixed on the two copper points of the rig and the resistances of the 2 mm long fibres between the points were measured. The cellulose/MWNTs composite films and fibres' electrical conductivity were calculated using the Equation (1):

$$\sigma = \frac{L}{R \cdot A} \tag{1}$$

where R is the resistance measured over length L, and A is the cross-sectional area of the sample [32]. All samples for scanning electron microscope (SEM) analysis were prepared using Emitech K550 Sputter coater with 10 seconds of gold sputter coating. Both composite film and fibre samples were stretched and broken manually after cooling with liquid nitrogen. The cross-sectional areas of the samples were revealed and further observed by using JEOL 6340F.

Wide angle X-ray diffraction (WAXD) patterns were obtained using CCD & X-ray photography, Generator 8, in University of Cambridge. It consists of an X-ray generator with c-tech XRD tube using CuK_α radiation, a sample holder and a cassette with film inside to collect/detect the pattern. The machine ran at 40 kV and 40 mA, with 4–6 hours of exposure time to obtain the pattern on the film. The films were developed after exposure, dried and scanned to get digital pattern images. The pattern images were scanned using software of IDL to obtain both azimuthal and radial scanning data.

3. Results and discussion

3.1. MWNTs dispersion in EMIMAc

To manufacture cellulose/MWNTs composite fibres with uniform diameter, stable properties and experimental repeatability, the MWNTs need to have a good dispersion in cellulose/EMIMAc solution. CMC can be dissolved in both water and EMIMAc, and has been shown to debundle carbon nanotubes [33]. CMC is nonconductive, which may reduce the level of direct contact between MWNTs after coating, but can give MWNTs excellent uniform disper-

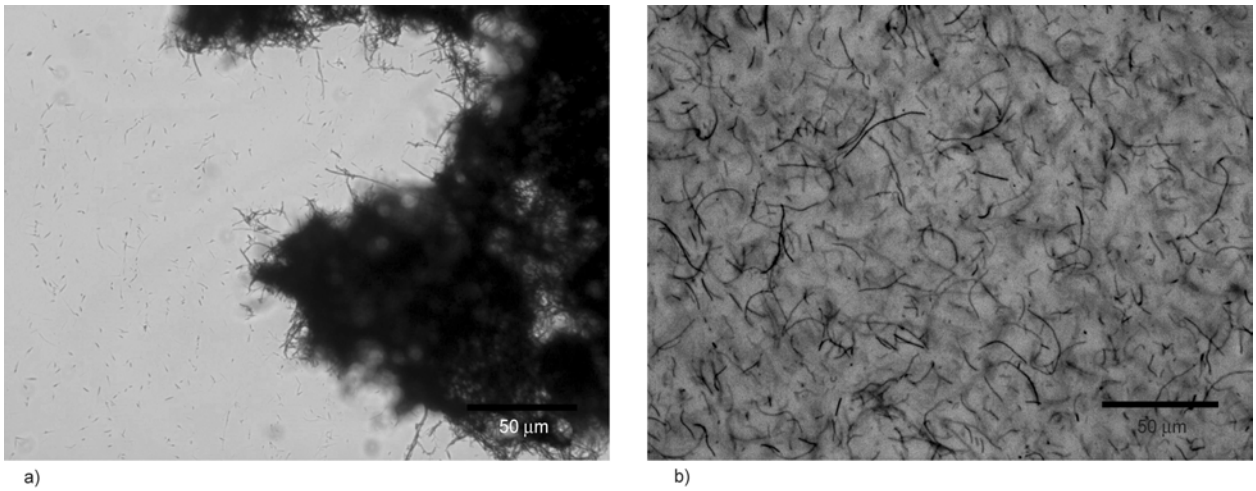

Figure 3. Optical micrographs of MWNTs dispersion in EMIMAc (a) without CMC and (b) with CMC

sion in EMIMAc and in cellulose fibres. The CMC coating of MWNTs improves the degree of MWNTs dispersion in cellulose which is a key requirement in developing a high quality nanocomposite product. Thus, we mixed CMC with MWNTs before adding MWNTs into EMIMAc. Figure 3a shows an optical micrograph of MWNTs dispersion without CMC coating and Figure 3b shows the MWNTs dispersion with CMC coating. The CMC/MWNTs mixture had an excellent dispersion in EMIMAc. This is because the CMC can potentially form hydrogen bonds with EMIMAc, like cellulose, and coated the surfaces of MWNTs to avoid self-entanglement, both of which contribute to the improved dispersion in EMIMAc [33].

3.2. FTIR analysis of raw cellulose and cellulose/MWNTs composite fibres

FTIR analysis was used to confirm that EMIMAc was completely removed from cellulose/MWNTs fibres. The FTIR spectra of raw cellulose, cellulose/MWNTs fibre and EMIMA are shown in Figure 4a. The hydrogen bond network inside raw cellulose was broken by EMIMAc leading to cellulose's dissolution [34, 35], and couldn't recover completely after cellulose's coagulation. The CH_2 symmetric bending peak in the spectra (Figure 4b) weakened and shifted from 1427.6 to 1416.4 cm^{-1} after regeneration, indicating the destruction of the intramolecular hydrogen bond in C_6–OH to some extent [35, 36]. The typical function group C=N (1562.7 cm^{-1}) of EMIMAc [37] is not present in cellulose/MWNTs fibre's spectrum (Figure 4c). This means that during coagulation process the majority of EMIMAc has been removed from fibres.

3.3. Electrical conductivity measurement of cellulose/MWNTs composite film and fibres

The electrical conductivity of cellulose/MWNTs fibres decreases as the extrusion speed (V_1) increases as seen in Table 1 and Figure 5 (winding speed was kept to zero; $V_2 = 0$). The average conductivity of the cellulose/MWNTs composite film ($V_1 = 0$) is 18.05 S/m, which is 75.2 times larger than the fibre with the slowest extrusion speed (0.24 S/m; $V_1 = 2.65 \cdot 10^{-3}$ m/s) and 501.4 times larger than the fibre with the fastest extrusion speed fibre (0.036 S/m; $V_1 = 1.06 \cdot 10^{-2}$ m/s). The effect of winding speed on the reduction in the electrical conductivity of fibres was relatively small compared with the effect of extrusion speed (Table 1 and Figure 5). A modest decrease in conductivity (from 0.11 to 0.045 S/m) was observed due to winding the fibres after extrusion as seen in Figure 5.

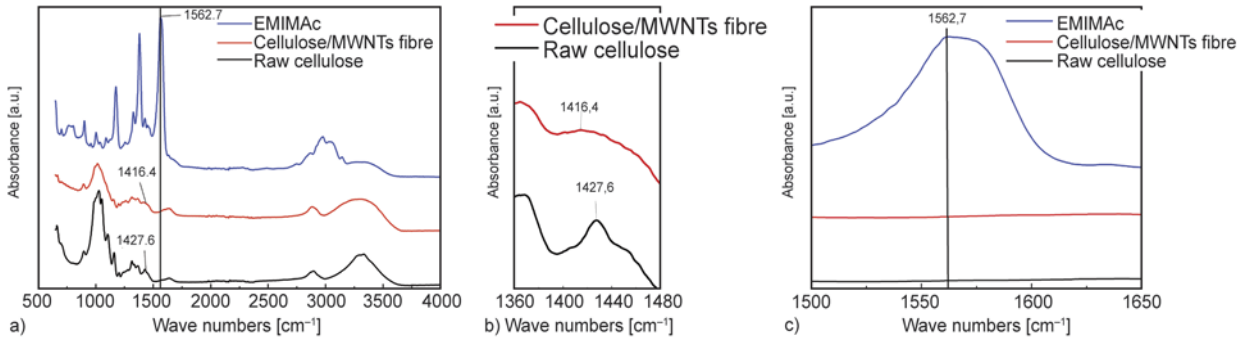

Figure 4. FTIR spectra of (a) raw cellulose, cellulose/MWNTs fibre and EMIMAc between 650–4000 cm^{-1}, (b) raw cellulose and cellulose/MWNTs fibre between 1360–1480 cm^{-1} which show the weekended and shifted peak corresponding to CH_2 (1427.6, 1416.4 cm^{-1}) of cellulose after regeneration, and (c) raw cellulose, cellulose/MWNTs fibre and EMIMAc between 1500–1650 cm^{-1} which show absence of the peak corresponding to C=N (1562.7 cm^{-1}) of EMIMAc

Table 1. Conductivity and WAXD data for cellulose/MWNTs film and fibres

Name	Extrusion speed (V_1) and winding speed (V_2)	Conductivity [S/m]	FWHM of MWNT (002) peak
Film	$V_1 = 0$, $V_2 = 0$	18.050±3.490	164.71
Fibre series 1	$V_1 = 2.65 \cdot 10^{-3}$ m/s, $V_2 = 0$	0.239±0.019	–
	$V_1 = 5.30 \cdot 10^{-3}$ m/s, $V_2 = 0$	0.112±0.016	54.07
	$V_1 = 7.96 \cdot 10^{-3}$ m/s, $V_2 = 0$	0.080±0.010	–
	$V_1 = 1.06 \cdot 10^{-2}$ m/s, $V_2 = 0$	0.036±0.021	–
Fibre series 2	$V_1 = 5.30 \cdot 10^{-3}$ m/s, $V_2 = 0$	0.112±0.016	54.07
	$V_1 = 5.3 \cdot 10^{-3}$ m/s, $V_2 = 2.5 \cdot 10^{-2}$ m/s	0.045±0.009	28.72

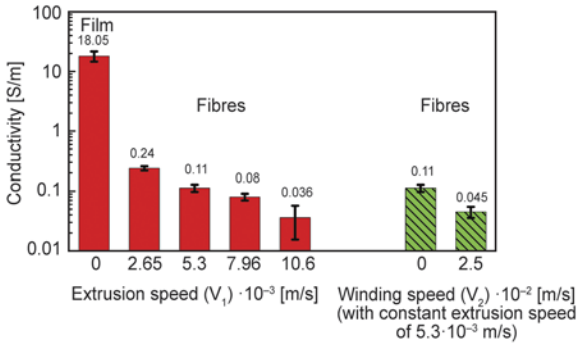

Figure 5. Conductivity of cellulose/MWNTs film and fibres with extrusion only, or with extrusion and winding

3.4. SEM analysis of cellulose/MWNTs composite film and fibres

SEM images of the composite film and fibre cross-sections show MWNTs dispersion in cellulose (Figure 6). MWNTs appear to be oriented randomly in the composite the film (Figure 6a). However, the MWNTs show more alignment as the extrusion speed is increased (Figure 6b–6c).

SEM images of cellulose/MWNTs fibres' cross sections (Figure 6b–6c), when the extrusion speed was very slow, show that MWNTs have a slight tendency to align along the fibre axis. As the extrusion and winding speeds increased, the alignment of MWNTs along fibre axis greatly increased. This means that during spinning, MWNTs dispersed well in EMIMAc and became aligned because of the shear and extensional force. This alignment is contributing to the decrease in fibre conductivity, because MWNTs are not in effective contact. The conducting pathways formed by contact between MWNTs through the fibre sample are reduced significantly due to the interval between orientated MWNTs as shown by previous theoretical work for electrical percolation of rigid rods [38]. Previous researchers have also reported alignment of carbon nanotubes during extrusion of polycarbonate and carbon nanotubes fibres using TEM analysis [39]. The decrease of conductivity due to alignment of nanofibres was also predicted in our previous studies using a combination of dissipative particle dynamics and Monte Carlo modelling method [40].

3.5. X-ray analysis of aellulose/MWNTs composite film and fibres

Figure 7 shows the WAXD radial scanning data (intensity against 2θ) of cellulose and MWNTs in a cellulose/MWNTs composite film and fibres at varying extrusion speeds. The diffraction patterns of these film and fibres correspond to the cellulose

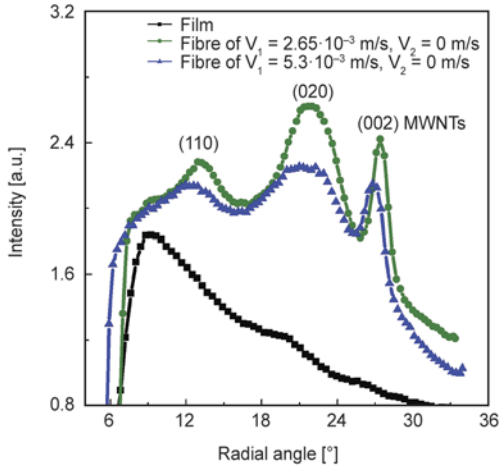

Figure 7. Integrated radial scans of cellulose/MWNTs film and fibres under different extrusion speeds without winding ($V_1 = 2.65 \cdot 10^{-3}$ m/s, $V_2 = 0$ m/s; $V_1 = 5.3 \cdot 10^{-3}$ m/s, $V_2 = 0$ m/s)

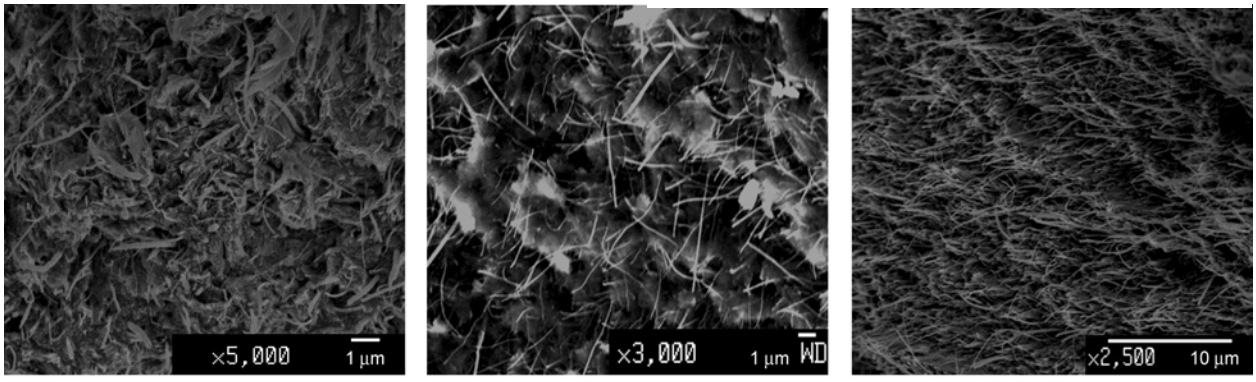

Figure 6. SEM micrographs of stretched and broken cross sections of (a) cellulose/MWNTs film, (b) cellulose/MWNTs fibre with spinning speed of $V_1 = 5.3 \cdot 10^{-3}$ m/s, $V_2 = 0$ m/s and (c) cellulose/MWNTs fibre with spinning speed of $V_1 = 5.3 \cdot 10^{-3}$ m/s, $V_2 = 2.5 \cdot 10^{-2}$ m/s

II structure [41, 42], which is a widely known type of crystal structure of regenerated cellulose after its dissolution. In addition, the (002) graphitic peak at $2\theta = 26.8°$ corresponding to MWNTs is also observed

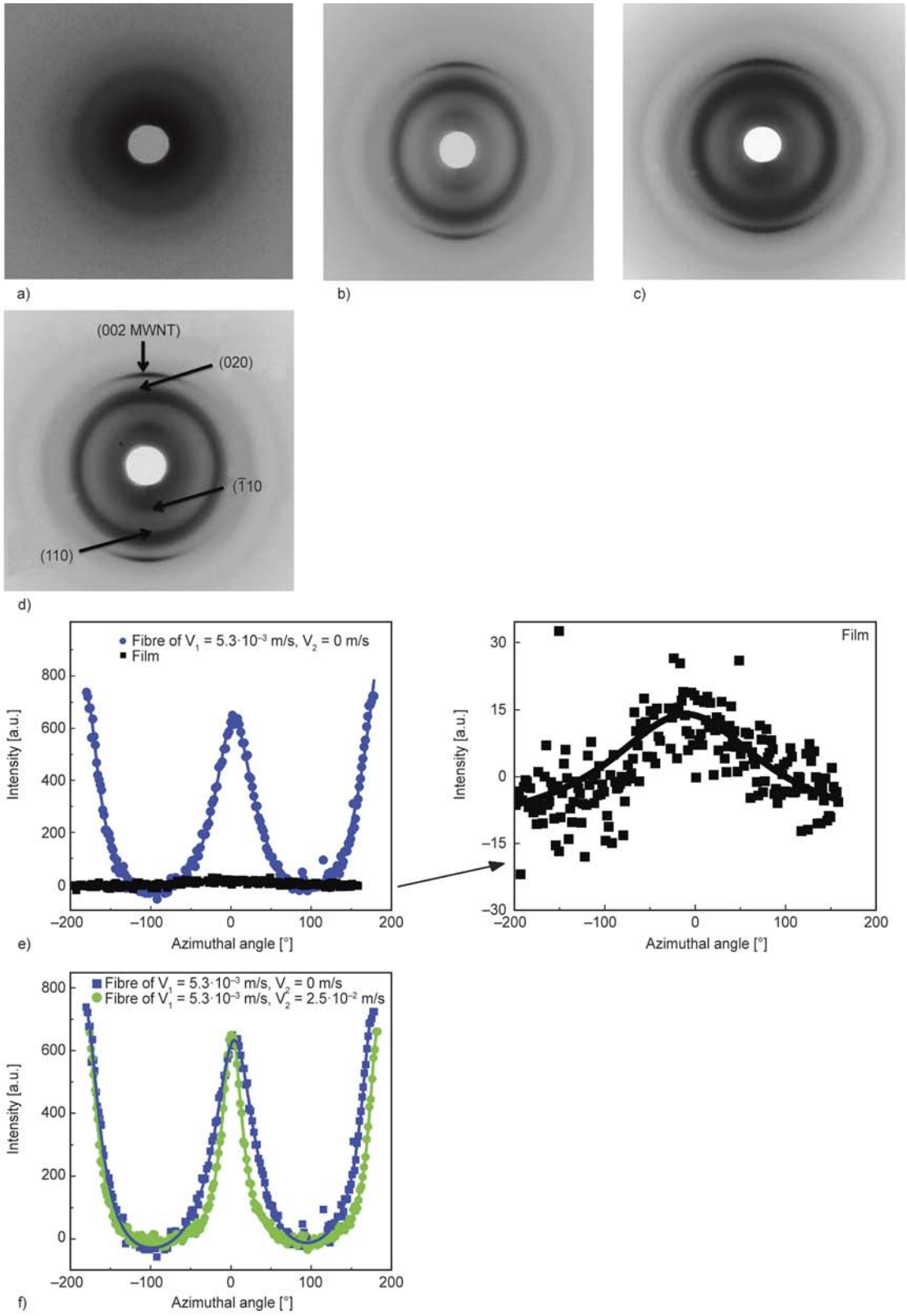

Figure 8. WAXD patterns of (a) cellulose/ MWNTs film, (b) cellulose/MWNTs fibres with speed of $V_1 = 2.65 \cdot 10^{-3}$ m/s, $V_2 = 0$ m/s, (c) $V_1 = 5.3 \cdot 10^{-3}$ m/s, $V_2 = 0$ m/s and (d) $V_1 = 5.3 \cdot 10^{-3}$ m/s, $V_2 = 2.5 \cdot 10^{-2}$ m/s, and azimuthal scans of (e) cellulose/MWNTs fibres spun with different extrusion speeds without winding ($V_1 = 0$ m/s, $V_2 = 0$ m/s; $V_1 = 5.3 \cdot 10^{-3}$ m/s, $V_2 = 0$ m/s) as well as (f) cellulose/MWNTs fibres spun with different winding speeds and fixed extrusion speed ($V_1 = 5.3 \cdot 10^{-3}$ m/s, $V_2 = 0$ m/s; $V_1 = 5.3 \cdot 10^{-3}$ m/s, $V_2 = 2.5 \cdot 10^{-2}$ m/s)

in the composite fibres as expected [8, 43]. The peaks at around 12° correspond to cellulose ($\bar{1}10$) plane, whereas the peaks at around 22° correspond to cellulose (020) plane [8, 39, 41].

Figure 8a–8d show the two dimensional WAXD diffraction patterns of cellulose film and fibres spun at different spinning rates. SEM image of the film (Figure 6a) shows no alignment of MWNTs. Similarly WAXD data (Figure 8a and 8e) for film sample shows diffraction ring corresponding to MWNTs and hashas intensity uniformly distributed azimuthally along the circumference, which confirm no preferred orientation of MWNTs [43]. In a stretched fibre, the MWNTs have a preferred orientation with their longitudinal axes parallel to the strain direction, which appear as concentrated intensity in the diffraction ring in the azimuthal direction. The intensity of the diffraction ring becomes more anisotropic as the extrusion/winding speed increases, as shown in Figure 8b–8d [43]. Figure 8e–8f shows the azimuthal scans of MWNT (002) peak of these fibres. The full width at half maximum (FWHM) for MWNT (002) azimuthal scan is shown in Figure 8e, which decreases from 164.71 to 54.07 with increased extrusion speed from 0 m/s (film, no extrusion) to $5.3 \cdot 10^{-3}$ m/s. The full width half max (FWHM) of 002 peak from MWNTs is a measure of degree of alignment of the MWNTs. The lower the value of FWHM, the higher is the degree of alignment of MWNTs, which is consistently observed with the increase in the extrusion and winding speeds of the composite fibre [44]. This confirms that the alignment of MWNTs in fibre increases as extrusion speed increases, which is the reason for the reduction in the conductivity of fibres as shown in Table 1. This observation is consistent with the SEM images for the cross-section of film and fibre composites. In Figure 8f, the FWHM for MWNT (002) azimuthal scan peak reduces from 54.07 to 28.72 as fibre winding speed increases from 0 m/s to $2.5 \cdot 10^{-2}$ m/s. This confirms that the increased degree of MWNTs alignment is due to the increase in fibre winding speed.

4. Conclusions

In this paper we presented a novel method for uniform dispersion of MWNTs for manufacturing electrically conducting textiles. Dispersion of MWNTs is challenging due to their low surface energy. To address this problem we used non-covalent surface modification of MWNTs using CMC, which wraps around carbon nanotubes to enable good dispersion in water as well as ionic liquid (EMIMAc). This process modification allows us to use ionic liquid as a common platform to achieve good dispersion of MWNTs, as well as act as a benign solvent for spinning of cellulose nanocomposite fibres. To understand the effect of alignment of MWNTs due to shear and extensional deformation of fibre during spinning process, we systematically studied the change in the electrical properties of cellulose/MWNT in two ways: as a function of extrusion speed without fibre winding/spinning, and as a function of fibre winding/spinning speed at constant extrusion speed. Increased extrusion speed causes a significant decrease in the electrical conductivity of the cellulose/MWNT fibre due to alignment of MWNTs, which results in reduced contact between MWNTs in the cellulose fibre matrix. The increased degree of alignment of MWNTs after extrusion and after fibre spinning/stretching was confirmed by SEM and WAXD studies. While it is important to produce textiles at high extrusion and winding speeds for increased productivity, it is clear from this study that in order to achieve good electrical conductivity the cellulose/MWNTs based smarts textiles need to be spun at moderately low speeds (extrusion speed such as $V_1 = 5.3 \cdot 10^{-3}$ m/s). The set of experiments carried out in the current work provide useful basic guideline for manufacturing of such smart textiles from cellulose/MWNTs composite fibres.

Acknowledgements

This work was supported by the Faculty of Engineering, the Centre for Nanoscience and Quantum Information (NSQI), the Faculty of Physics at the University of Bristol, and the Department of Materials Science & Metallurgy at the University of Cambridge. Prof. Paul C. Trulove and J. W Gilman wish to acknowledge funding from the U.S. Air Force Office of Scientific Research.

A portion of this work was carried out by the National Institute of Standards and Technology (NIST), an agency of the U. S. government and by statute is not subject to copyright in the United States. Certain commercial equipment, instruments, materials, services, or companies are identified in this paper in order to specify adequately the experimental procedure. This in no way implies endorsement or recommendation by NIST.

References

[1] Laxminarayana K., Jalili N.: Functional nanotube-based textiles: Pathway to next generation fabrics with enhanced sensing capabilities. Textile Research Journal, **75**, 670–680 (2005).
DOI: 10.1177/0040517505059330

[2] Llinás R., Mühlethaler M.: Electrophysiology of guinea-pig cerebellar nuclear cells in the in vitro brain stem-cerebellar preparation. Journal of Physiology, **404**, 241–258 (1988).

[3] Xie X-L., Mai Y-W., Zhou X-P.: Dispersion and alignment of carbon nanotubes in polymer matrix: A review. Materials Science and Engineering R: Reports, **49**, 89–112 (2005).
DOI: 10.1016/j.mser.2005.04.002

[4] Rangari V. K., Shaik M. Y., Mahfuz H., Jeelani S.: Fabrication and characterization of high strength Nylon-6/Si_3N_4 polymer nanocomposite fibers. Materials Science and Engineering: A, **500**, 92–97 (2009).
DOI: 10.1016/j.msea.2008.09.014

[5] Zhang C., Yuan W., Wang S., Liang X.: Effect of MWCNTs irradiation grafting treatment on the surface properties of PBO fiber. Journal of Applied Polymer Science, **121**, 3455–3459 (2011).
DOI: 10.1002/app.33996

[6] Vankayala R. R., Lai W-J. P., Cheng K-C., Hwang K. C.: Enhanced electrical conductivity of nylon 6 composite using polyaniline-coated multi-walled carbon nanotubes as additives. Polymer, **52**, 3337–3343 (2011).
DOI: 10.1016/j.polymer.2011.05.007

[7] Kumar S., Dang T. D., Arnold F. E., Bhattacharyya A. R., Min B. G., Zhang X., Vaia R. A., Park C., Adams W. W., Hauge R. H., Smalley R. E., Ramesh S., Willis P. A.: Synthesis, structure, and properties of PBO/SWNT composites. Macromolecules, **35**, 9039–9043 (2002).
DOI: 10.1021/ma0205055

[8] Rahatekar S. S., Rasheed A., Jain R., Zammarano M., Koziol K. K., Windle A. H., Gilman J. W., Kumar S.: Solution spinning of cellulose carbon nanotube composites using room temperature ionic liquids. Polymer, **50**, 4577–4583 (2009).
DOI: 10.1016/j.polymer.2009.07.015

[9] Fischer K., Hintze H., Schmidt I.: Reactivity of cellulose and characteristics of viscose. Papier, **50**, 682–687 (1996).

[10] Camacho F., González-Tello P., Jurado E., Robles A.: Microcrystalline-cellulose hydrolysis with concentrated sulphuric acid. Journal of Chemical Technology and Biotechnology, **67**, 350–356 (1996).
DOI: 10.1002/(sici)1097-4660(199612)67:4<350::aid-jctb564>3.0.co;2-9

[11] Fink H-P., Weigel P., Purz H. J., Ganster J.: Structure formation of regenerated cellulose materials from NMMO-solutions. Progress in Polymer Science, **26**, 1473–1524 (2001).
DOI: 10.1016/s0079-6700(01)00025-9

[12] Heinze T., Schwikal K., Barthel S.: Ionic liquids as reaction medium in cellulose functionalization. Macromolecular Bioscience, **5**, 520–525 (2005).
DOI: 10.1002/mabi.200500039

[13] El Seoud O. A., Koschella A., Fidale L. C., Dorn S., Heinze T.: Applications of ionic liquids in carbohydrate chemistry: A window of opportunities. Biomacromolecules, **8**, 2629–2647 (2007).
DOI: 10.1021/bm070062i

[14] Kosan B., Michels C., Meister F.: Dissolution and forming of cellulose with ionic liquids. Cellulose, **15**, 59–66 (2008).
DOI: 10.1007/s10570-007-9160-x

[15] Hermanutz F., Gähr F., Uerdingen E., Meister F., Kosan B.: New developments in dissolving and processing of cellulose in ionic liquids. Macromolecular Symposia, **262**, 23–27 (2008).
DOI: 10.1002/masy.200850203

[16] Haward S. J., Sharma V., Butts C. P., McKinley G. H., Rahatekar S. S.: Shear and extensional rheology of cellulose/ionic liquid solutions. Biomacromolecules, **13**, 1688–1699 (2012).
DOI: 10.1021/bm300407q

[17] Swatloski R. P., Spear S. K., Holbrey J. D., Rogers R. D.: Dissolution of cellose with ionic liquids. Journal of the American Chemical Society, **124**, 4974–4975 (2002).
DOI: 10.1021/ja025790m

[18] Gericke M., Schlufter K., Liebert T., Heinze T., Budtova T.: Rheological properties of cellulose/ionic liquid solutions: From dilute to concentrated states. Biomacromolecules, **10**, 1188–1194 (2009).
DOI: 10.1021/bm801430x

[19] Xie H., Li S., Zhang S.: Ionic liquids as novel solvents for the dissolution and blending of wool keratin fibers. Green Chemistry, **7**, 606–608 (2005).
DOI: 10.1039/b502547h

[20] Hameed N., Guo Q.: Blend films of natural wool and cellulose prepared from an ionic liquid. Cellulose, **17**, 803–813 (2010).
DOI: 10.1007/s10570-010-9411-0

[21] Qin Y., Lu X., Sun N., Rogers R. D.: Dissolution or extraction of crustacean shells using ionic liquids to obtain high molecular weight purified chitin and direct production of chitin films and fibers. Green Chemistry, **12**, 968–971 (2010).
DOI: 10.1039/c003583a

[22] Barber P. S., Griggs C. S., Bonner J. R., Rogers R. D.: Electrospinning of chitin nanofibers directly from an ionic liquid extract of shrimp shells. Green Chemistry, **15**, 601–607 (2013).
DOI: 10.1039/c2gc36582k

[23] Singh N., Koziol K. K. K., Chen J., Patil A. J., Gilman J. W., Trulove P. C., Kafienah W., Rahatekar S. S.: Ionic liquids-based processing of electrically conducting chitin nanocomposite scaffolds for stem cell growth. Green Chemistry, **15**, 1192–1202 (2013).
DOI: 10.1039/c3gc37087a

[24] Silva S. S., Duarte A. R. C., Carvalho A. P., Mano J. F., Reis R. L.: Green processing of porous chitin structures for biomedical applications combining ionic liquids and supercritical fluid technology. Acta Biomaterialia, **7**, 1166–1172 (2011).
DOI: 10.1016/j.actbio.2010.09.041

[25] Phillips D. M., Drummy L. F., Naik R. R., De Long H. C., Fox D. M., Trulove P. C., Mantz R. A.: Regenerated silk fiber wet spinning from an ionic liquid solution. Journal of Materials Chemistry, **15**, 4206–4208 (2005).
DOI: 10.1039/b510069k

[26] Brandt A., Hallett J. P., Leak D. J., Murphy R. J., Welton T.: The effect of the ionic liquid anion in the pretreatment of pine wood chips. Green Chemistry, **12**, 672–679 (2010).
DOI: 10.1039/b918787a

[27] Li C., Wang Q., Zhao Z. K.: Acid in ionic liquid: An efficient system for hydrolysis of lignocellulose. Green Chemistry, **10**, 177–182 (2008).
DOI: 10.1039/b711512a

[28] Singh N., Rahatekar S. S., Koziol K. K. K., Ng T. S., Patil A. J., Mann S., Hollander A. P., Kafienah W.: Directing chondrogenesis of stem cells with specific blends of cellulose and silk. Biomacromolecules, **14**, 1287–1298 (2013).
DOI: 10.1021/bm301762p

[29] Zhang H., Wang Z., Zhang Z., Wu J., Zhang J., He H.: Regenerated-cellulose/multiwalled- carbon-nanotube composite fibers with enhanced mechanical properties prepared with the ionic liquid 1-allyl-3-methylimidazolium chloride. Advanced Materials, **19**, 698–704 (2007).
DOI: 10.1002/adma.200600442

[30] Singh C., Shaffer M. S. P., Koziol K. K. K., Kinloch I. A., Windle A. H.: Towards the production of large-scale aligned carbon nanotubes. Chemical Physics Letters, **372**, 860–865 (2003).
DOI: 10.1016/s0009-2614(03)00531-1

[31] Liang J. Z.: Effects of extrusion conditions on die-swell behavior of polypropylene/diatomite composite melts. Polymer Testing, **27**, 936–940 (2008).
DOI: 10.1016/j.polymertesting.2008.08.001

[32] Bradford P. D., Bogdanovich A. E.: Electrical conductivity study of carbon nanotube yarns, 3-D hybrid braids and their composites. Journal of Composite Materials, **42,** 1533–1545 (2008).
DOI: 10.1177/0021998308092206

[33] Haggenmueller R., Rahatekar S. S., Fagan J. A., Chun J., Becker M. L., Naik R. R., Krauss T., Carlson L., Kadla J. F., Trulove P. C., Fox D. F., DeLong H. C., Fang Z., Kelley S. O., Gilman J. W.: Comparison of the quality of aqueous dispersions of single wall carbon nanotubes using surfactants and biomolecules. Langmuir, **24**, 5070–5078 (2008).
DOI: 10.1021/la703008r

[34] Remsing R. C., Swatloski R. P., Rogers R. D., Moyna G.: Mechanism of cellulose dissolution in the ionic liquid 1-*n*-butyl-3-methylimidazolium chloride: A ^{13}C and $^{35/37}Cl$ NMR relaxation study on model systems. Chemical Communications, **2006**, 1271–1273 (2006).
DOI: 10.1039/b600586c

[35] Zhang H., Wu J., Zhang J., He J.: 1-allyl-3-methylimidazolium chloride room temperature ionic liquid: A new and powerful nonderivatizing solvent for cellulose. Macromolecules, **38**, 8272–8277 (2005).
DOI: 10.1021/ma0505676

[36] Lan W., Liu C-F., Yue F-X., Sun R-C., Kennedy J. F.: Ultrasound-assisted dissolution of cellulose in ionic liquid. Carbohydrate Polymers, **86**, 672–677 (2011).
DOI: 10.1016/j.carbpol.2011.05.013

[37] FitzPatrick M., Champagne P., Cunningham M. F.: Quantitative determination of cellulose dissolved in 1-ethyl-3-methylimidazolium acetate using partial least squares regression on FTIR spectra. Carbohydrate Polymers, **87**, 1124–1130 (2012).
DOI: 10.1016/j.carbpol.2011.08.086

[38] Celzard A., McRae E., Deleuze C., Dufort M., Furdin G., Marêché J. F.: Critical concentration in percolating systems containing a high-aspect-ratio filler. Physical Review B, **53**, 6209–6214 (1996).
DOI: 10.1103/PhysRevB.53.6209

[39] Pötschke P., Brünig H., Janke A., Fischer D., Jehnichen D.: Orientation of multiwalled carbon nanotubes in composites with polycarbonate by melt spinning. Polymer, **46**, 10355–10363 (2005).
DOI: 10.1016/j.polymer.2005.07.106

[40] Rahatekar S. S., Hamm M., Shaffer M. S. P., Elliott J. A.: Mesoscale modeling of electrical percolation in fiber-filled systems. The Journal of Chemical Physics, **123**, 134702/1–134702/5 (2005).
DOI: 10.1063/1.2031147

[41] Qi H., Chang C., Zhang L.: Effects of temperature and molecular weight on dissolution of cellulose in NaOH/urea aqueous solution. Cellulose, **15**, 779–787 (2008).
DOI: 10.1007/s10570-008-9230-8

[42] Chen X., Burger C., Fang D., Ruan D., Zhang L., Hsiao B. S., Chu B.: X-ray studies of regenerated cellulose fibers wet spun from cotton linter pulp in NaOH/thiourea aqueous solutions. Polymer, **47**, 2839–2848 (2006).
DOI: 10.1016/j.polymer.2006.02.044

[43] Jin L., Bower C., Zhou O.: Alignment of carbon nanotubes in a polymer matrix by mechanical stretching. Applied Physics Letters, **73**, 1197–1199 (1998).
DOI: 10.1063/1.122125

[44] Zhou W., Vavro J., Guthy C., Winey K. I., Fischer J. E., Ericson L. M., Ramesh S., Saini R., Davis V. A., Kittrell C., Pasquali M., Hauge R. H., Smalley R. E.: Single wall carbon nanotube fibers extruded from super-acid suspensions: Preferred orientation, electrical, and thermal transport. Journal of Applied Physics, **95**, 649–655 (2004).
DOI: 10.1063/1.1627457

eXPRESS Polymer Letters Vol.8, No.3 (2014) 164–176
Available online at www.expresspolymlett.com
DOI: 10.3144/expresspolymlett.2014.20

PMMA/SAN and SAN/PBT nanoblends obtained by blending extrusion using thermodynamics and microrheology basis

L. C. Costa[1*], *A. Ternes Neto*[1], *E. Hage*[2]

[1]Materials Science and Engineering Graduate Program, Federal University of São Carlos 13565-905 São Carlos, SP, Brazil
[2]Department of Materials Engineering, Federal University of São Carlos 13565-905 São Carlos, SP, Brazil

Received 1 August 2013; accepted in revised form 22 October 2013

Abstract. Styrene-Acrylonitrile (SAN) copolymer has been blended to poly(methyl methacrylate) (PMMA) and to poly(butylene terephthalate) (PBT) to obtain polymer nanoblends based on thermodynamics and microrheological aspects. PMMA/SAN and SAN/PBT blends show miscibility windows for a specific range of acrylonitrile (AN) content in the SAN copolymer. The phase diagram for both blends has been calculated using the interaction energy density parameter B as function of AN content in the SAN. A critical interaction energy density parameter, B_{crit}, was also calculated to find the miscibility window for both SAN blends. For some of the used SAN in the blends it was possible to obtain nanoblends as the AN content would allow B values close to the B_{crit}. For immiscible PMMA/SAN and SAN/PBT blends the disperse particle size was predicted using suitable equations and it was observed by transmission electron microscopy (TEM). Acrylic copolymers were used as compatibilizer to modify the interfacial tension and reduce the disperse phase dimensions. The compatibilizer has shown strong effect by reducing the interfacial tension and by preventing the coalescence effect. The compatibilized blends have shown disperse particle size within the nanoscale.

Keywords: *nanomaterials, polymer blends and alloys, nanoblends, compatibilization*

1. Introduction

Nanostructured polymer blends are polymeric systems in which the dispersed-phase domains exhibit length scales of 100 nm or less. Usually those polymer blends are referred to as nanoblends [1]. Although, the same terminology can be found in the literature to describe mixture of inorganic nanoparticles with polymer, which should mostly be referred as nanocomposites [2]. Nanoblends have been developed to be applied in electronic, membrane, sensing probes and optical applications [3–5]. There are several approaches to obtain nanoblends. Reactive extrusion has been used to produce nanostructured polymer blends based on polyamides [1]. *In situ* blend polymerization has also been used to develop several kind of nanoblends [6, 7]. Solution casting blending has been preferred to obtain nanoblends for those systems with poor thermo-mechanical stability to be prepared by melt mixing [8, 9]. The most used method to prepare nanoblends is by melt blending [10, 11]. Polymer nanoblends can be designed by two approaches, one considering thermodynamics aspects and the other one considering microrheology basis [12]. The interaction energy density parameter (B) can be used to predict polymer blends phase separation with disperse domains in the nanoscale, as proposed by Paul and Bucknall [13]. B parameter is strictly related to the Flory-Huggins

*Corresponding author, e-mail: lidiane@ufscar.br

interaction parameter χ and depends on the polymers solubility parameters δ_i. There is a critical B value (B_{crit}) for any polymer blend which is calculated according to Equation (1):

$$B_{crit} = \frac{RT}{2}\left(\sqrt{\frac{\rho_A}{(\bar{M}_w)_A}} + \sqrt{\frac{\rho_B}{(\bar{M}_w)_B}}\right)^2 \quad (1)$$

where, ρ_A, ρ_B and $(\bar{M}_w)_A$, $(\bar{M}_w)_B$ represent densities and the weight average molecular weights of polymers A an B, respectively. In addition, R and T represent gas constant and absolute temperature, respectively. For those blends whose B value is lower than B_{crit} the final state of mixing is miscible. On the other hand, those which B is larger than B_{crit} the final mixing states are immiscible. In addition, when B is larger than B_{crit}, but the difference among them is small, the disperse particle size may become small enough to reach nanoscale. By choosing adequate polymer pairs it is possible to vary B values below and above Bcrit to obtain miscible and immiscible polymer blends. Poly(methyl methacrylate)/styrene-acrylonitrile copolymer blends, PMMA/SAN, have been studied because it allows to have miscible and immiscible blends depending on the acrylonitrile (AN) content in the SAN [14–16]. There is an AN content limit in the SAN above which PMMA/SAN blends become immiscible with disperse phase in the range of nanoparticles. That is referred to as miscibility copolymer composition window. Paul and Barlow [17] have shown how to find the miscibility window for copolymer blends using a binary interaction model based in the interaction energy density parameter B. Miscibility windows for PMMA/SAN have been set for SAN copolymer containing from 9 to 35 wt% of acrylonitrile (AN) [18], depending on the SAN molecular weight. Higashida *et al*. [19] have shown the same trend for PMMA/SAN blends basing on Flory-Huggins parameter χ, however by increasing temperature of PMMA/SAN miscible blend it was possible to have a lower critical solution temperature (LCST). Shimomai *et al*. [20] have used the equation of state theory to show the PMMA/SAN miscibility window and have also predicted a LCST by increasing temperature. By changing the AN content in the SAN copolymer the B interaction parameter of the PMMA/SAN blend can be increased just above the B_{crit} value reaching an immiscible state. However, the disperse phase may show nanoscale domains size which allow to obtain nanoblends. This is one of the objectives of the present paper.

As described in the paper nanostructured blends or nanoblends can be obtained by choosing the interaction energy density paramenter B just above the critical B value (B_{crit}). That approach is based on the Thermodynamics of a homopolymer and a copolymer mixture. On the other hand, when B for any polymer blend is well above the B_{crit}, nanostructured blends can be obtained by choosing adequate microrheological parameters for the blend such as: disperse and matrix phases viscosity ratio; shear and extensional flow conditions and interfacial tension or energy. All those parameters affect the final particle size of the blend disperse phase. In addition, sometimes compatibilization is necessary to reduce the interfacial tension and to prevent the coalescence for higher disperse phase content in the polymer blend [21]. One of main rheological parameters is the viscosity ratio between the liquids, which can be determined by Equation (2) [22]:

$$\eta_r = \frac{\eta_d}{\eta_m} \quad (2)$$

where η_d and η_m are the viscosity values for the disperse and matrix phase at the mixing temperature, respectively. For simple shear flow at small Newtonian liquid deformations, the particle diameter D, due the drop breakup, can be determined by balancing interfacial tension (Γ) and shear forces ($\dot{\gamma}\eta_m$), as shown in Equation (3):

$$D = \frac{4\Gamma(\eta_r + 1)}{\dot{\gamma}\eta_m\left(\frac{19}{4}\eta_r + 4\right)} \quad (3)$$

where $\dot{\gamma}$ is the shear rate and η_m is the matrix phase viscosity. The above equation is valid for $\eta_r < 2.5$. Wu [23] has modified it to represent drop breakup in polymer blends. Thus the previous equation becomes Equation (4):

$$D = \frac{4\Gamma(\eta_r)^{\pm 0.84}}{\dot{\gamma}\eta_m} \quad (4)$$

where 0.84 is a empirical exponent and the plus (+) sign applies for $\eta_r > 1$, while minus (–) sign applies to $\eta_r < 1$. Equation (4) is applied to compositions lower than 15 wt% of the disperse phase and $\dot{\gamma}$ close to 100 s^{-1}. In addition, Sundararaj and Macosko [22] have extended it to include viscoelastic effects during the polymeric drop breakup. It was established a critical capillary number value, C_{acrit}, above which drop breakup for polymer blends will occur leading

to disperse particle diameter size D, estimated by Equation (5):

$$D > \frac{2\Gamma C_{acrit}}{(\eta_m \dot{\gamma} - N_1)} \quad (5)$$

where, N_1 represents the first normal stress difference due to the elastic forces during polymer mixing. C_{acrit} can be estimated as approximately 0.5 for $0.1 < \eta_r < 1$. By optimizing shear and extensional flow conditions, as well as, reducing as much as possible the interfacial energy, Γ, it is possible to obtain disperse particle size in the range of nanoscale. In addition, it is necessary to prevent as much as possible the particles coalescence, which can be done through compatibilization and for lower contents of the disperse phase component. Li and Shimizu [10] have obtained nanoblends from poly(vinylidene fluoride) (PVDF) by melt mixing. Polyamide 11 (PA11) particle size in the range of 20 to 100 nm was obtained at very high shear. Similar morphology was obtained for acrylic rubber (ACM) in PVDF blends [24]. Lumlong *et al*. [25] have obtained very small disperse particles for poly (butylene terephthalate)/SAN blends, PBT/SAN, under certain shear conditions and for lower disperse phase content.

The main contribution of this work is to obtain nanoblends by choosing either adequate thermodynamics parameters such as the interaction energy density parameter B or adequate microrheological parameters such as viscosity ratio and interfacial energy. The latter one can be reached by using compatibilizers. There are few works about nanoblends in the literature obtained from melt mixing and none using that approach.

2. Experimental

2.1 Materials

PMMA was supplied by UNIGEL, Brazil, as Acrigel® DHLEP, SAN copolymer samples were supplied by BASF, Brazil, as LURAN® 358N and 388S, PBT was supplied by SABIC Innovative Plastics, Brazil, as Valox® 325. Table 1 shows the properties of the materials used in this study. An acrylic compatibilizer based on methyl methacrylate (MMA), glycidyl methacrylate (GMA) and ethyl acrylate (EA) comonomers was synthesized through bulk copolymerization at 60°C for 1 hour. MMA was supplied by Sheet Cril, Brazil, while GMA and EA were supplied by Sigma-Aldrich, Brazil. Azobisisobutyronitrile (AIBN), used as initiator, was by DuPont Brazil as Vazo® 64. MMA comonomer was previously distilled under vacuum. The acrylic copolymer, referred as MGE, was obtained with the composition MMA 88 wt%, GMA 10 wt% and EA 2 wt%, as used by Hale *et al*. [26]. EA comonomer was mainly used in the copolymer as a stabilizer to prevent molecular unzipping scissions. Two MGE samples were synthesized to give low and higher molecular weight samples, MGE 1 and MGE 2 respectively. Table 1 shows the main characteristics of all materials used in this study.

2.2. Processing conditions

All polymer blends were prepared by melt mixing using a co-rotated intermeshing twin screw 19 mm

Table 1. Characteristics of the materials used in this study.

Materials	MFI [g/10 min][a]	$\bar{M}_n$ [g/mole][b]	$\bar{M}_w$ [g/mole][b]	$\bar{M}_w / \bar{M}_n$	AN [%][e]	[COOH] [meq/(K·g)][f]
PMMA	4.6	75 670	113 350	1.5	–	–
SAN 24 (LURAN 358N)	7.5	107 440	156 860	1.5	24	–
SAN 31 (LURAN 388S)	2.6	166 050	321 200	1.9	31	–
PBT (Valox 325)	14.0	39 175[c]	45 000[d]	–	–	45.3
MGE 1	–	13 950	81 810	5.9	–	–
MGE 2	–	26 370	102 720	3.9	–	–

[a]ASTM D1238: 230°C and 3.8 kg;
[b]GPC: THF and 40°C;
[c]Viscosimetry: Borman method [27];
[d]Based on polycondensation molecular weight polydispersivity index;
[e]Elementar analysis;
[f]Titration: Pohl method [28]

diameter extruder from B&P Process Equipment and Systems, U.S.A., model MP19, with *L*/*D* as 25. All materials were previously dried under vacuum at 60°C. The PMMA/SAN blends were melt blended in the extruder using a temperature profile from 180 to 220°C and 170 rpm as screw speed, while the SAN/PBT blends were mixed from 220 to 240°C at 140 rpm and 200 rpm. Both polymer blends were dried for 12 hours at 60°C before to be injection molded as testing specimens. The temperature profile for the injection molding was from 210 to 240°C. Table 2 shows all the prepared PMMA/SAN and SAN/PBT blends compositions.

2.3 Characterization

The blends morphology was observed by transmission electron microscope (TEM), PHILIPS, model CM120, Oregon. All samples were ultracryomicrotomed at -60°C with section thickness in the range of 30 to 50 nm. The sections of both kinds of blends were stained by ruthenium tetroxide, RuO_4, vapor. All the micrographs taken from the TEM had their particle size analysis made by Image-Pro Plus. At least 300 particles were considered in the image analysis of each sample. For the PMMA/SAN blends the average particle size and its distribution were obtained using equivalent diameter particle size and considering the projected disperse phase area. On the other hand, for SAN/PBT blends ellipses were considered to measure the shorter axis (*B*). In addition, the equivalent diameter was also calculated from the particles projected area (D_n).

Shear viscosity data for the studied materials was obtained by capillary rheometry using an INSTRON capillary rheometer, model 4467, Massachusetts, U.S.A. All the viscosity measurements were done at 240°C, using a capillary die with 33 as *L*/*D*. The shear rate was swept from 100 to 30 000 s^{-1}. The interfacial tension data used for SAN 24/PBT blends were obtained from parallel plate rheometry. Viscosity values were obtained under rotational and oscillatory conditions as a function of shear rates and frequency. An ARES rheometer from Rheometric Scientific, model strain control, U.S.A., was used with a 25 mm parallel plate diameter, with shear rate in the range of 0.01 to 100 s^{-1} and oscillatory frequency in the range of 0.01 to 500 rads/s. The distance between plates was fixed as 6 mm and the strain amplitude was set in the linear viscoelastic range. All measurements were done at 240°C under dry inert nitrogen gas flow.

3. Results and discussion

Considering the PMMA/SAN and SAN/PBT blends, the interaction energy density parameter *B* was calculated as a function of the AN content in the SAN using Equation (6) for each one and plotted as function of AN content in Figure 1. The B_{crit} value, calculated from Equation (1), was also plotted in Figure 1 to show the miscibility windows for SAN blends. Parameter *B* for a homopolymer 1 (PMMA or PBT)/copolymer 2-3 (copolymer S-AN) blend can be calculated by Equation (6):

$$B = B_{12}\varphi'_2 + B_{13}\varphi'_3 - B_{23}\varphi'_2\varphi'_3 \quad (6)$$

where B_{12} represents the interaction between monomer from homopolymer 1 and comonomer 2 from copolymer 2-3. In the same way B_{13} represents interaction between monomer from homopolymer 1 and comonomer 3 from copolymer 2-3. B_{23} represents the interaction between the comonomers from copolymer 2-3. On the other hand, φ'_2 and φ'_3 represent the comonomer volume fraction contents 2 and 3 of the copolymer 2-3, respectively. For the PMMA/SAN blends B_{12} and B_{13} are represented by the interaction parameters $B_{MMA\text{-}S}$ and $B_{MMA\text{-}AN}$, respectively, while B_{23} is represented by $B_{S\text{-}AN}$. For SAN/PBT blends B_{12} and B_{13} are represented by the interaction parameters $B_{PBT\text{-}S}$ and $B_{PBT\text{-}AN}$, respectively, while B_{23} is represented by $B_{S\text{-}AN}$. The B_{ij} values for each interaction pair are shown in Table 3. On the other hand, φ'_2 and φ'_3 represents the weight fraction content of styrene (S) and of acrylonitrile (AN) comonomers in the SAN copolymer. Calculations were done considering volume fraction close to the weight fraction because all components density is quite close to 1 g/cm^3.

Table 2. Polymer blends formulations prepared by extrusion and injection molded

Materials	PMMA/SAN 24 [wt%/wt%]	PMMA/SAN 24/MGE 1 [wt%/wt%/wt%]	SAN 24/PBT [wt%/wt%]	SAN 24/PBT/MGE 2 [wt%/wt%/wt%]
SAN 24	[99/1]; [97/3]; [95/5]; [90/10]	[94/1/5]; [92/3/5]; [90/5/5]; [85/10/5]	[90/10]	[94.5/3/2.5]; [90.9/5/4.1]; [81.8/10/8.2]
SAN 31	[99/1]; [97/3]; [95/5]; [90/10]	[94/1/5]; [92/3/5]; [90/5/5]; [85/10/5]		

Table 3. Binary interaction energy density B_{ij} for styrene (S), acrylonitrile (AN), methyl methacrylate (MMA) and poly(butylene terephthalate) (PBT) pair combinations estimated at 200°C for PMMA/SAN blends and at 240°C for SAN/PBT blends [29]

Pairs ij	B_{ij} [cal/cm^3]
S-AN (200°C)	7.00
S-MMA	0.26
MMA-AN	4.45
S-PBT	0.51
AN-PBT	7.40
S-AN (240°C)	6.86

Table 4 shows the B_{crit} values for both PMMA/SAN blends, calculated using Equation (1). The interceptions of those values with the B parameter curve, as shown in Figure 1, determines the range of AN content in the SAN copolymer for the miscibility window. For the PMMA/SAN blend the range of the miscibility window is set from 13.0 up to 27.1 AN wt%, while for the SAN/PBT blend the miscibility window stays between 17.8 and 21.9 AN wt%. Considering SAN 24 and SAN 31 as copolymer components in the PMMA/SAN blends, according to the miscibility window, PMMA/SAN 24 is miscible while PMMA/SAN 31 is immiscible. On the other hand, using SAN 24 as copolymer component in the SAN/PBT blends, those blends are immiscible. In addition, for PMMA/SAN 31 the B value, 0.0619 cal/cm^3, is close to the B_{crit}, 0.0090 cal/cm^3, from which it might expected to obtain PMMA/SAN nanoblends, as proposed by Paul and Bucknall [13]. The same expectation can be extended to the SAN 24/PBT blends in which the B value, 0.0351 cal/cm^3, is even closer to its B_{crit}, 0.0277 cal/cm^3.

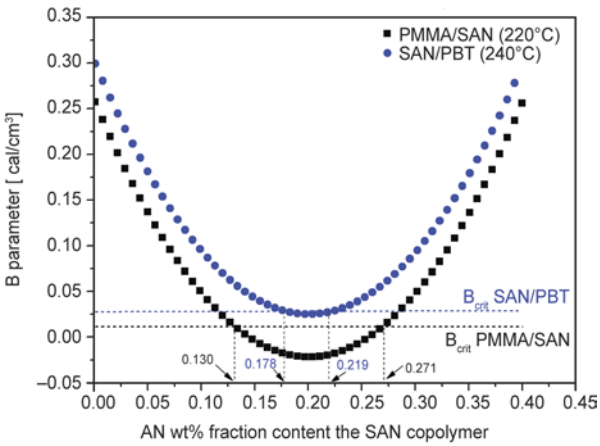

Figure 1. Interaction energy density parameter B for the PMMA/SAN and SAN/PBT blends as function of acrylonitrile (AN) content in the SAN copolymer. B_{crit}, calculated by Equation (1), has been plotted as dash straight lines to show the miscibility window for both blends.

Table 4. Critical interaction energy density parameter (B_{crit}) for both PMMA/SAN and SAN/PBT blends calculated at 200°C and 240°C, respectively

SAN blends	B_{crit} [cal/cm^3]
PMMA/SAN 24	0.0111[a]
PMMA/SAN 31	0.0090[a]
SAN 24/PBT	0.0277[b]

[a]Values calculated for the PMMA and SAN densities at 200°C
[b]SAN and PBT densities at 240°C

Figure 2 shows the TEM morphologies for PMMA/SAN 24 miscible blend. It can be observed that PMMA/SAN 24 blend stays quite as a homogeneous single phase, thereby representing a miscible blend. The RuO_4 interacts strongly with the aromatic rings from the styrene comonomer of SAN. Therefore, the dark spots observed in the images are assigned to the SAN copolymer. Figure 3 shows PMMA/SAN 31 blends TEM micrographs at different compositions. Phase separation can be observed for the PMMA/SAN 31 blends, where the dark domains are SAN 31 RuO_4 stained particles. All morphological observations seem to agree with the phase behavior which has been predicted by the thermodynamics analysis from Figure 1. Most of the SAN 31 disperse particles has size below 100 nm,

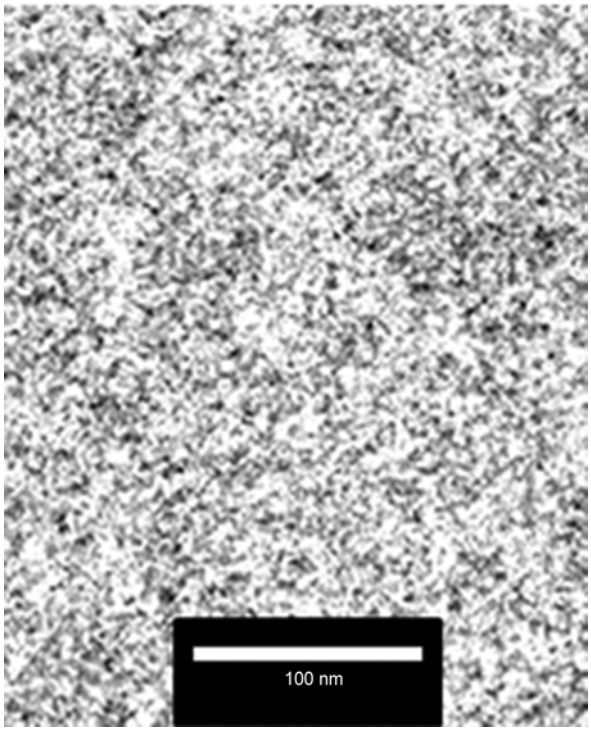

Figure 2. TEM micrographs obtained for PMMA/SAN 24 blend 90/10, as injection molded

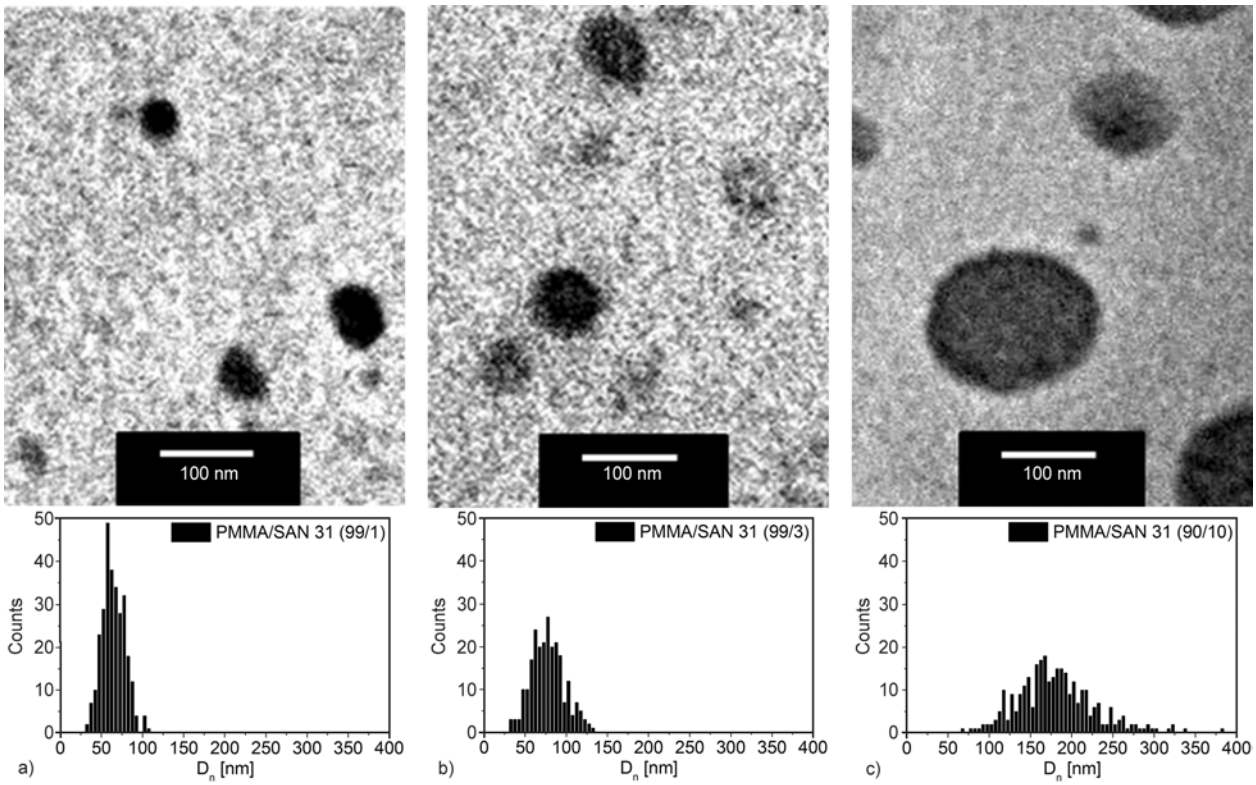

Figure 3. PMMA/SAN 31 blend TEM micrographs and particle size distribution histograms at different compositions, as injection molded: (a) 99/1; (b) 97/3; (c) 90/10

as shown in Figure 3. PMMA/SAN 31 nanoblends were mainly obtained for lower SAN 31 contents as can be observed from the respective particle size distribution histograms of the PMMA/SAN 31 nanoblend, as shown in Figure 3. At lower SAN 31 contents most of its particles are below 100 nm. The SAN 31 particle average size, obtained from the histograms in Figure 3, is shown in Table 5. As proposed by Paul and Bucknall [13] the parameter energy density $B_{\text{PMMA/SAN 31}}$ is small enough, compared to the B_{crit}, that very small particles can be obtained within the nanoscale size. As previously cited, the PMMA/SAN blends were prepared by melt mixing and injection molded. Most of the thermodynamics applied to analyze polymer-polymer miscibility is based on the mixing state equilibrium. On the other hand, polymer blending obtained by melt extrusion is well far away from the thermodynamics equilibrium due to the unstable temperature and pressure. Therefore it is surprising that the predicted thermodynamic conditions to produce nanoblends can be applied within the melt blending conditions and still obtains nanoparticles as expected. Even so, the PMMA/SAN 31 blend morphology gives results as been in the equilibrium state of mixing, at least for lower SAN 31 contents. As the amount of SAN 31 is increased in the blend, the coalescence mechanism becomes more pronounceable leading to less stable mixing, as predicted by Tokita [30].

Table 5. SAN 31 disperse phase average particle size for the PMMA/SAN 31 blends, as injection molded

PMMA/SAN 31	Average equivalent diameter [nm]	Standard deviation [nm]
99/1	63	±14
97/3	77	±20
90/10	181	±48

The blend viscosity ratio can be obtained for PMMA/SAN and SAN/PBT blends from capillary rheometry, as shown in Figure 4. All blend components have a strong pseudoplastic behavior. According to Equation (2) the viscosity ratio η_r can be calculated for any shear rate for all studied blends in this work. The PMMA matrix viscosity and the SAN 31/PMMA viscosity ratio can be observed in Table 6 for several shear rates. That viscosity ratio is close to 1. As consequence a good SAN 31 dispersion in the PMMA matrix would be expected. According to Equation (4) the particle diameter D would only depends on the interfacial tension and the rheological forces. As the shear rate increases the rheologi-

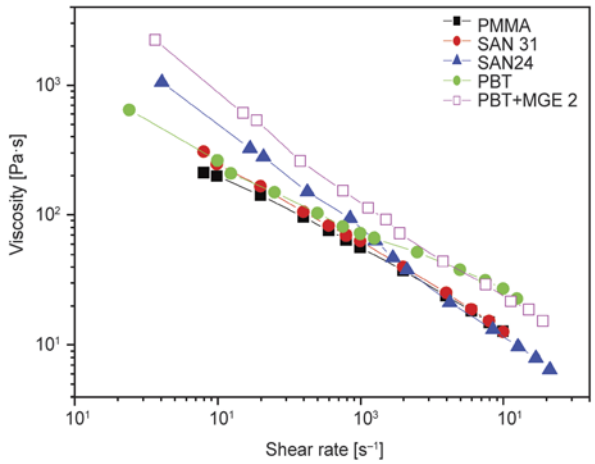

Figure 4. Apparent viscosity curves obtained from capillary rheometry for PMMA, SAN 24, SAN 31, PBT and PBT+MGE 2 measured at 240°C

Table 6. Capillary viscosity for PMMA, SAN and viscosity ratio for their blends

Shear rate [s^{-1}]	Shear viscosity [Pa·s]		Viscosity ratio $\frac{\eta_{SAN}}{\eta_{PMMA}}$	Rheological force, $\dot{\gamma}\eta_m$ [Pa]
	PMMA	SAN 31		
100	196	240	1.22	19 600
200	142	164	1.15	28 400
300	112	126	1.13	33 600
500	83	92	1.11	41 500
1000	58	63	1.09	58 000
2000	38	40	1.05	76 000
5000	21	22	1.04	105 000

cal force increases, which would reduce. The interfacial tension v_{12} can be calculated by the harmonic average equation (Equation (7)) [31]:

$$\nu_{12} = \nu_1 + \nu_2 - \frac{4\nu_1^d\nu_2^d}{\nu_1^d + \nu_2^d} - \frac{4\nu_1^p\nu_2^p}{\nu_1^p + \nu_2^p} \quad (7)$$

where v_1 and v_2 are the surface tension, while v_1^d and v_2^d are the non-polar surface tension components and v_1^p and v_2^p are the polar surface tension for components 1 and 2 of the blend, respectively. The surface tensions v_i for PMMA and SAN 31 at 20°C was obtained from Wu [23] and extrapolated for 220°C according to Ito *et al.* [32]. Both values are 24.4 and 25.1 mN/m, respectively. The polar surface tensions v_i^p were calculated for PMMA and SAN 31 by Equation (8) as 6.85 and 2.87 mN/m, respectively:

$$v_i^p = X_i^p v_i \quad (8)$$

where X_i^p is the polarity for both components, which are 0.280 and 0.110 for PMMA and SAN 31, respectively. The v_i^d is obtained as $(1 - v_i^p)$ and it is 17.53 mN/m for PMMA and 23.23 mN/m for SAN 31. As result, v_{12} can be calculated as 1.3 mN/m for the PMMA/SAN 31 blend. On the other hand, the PMMA/SAN 31 viscosity ratio can be chosen as 1.09 at shear rate close to 1000 s^{-1}, because the used range of shear rates where the PMMA/SAN melt blending was prepared has been calculated for the twin screw extruder running at 170 rpm [33]. Thus, the minimum shear rate occurs in the conveying screw section at 51 s^{-1}, while the maximum shear rate is in the kneading screw section which is 1127 s^{-1}. Considering that most of the particle breaking occurs between the kneading elements, the particle size can be estimated from Equation (4) by using the power index as +0.84. Thus the particle size D was estimated as 96.8 nm, which is within the values of D shown in Table 5. However, the estimated D through Equation (4) has not included viscoelastic effects on the drop breaking.

MGE 1 copolymer was used to modify the interfacial tension for PMMA/SAN 31 blends. Figure 5 shows the blend morphology for the ternary PMMA/SAN 31/MGE 1 blends.

The interface has changed from a sharp transition to a white halo around the SAN disperse phase, as indicated by the black arrows in the micrographs, which can be considered as an interphase. That interfacial region is certainly a MGE rich phase because it cannot be stained by RuO_4. MGE 1 has no aromatic ring in its chemical structure to be stained by RuO_4. The presence of MGE 1 has prevented the coalescence effect because it has allowed a reduction in the SAN 31 average particle size as shown in Figure 6. The SAN particle size has shown a significant reduction mainly for higher contents where the coalescence is more effective to increase the particle size. As result all SAN 31 contents have shown the average particle size in the nanoscale range. Gan and Paul [34] has predicted phase separation for SAN/MGE blends at temperatures above 185°C, when SAN has 32.3 wt% of AN and MGE has between 8 and 14 wt% of GMA. Therefore it could be expected that MGE 1, containing 10 wt% of GMA, would be immiscible with SAN 31 at temperatures above 185°C. In addition, the blending temperature in the extruder was around 220°C and the injection molding temperature was 240°C. Both temperatures are well above 185°C established by the

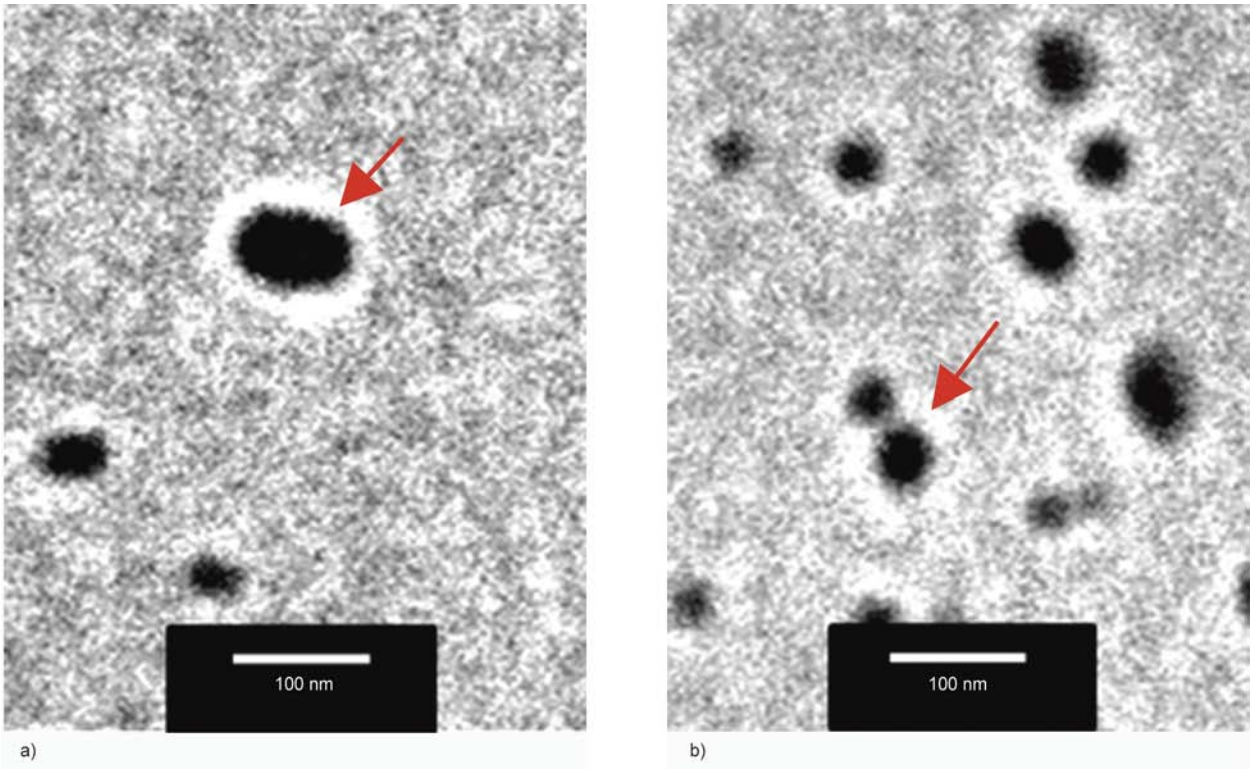

Figure 5. TEM micrographs for melt mixed PMMA/SAN 31/MGE 1 blends, injection molded at 240°C: (a) 94/1/5; (b) 92/3/5

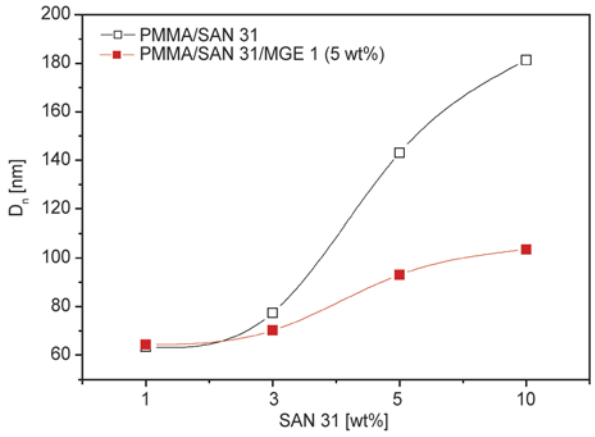

Figure 6. SAN 31 average particle size (D_n) as function of SAN 31 content in the PMMA/SAN 31 binary and ternary blends with MGE 1, for injection molded samples at 240°C

previous authors. Therefore, it might be expected to observe an immiscible SAN 31/ MGE 1 blend.

SAN 24/PBT nanoblends were obtained by melt mixing and injection molded, as result the TEM micrographs are shown in Figure 7. However, it was necessary to use MGE 2 as compatibilizer to reduce the PBT phase average particle size as shown in Figure 7b. MGE 2 copolymer is a reactive compatibilizer which has epoxy functional groups to react *in situ* mainly with COOH end groups from PBT molecules during the melt mixing. The grafted PBT-MGE molecules have segments which interact with both SAN 24 and PBT phases in the SAN 24/PBT blends and may diffuse to the interfacial region, thereby reducing its interfacial energy [26]. The average particle size for the SAN 24/PBT 90/10 blends obtained from the histograms in Figure 7a is 160±67 nm, while addition of MGE 2 has reduce it to 101±45 nm, obtained from Figure 7b. MGE 2 has shown a good efficiency to decrease the interfacial tension for the SAN 24/PBT blend, as well as, to prevent coalescence between the disperse particles. The reduction of the interfacial energy due to the presence of MGE 2 is expected to decrease the particle size as predicted by Equation (4). The evaluation of the interfacial tension for SAN 24/PBT blends was done from its viscoelastic properties, such as, dynamic modulus and relaxation time spectrum, obtained through dynamic rotational rheometry. The SAN 24/PBT blends interfacial tension is shown in Table 7 using two different models, Choi and Schowalter [35] and Palierne [36], respectively. A significant decrease in the interfacial tension can be observed by using the reactive compatibilizer MGE 2 in the SAN 24/PBT blends. That occurs when both methods are used to obtain it, as well as, both model to estimate it. That may be one of the reasons for the reduction in the disperse phase parti-

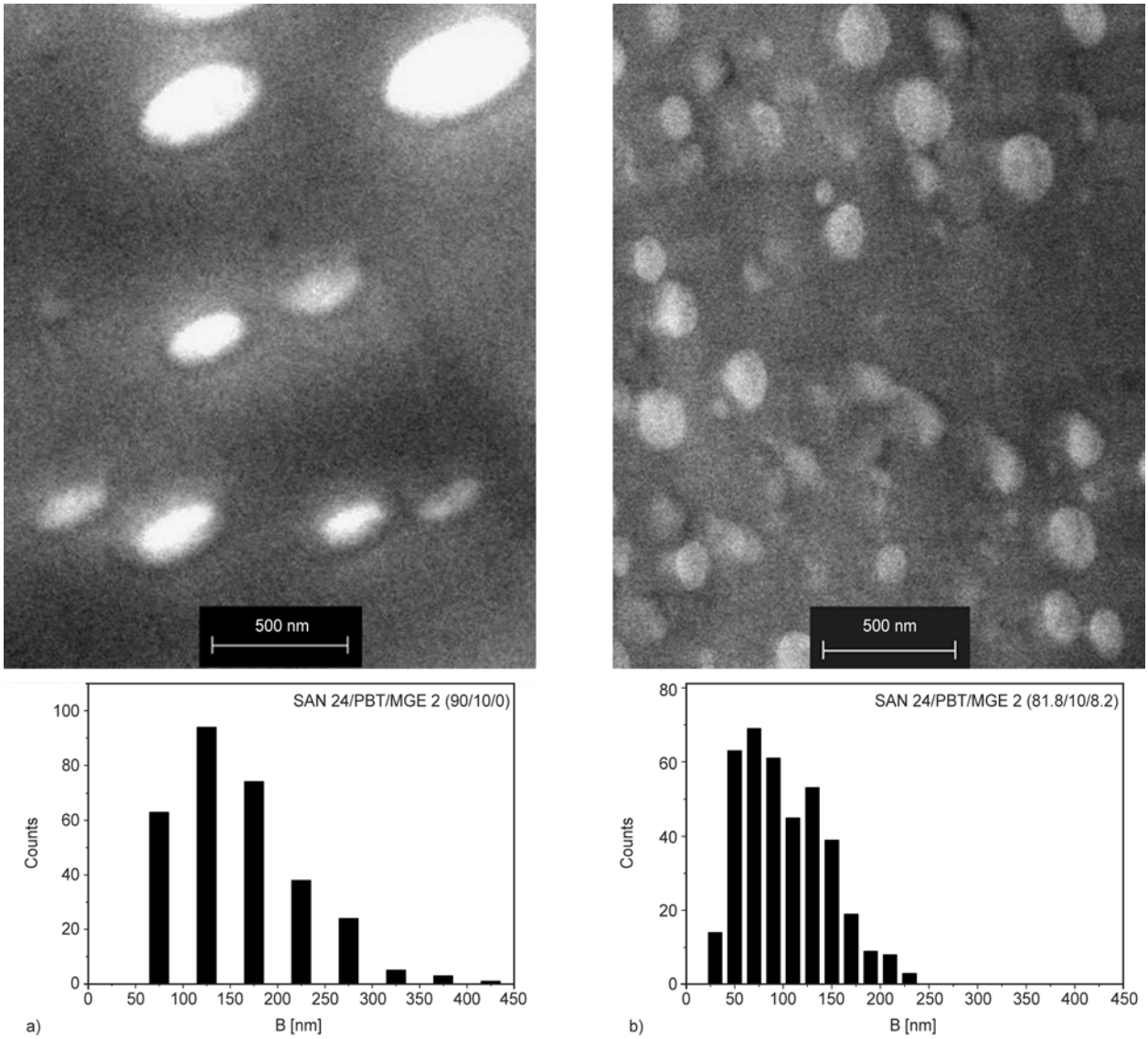

Figure 7. TEM micrographs and particle size distribution histograms for melt mixed SAN 24/PBT/MGE 2 blends, as extruded: (a) 90/10/0; (b) 81.8/10/8.2

Table 7. SAN/PBT blends interfacial energy measured by rotational rheometry

Blends	Interfacial energy based on G′ [mN/m]		Interfacial energy based on G* [mN/m]	
	Choi	Palierne	Choi	Palierne
SAN 24/PBT (90/10)	2.36	3.26	4.72	6.51
SAN 24/PBT/MGE (88.1/10/8.2)	1.60	1.66	1.47	1.52

G′: dynamic shear modulus;
*G**: complex shear modulus

cle size in those blends. However, the coalescence effect can occur simultaneously with the reduction in interfacial tension which can leave to an increase in particle size. On the other hand, as the amount of PBT phase is decreased in the SAN 24/PBT/MGE 2 blends there is lower probability for the occurrence of coalescence.

Figure 8 shows evidences of the coalescence prevention as PBT content is reduced in the SAN 24/PBT blends. The average particle size drops to values lower than 100 nm. The average particle size for lower PBT disperse phase content was 68±27 and 91±37 nm, respectively, as observed in Figure 8a and 8b. For those SAN 24/PBT compositions it was possible to obtain blends with smaller disperse particle size within the nanoscale. Coalescence effect depends basically on two parameters: number of particle collisions and the ability of a matrix film between two disperse particles to be drained out. The number of particle collisions is proportional to the square of disperse phase content and inversely

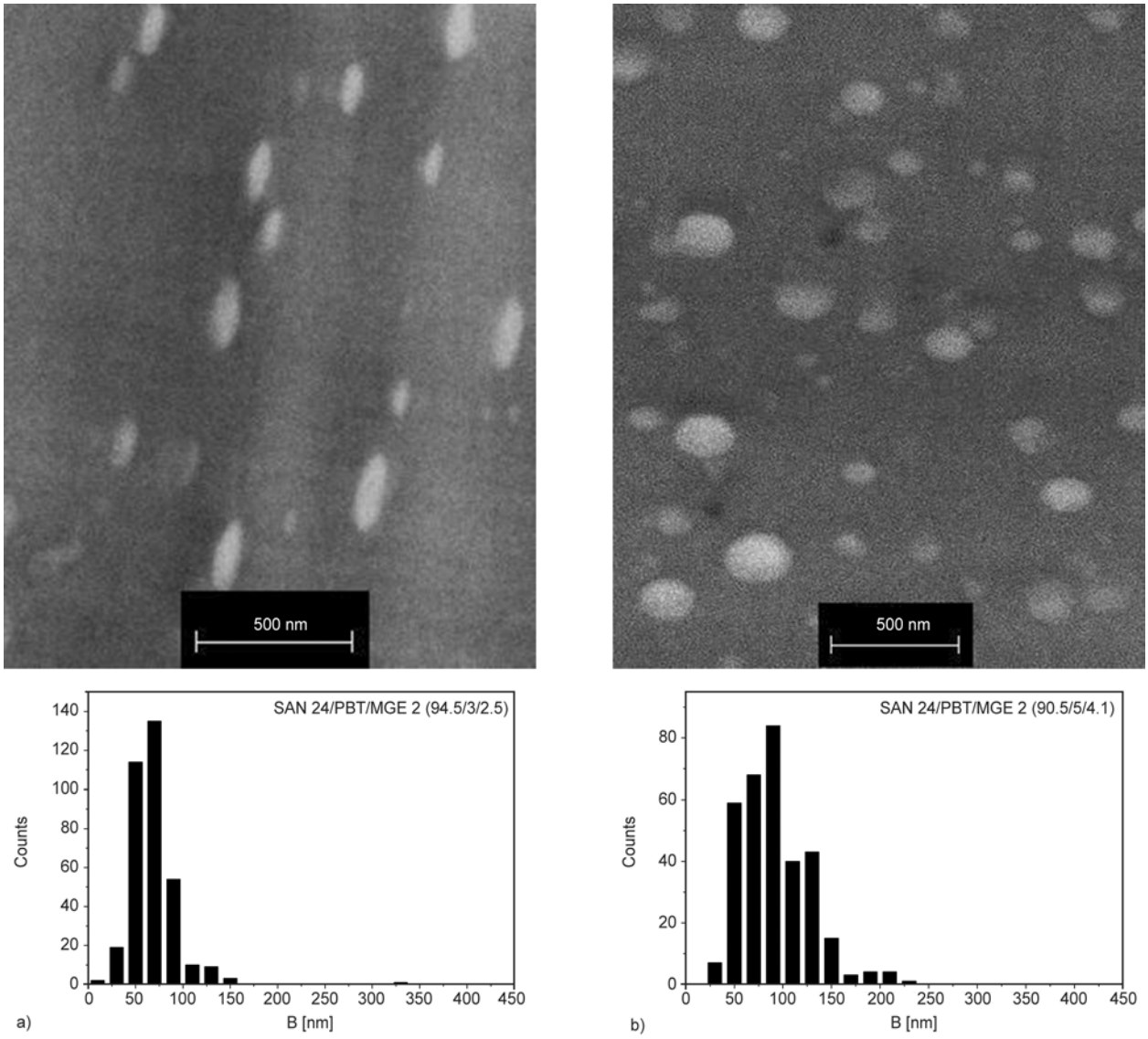

Figure 8. TEM micrographs and particle size distribution histograms for melt mixed SAN 24/PBT/MGE 2 blends, as extruded: (a) 94.5/3/2.5; (b) 90.9/5/4.1

proportional to the particle size, while the ability to drain out depends on the interfacial tension and it is inversely proportional to the matrix viscosity [37]. For lower interfacial tension values and viscosity ratio between disperse phase and matrix there is less chance to the matrix film between particles to be drained and as consequence there is coalescence suppression. From Figure 5 it is possible estimate the viscosity ratio n_r for SAN 24/PBT blends. For very low shear rates the PBT viscosity is smaller than SAN 24 viscosity. As the shear rate is increased to higher values PBT viscosity becomes closer to the SAN 24 viscosity. For very high shear rate PBT has higher viscosity than SAN 24. On the other hand, the SAN/(PBT+MGE) viscosity is higher than SAN 24 viscosity at any shear rate. Both SAN 24/PBT and SAN 24/(PBT/MGE 2) blends were melt mixed in the twin screw extruder at 140 and 200 rpm. The lowest shear rate for both screw speed were calculated in the conveying screw section as 43 and 60 s^{-1}, respectively. On the other hand, the maximum shear rates were calculated as 930 to 1330 s^{-1}, respectively, in the kneading blocks screw sections [33]. Considering that drop breaking mostly occurs in the kneading blocks screw sections with higher shear rates, the viscosity ratio is close to 1 for the SAN 24/PBT blend and is 1.8 for the SAN 24/(PBT+MGE 2), as observed in Table 8.

According to Equation (4) the PBT particle size D can be estimated as shown in Table 9, where several values for D were calculated for different shear rates and for interfacial tension obtained by different models from Table 7. The estimated particle size for tension for Palierne model and an increase in the

Table 8. Capillary viscosity for SAN, PBT and PBT/MGE and viscosity ratio for their blends

Shear rate [s^{-1}]	Capillary viscosity [Pa·s]			Viscosity ratio	
	SAN 24	PBT	PBT+MGE 2	$\frac{\eta_{PBT}}{\eta_{SAN\,24}}$	$\frac{\eta_{PBT+MG\,2}}{\eta_{SAN\,24}}$
43	999	388	1607	0.4	1.6
60	755	327	1229	0.4	1.6
930	80	82	144	1.0	1.8
1330	60	68	109	1.1	1.8

Table 9. PBT and PBT+MGE particle size estimated at different shear rates and interfacial tensions for SAN 24/PBT and SAN 24/(PBT+MGE 2) blends and obtained from TEM

Shear rate [s^{-1}]	Shear stress, $\dot{\gamma}\eta_m$ [Pa]	Viscosity ratio		Estimated particle size, D [nm]			
		$\frac{PBT}{SAN\,24}$	$\frac{(PBT + MGE\,2)}{SAN\,24}$	PBT Disperse phase		(PBT+MGE 2) Disperse phase	
				Choi[a]	Palierne[a]	Choi[a]	Palierne[a]
930	74 400	1.0	1.8	127	177	141	146
1330	79 800	1.1	1.8	128	179	132	140

SAN 24, PBT and (PBT+MGE 2) Blends composition		Average particle size [nm] Measured from TEM			
[wt%/wt%]	[rpm]	B[b]	D_n[b]	B[b]	D_n[b]
SAN 24/PBT (90/10)	200	160±67	227±99	–	
SAN 24/(PBT/MGE 2) 94.5/3/2.5)	200	–		68±27	104±42
SAN 24/(PBT/MGE 2) (90.9/5/4.2)	200	–		91±37	111±42
SAN 24/(PBT/MGE 2) (90.9/5/4.2)	140	–		58±20	86±31
SAN 24/(PBT/MGE 2) (81.8/10/8.2)	200	–		101±45	124±45

[a]The interfacial tension values used in the calculations of *D* for PBT and (PBT+MGE 2) disperse phases were 2.4 and 1.6 mN/m for Choi model and 3.3 and 1.7 mN/m for Palierne model, respectively.
[b]*B* was measured as the smaller axis of the elliptical shape of most of the disperse particles. D_n was calculated as the equivalent average diameter of the particles based on their areas.

viscosity ratio for higher shear rates, as observed in Table 8. The reduction in the particle size by using the Palierne model for compatibilized blends is due to the strong reduction in interfacial tension which overcomes an increase in the viscosity ratio by considering Equation (4). On the other hand, the reduction in the interfacial tension for the compatibilized blends using Choi model it was not enough to allow enough reduction in the estimated particle size, as shown in Table 9. For all estimated values no one has shown particle size below 100 nm.

The particle dimensions measured for the SAN 24/PBT blends are well above the ones for SAN 24/(PBT+MGE 2). By considering the smaller dimension *B* any of the SAN 24 blends most of them has shown average values lower than 100 nm within the range of nano particles. Although, the average equivalent diameter D_n has shown values above 100 nm for most compatibilized blends their dimension are smaller than the estimated ones. One of the main reasons to show D_n lower than predicted one is that the component (PBT+MGE 2) has reduced the possibility to occur coalescence within the evaluated shear rates. The estimation done by Equation (4) does not take in account the coalescence effect. The grafted PBT-g-MGE molecules besides reducing the interfacial tension have hindered the coalescence among the disperse phase particles.

4. Conclusions

Nanostructured polymer blends based on SAN copolymers have been obtained. The window of miscibility was obtained for both PMMA/SAN and SAN/PBT blends. For PMMA/SAN blends the range

of AN content to have miscible blends has been found between 13 and 27.1 wt%, while for SAN/PBT blends the range was found between 17.8 and 21.9 AN wt%. By chosen SAN copolymers containing AN just above the window upper limit it was possible to obtain Immiscible blends. SAN copolymer with 24 AN wt% was chosen for PMMA/SAN immiscible blends, while a SAN with 31 AN wt% was chosen for SAN/PBT as well as immiscible blends. The disperse phase particle size was estimated for those blends using Wu equation. The experimentally measured particle size was found within the range of the estimated values. The use of acrylic compatibilizers has helped to obtain particle size within the nanoscale by strongly reducing interfacial tension.

Acknowledgements

The authors would like to thank BASF, UNIGEL, SABIC Innovative Plastics and Sheet Cril by providing SAN, PMMA, PBT and MMA, respectively. The acknowledgement should also be extended to CNPq and FAPESP, Brazilian foundations by providing the fellowships.

References

[1] Hu G-H., Cartier H., Plummer C.: Reactive extrusion: Toward nanoblends. Macromolecules, **32**, 4713–4718 (1999).
DOI: 10.1021/ma981924y

[2] Gallego R., García-López D., Merino J. C., Pastor J. M.: The effect of montmorillonite and compatibilizer quantities on stiffness and toughness of polyamide nanoblends. Polymer International, **59**, 472–478 (2010).
DOI: 10.1002/pi.2724

[3] Sundararaj U.: Micro- and nanostructured multiphase polymer blend systems: Phase and interfaces. in 'Phase morphology development in polymer blends: Processing and experimental aspects' (eds.: Harrats C., Thomas S., Groeninckx G.) Taylor and Francis, London, 133–164 (2006).

[4] Nam S. Y., Dorgan J. R.: Non-equilibrium nanoblends via forced assembly for pervaporation separation of benzene from cyclohexane: UNIFAQ-FV group contribution calculations. Journal of Membrane Science, **306**, 186–195 (2007).
DOI: 10.1016/j.memsci.2007.08.047

[5] Segal E., Tchoudakov R., Narkis M., Siegmann A., Wei Y.: Polystyrene/polyaniline nanoblends for sensing of aliphatic alcohols. Sensors and Actuators B: Chemical, **104**, 140–150 (2005).
DOI: 10.1016/j.snb.2004.05.002

[6] Alam T. M., Otaigbe J. U., Rhoades D., Holland G. P., Cherry B. R., Kotula P. G.: Nanostructured polymer blends: Synthesis and structure. Polymer, **46**, 12468–12479 (2005).
DOI: 10.1016/j.polymer.2005.10.079

[7] Ji Y., Ma J., Liang B.: A novel approach to the preparation of nano-blends of PPO/PS/PA6. Polymer Bulletin, **54**, 109–115 (2005).
DOI: 10.1007/s00289-005-0366-5

[8] Okeowo O., Nam S. Y., Dorgan J. R.: Nonequilibrium nanoblend membranes for the pervaporation of benzene/cyclohexane mixtures. Journal of Applied Polymer Science, **108**, 2917–2922 (2008).
DOI: 10.1002/app.27749

[9] Kotal M., Srivastava S. K., Paramanik B.: Enhancements in conductivity and thermal stabilities of polypyrrole/polyurethane nanoblends. The Journal of Physical Chemistry C, **115**, 1496–1505 (2011).
DOI: 10.1021/jp1081643

[10] Li Y., Shimizu H.: Morphological investigations on the nanostructured poly(vinylidene fluoride)/polyamide 11 blends by high-shear processing. European Polymer Journal, **42**, 3202–3211 (2006).
DOI: 10.1016/j.eurpolymj.2006.08.014

[11] Li Y., Shimizu H.: Fabrication of nanostructured polycarbonate/poly(methyl methacrylate) blends with improved optical and mechanical properties by high-shear processing. Polymer Engineering and Science, **51**, 1437–1445 (2011).
DOI: 10.1002/pen.21879

[12] Utracki L. A.: Polymer alloys and blends: Thermodynamics and rheology. Hanser, New York (1989).

[13] Paul D. R., Bucknall C. B.: Polymer blends: Formulation. Wiley, New York (2000).

[14] Fowler M. E., Barlow J. W., Paul D. R.: Effect of copolymer composition on the miscibility of blends of styrene-acrylonitrile copolymers with poly (methyl methacrylate). Polymer, **28**, 1177–1184 (1987).
DOI: 10.1016/0032-3861(87)90261-8

[15] Ranganathaiah C., Kumaraswamy G. N.: New method of determining miscibility in binary polymer blends through hydrodynamic interaction: The free volume approach. Journal of Applied Polymer Science, **111**, 577–588 (2009).
DOI: 10.1002/app.29046

[16] Ren L., Zhang M. Y., Wang Y. R., Na H., Zhang H. X.: Investigation on the miscibility of the blends of poly (methyl methacrylate) and poly(styrene-*co*-acrylonitrile). Journal of Applied Polymer Science, **123**, 292–298 (2012).
DOI: 10.1002/app.34336

[17] Paul D. R., Barlow J. W.: A binary interaction model for miscibility of copolymers in blends. Polymer, **25**, 487–494 (1984).
DOI: 10.1016/0032-3861(84)90207-6

[18] Suess M., Kressler J., Kammer H. W.: The miscibility window of poly(methylmethacrylate)/poly(styrene-*co*-acrylonitrile) blends. Polymer, **28**, 957–960 (1987). DOI: 10.1016/0032-3861(87)90169-8

[19] Higashida N., Kressler J., Inoue T.: Lower critical solution temperature and upper critical solution temperature phase behaviour in random copolymer blends: Poly(styrene-*co*-acrylonitrile)/poly(methyl methacrylate) and poly(styrene-*co*-acrylonitrile)/poly(ε-caprolactone). Polymer, **36**, 2761–2764 (1995). DOI: 10.1016/0032-3861(95)93654-5

[20] Shimonai K., Higashida N., Ougizawa T., Inoue T., Rudolf B., Kressler J.: Studies on miscibility in homopolymer/random copolymer blends by equation of state theory. Polymer, **37**, 5877–5882 (1996). DOI: 10.1016/S0032-3861(96)00453-3

[21] Larocca N. M., Ito E. N., Rios C. T., Pessan L. A., Bretas R. E. S., Hage. E. Jr: Effect of PBT molecular weight and reactive compatibilization on the dispersed-phase coalescence of PBT/SAN blends. Journal of Polymer Science Part B: Polymer Physics, **48**, 2274–2287 (2010). DOI: 10.1002/polb.22110

[22] Sundararaj U., Mackosco C. W.: Drop breakup and coalescence in polymer blends: The effects of concentration and compatibilization. Macromolecules, **28**, 2647–2657 (1995). DOI: 10.1021/ma00112a009

[23] Wu S.: Formation of dispersed phase in incompatible polymer blends: Interfacial and rheological effects. Polymer Engineering and Science, **27**, 335–343 (1987). DOI: 10.1002/pen.760270506

[24] Li Y., Iwakura Y., Zhao L., Shimizu H.: Nanostructured poly(vinylidene fluoride) materials by melt blending with several percent of acrylic rubber. Macromolecules, **41**, 3120–3124 (2008). DOI: 10.1021/ma7027402

[25] Lumlong S., Kuboyama K., Chiba T., Oyama H. T., Ougizawa T.: Shear effect on morphology of poly(butylene terephthalate)/poly(styrene-*co*-acrylonitrile) blends. Journal of Macromolecular Science Part B: Physics, **43**, 711–724 (2004). DOI: 10.1081/MB-120030016

[26] Hale W., Keskkula H., Paul D. R.: Compatibilization of PBT/ABS blends by methyl methacrylate-glycidyl methacrylate-ethyl acrylate terpolymers. Polymer, **40**, 365–377 (1999). DOI: 10.1016/S0032-3861(98)00189-X

[27] Borman W. F. H.: Molecular weight–viscosity relationships for poly(1,4-butylene terephthalate). Journal of Applied Polymer Science, **22**, 2119–2126 (1978). DOI: 10.1002/app.1978.070220804

[28] Pohl H. A.: Determination of carboxyl end groups in polyester, polyethylene terephthalate. Analytical Chemistry, **26**, 1614–1616 (1954). DOI: 10.1021/ac60094a024

[29] Chu J. H., Paul D. R.: Interaction energies for blends of SAN with methyl methacrylate copolymers with ethyl acrylate and *n*-butyl acrylate. Polymer, **40**, 2687–2698 (1999). DOI: 10.1016/S0032-3861(98)00499-6

[30] Tokita N.: Analysis of morphology formation in elastomer blends. Rubber Chemistry and Technology, **50**, 292–300 (1977). DOI: 10.5254/1.3535144

[31] Hong Z., Shaw M. T., Weiss R. A.: Effect of shear flow on the morphology and phase behavior of a near-critical SAN/PMMA blend. Macromolecules, **31**, 6211–6216 (1998). DOI: 10.1021/ma980637r

[32] Ito E. N., Ueki M. M., Bretas R. E. S., Hage Junior E.: Interfacial tension of PBT/SAN blends by the drop retraction method. Materials Research, **11**, 165–169 (2008). DOI: 10.1590/S1516-14392008000200009

[33] Beatrice C. A. G., Branciforti M. C., Alves R. M. V., Bretas R. E. S.: Rheological, mechanical, optical, and transport properties of blown films of polyamide 6/residual monomer/montmorillonite nanocomposites. Journal of Applied Polymer Science, **116**, 3581–3592 (2010). DOI: 10.1002/app.31898

[34] Gan P. P., Paul D. R.: Interaction energies for blends based on glycidyl methacrylate copolymers. Polymer, **35**, 3513–3524 (1994). DOI: 10.1016/0032-3861(94)90917-2

[35] Choi S. J., Schowalter W. R.: Rheological properties of nondilute suspensions of deformable particles. Physics of Fluids, **18**, 420–427 (1975). DOI: 10.1063/1.861167

[36] Palierne J. F.: Linear rheology of viscoelastic emulsions with interfacial tension. Rheologica Acta, **29**, 204–214 (1990). DOI: 10.1007/BF01331356

[37] Gramespacher H., Meissner J.: Interfacial tension between polymer melts measured by shear oscillations of their blends. Journal of Rheology, **36**, 1127–1141 (1992). DOI: 10.1122/1.550304

eXPRESS Polymer Letters Vol.8, No.3 (2014) 177–186
Available online at www.expresspolymlett.com
DOI: 10.3144/expresspolymlett.2014.21

Preparation and characterization of polyamide 6 nanocomposites using MWCNTs based on bimetallic Co-Mo/MgO catalyst

A. J. Hassani[1], *Z. A. Mohd Ishak*[2,3], *A. R. Mohamed*[1*]

[1]Chemical Engineering School, Engineering Campus, Universiti Sains Malaysia, Seri Ampangan, 14300 Nibong Tebal, Penang, Malaysia
[2]School of Material and Mineral Resources Engineering, Engineering Campus, Universiti Sains Malaysia, Seri Ampangan, 14300 Nibong Tebal, Penang, Malaysia
[3]Cluster for Polymer Composites, Science and Engineering Research Centre, Engineering Campus, Universiti Sains Malaysia, Seri Ampangan, 14300 Nibong Tebal, Penang, Malaysia

Received 6 August 2013; accepted in revised form 28 October 2013

Abstract. Multiwalled carbon nanotubes (MWCNTs) based on bimetallic Co-Mo/MgO catalyst were produced in large scale by catalytic chemical vapor deposition method (CCVD) of methane. X-ray diffraction (XRD), transmission electron microscopy (TEM), thermogravimetric analysis (TGA) and Raman spectroscopy proved carbon nanotube (CNT) formation. As-produced multiwalled carbon nanotubes (PCNTs) and commercial ones (CCNTs) with the same diameter (10–20 nm) were melt blended with polyamide 6 (PA6). XRD patterns of nanocomposites showed applying 0.1% of both types of CNTs changed the crystalline structure of neat PA6 from α/γ form to thermodynamically more stable α-phase structure. Differential scanning calorimetry (DSC) showed both types of CNTs shifted crystallization temperature of about 10–15°C to higher temperature due to the nucleating effect of nanotubes. Furthermore, degree of crystallinity increased by about 30% in some composites, especially for PCNTs. Nanocomposites containing PCNTs exhibited improvements in thermal decomposition temperature in comparison with CCNT nanocomposites. Nanocomposites melt viscosity increased at high CNTs loading due to the filler-matrix entanglements.

Keywords: *nanocomposites, mechanical properties, thermal properties, carbon nanotube, polyamide*

1. Introduction

MWCNTs with extraordinary mechanical, electrical and thermal properties were first ever observed by Iijima [1]. Nowadays, several different processes such as chemical vapour deposition (CVD) of hydrocarbons, arc discharge, laser ablation, solar carbon vaporization and carbon electrode electrolysis in ionic salts melts are employed to prepare CNTs. Large quantity production of CNTs with high quality and selective diameter and length is the main challenge in carbon nanotube technology. Decomposition of hydrocarbons over transition metals or their compound at the moderate temperatures is one of the simplest routes to prepare CNTs in large scale and low cost. Crystalline quality and defects on the individual CNTs affect CNTs properties. Commonly, the CVD process yields a lot of entanglements in the resulting CNTs in comparison to other methods. Because of the large surface area, high aspect ratio and above-mentioned properties, CNTs are one of the best candidates for reinforcing phase in polymeric matrices. In situ polymerization [2], solution casting [3] and melt processing [4] are applied to distribute and disperse CNTs in thermoset and/or

*Corresponding author, e-mail: chrahman@eng.usm.my

thermoplastic based nanocomposites. Semi-crystalline engineering thermoplastic PA6 is used in many applications, i.e. automotive, aerospace, textiles, electrical and electronics industries. PA6/nanoclay nanocomposites have been investigated intensively in the last decade [5]. In addition, recently, the number of investigations on CNT/PA nanocomposites including modified and unmodified CNTs is increasing. Several researches have also been reported considering different aspects of thermal, mechanical, electrical and rheological properties of nanocomposites which have used in situ polymerization, solution casting, melt spinning and melt compounding methods [3, 4, 6–9].

Melt mixing of CNTs and thermoplastic matrices by single screw [10, 11] or twin screw extruder [6, 12–14] is the most economical and desirable approach in comparison with other methods because, for fabricating these composites no additional equipment is needed. This process can be performed with conventional plastic machines, i.e. injection molding and extrusion. In addition, for large-scale production of carbon nanotube composites, in situ polymerization needs new mixing and conveying technology in upstream production lines and in some cases change of reactor type and its design would be required. In solution method, a lot of solvents are necessary and recovery of solvent and contaminants in the final product can affect the properties of the product. However, in some cases there would be no any other method to obtain a desired product.

Rangari *et al*. [10] reported that the tensile strength of PA6 fibre nanocomposites prepared by a single screw extruder, enhanced by 230% which contained only 1 wt% unmodified CNTs, while De Zhang *et al*. [6] indicted that tensile strength improved by about 124% with the same CNTs loading using twin – screw mixer. Phang *et al*. [14] have studied the effect of CNTs on crystallinity of the polymer matrix prepared via melt compounding. They found that CNTs changed polymer crystalline structure and α-phase crystalline structure forms independently from cooling rate and annealing conditions. This behaviour is completely different from PA/nanoclay nanocomposites. Sun *et al*. [15] have compared different nanoparticles behaviour in PA6. They found that different nanoparticles change the crystallization temperature peak to higher temperature due to nucleating effect of montmorillonite, SiO_2 and CNTs. They have also reported that CNTs induce α-phase crystalline structure.

Our research group has been working on the synthesis of CNT for several years [16–18] and have synthesized MWCNTs with different aspect ratios and purity on various catalysts. Specifically, recently, we have produced CNT on a pilot plant scale [19]. In the present study, MWCNTs were produced using the catalytic chemical vapor deposition (CCVD) method on bimetallic Co-Mo/MgO catalyst in a rotary tubular reactor. PA6/CNT nanocomposites at different loading of CNTs have been prepared by melt mixing technique. The focus has been on investigating and comparing the effect of as-produced CNTs and commercial ones on mechanical, rheological, morphological and thermal properties of the PA6 matrix.

2. Material and methods

2.1. Materials

PA6 pellets (CM1017-Toray, Japan) were used in this study. The melt flow index (MFI at 230°C and 2.16 kg load) and density of PA6 were 35 g/10 min and 1.14 g/cm^3, respectively. Commercial MWCNTs with ~95% purity were purchased from Shenzhen Nanotech Port Co. Ltd (NTP), China. The diameter, length, special surface area and thermal conductivity of CCNT were 10–20 nm, 5–15 μm, 40–300 m^2/g and ~2000 W/(m·K), respectively. Ammonium molybdate tetrahydrate, citric acid, cobalt(II) nitrate and magnesium nitrate were purchased from a local supplier, Kumpulan Saintifik F.E. Sdn, Bhd. (KSFE), Malaysia.

2.2. Carbon nanotube preparation

The MWCNTs were prepared by chemical vapor deposition of methane on bimetallic Co-Mo/MgO catalyst [19]. Briefly, materials were accurately weighed and dissolved in a proper amount of water and mixed at 90°C to form a purple gel. After that, the gel was dried at 120°C overnight. Foamed material was ground in a mortar, and it was calcined at 700°C for two hours. Prepared catalysts were sieved and were used to prepare MWCNTs. Then, the catalyst was continuously fed into the rotary reactor system and the reaction occurred in the reactor tube at 800°C. A residence time of 1 hr was chosen by screw conveyor speed controlling. Deposited carbonaceous material on the catalyst was collected in the reservoir that fixed at the end of the reactor.

2.3. Nanocomposite preparation

PA6 and two types of CNTs were dried at 80°C for 15 h before melt compounding. Melt blending was performed on a single screw extruder (Brabender KE19/25 D) at 35 rpm in different CNT loadings for both types of CNTs. Operating temperatures at different zones from the hopper to die were 225, 230, 235 and 230°C respectively. Nanocomposites were obtained with CCNTs and PCNTs at 0.1, 0.2, 0.5, 1, 2 and 3 wt% loading. After melt mixing, nanocomposites of 1 mm thickness were prepared by compression molding at 250°C and 100 bars by using a Gotech KT-7014A press. Prior to hot press, samples were put in the vacuum for 15 h at 80°C.

2.4. Differential scanning calorimetry (DSC)

Differential scanning calorimetry experiments were performed by a Mettler Toledo DSC-1 instrument using Stare software under nitrogen atmosphere. Samples of about 10 mg were accurately weighed and placed in an aluminium pan. Then the pan was heated from 25 to 250°C at a heating rate of 10°C/min. Prior cooling to room temperature samples were maintained for 4 min at 250°C to erase previous thermal history. Then, the cooling was done at the same heating rate from 250°C to room temperature. This process was performed for another cycle, and data was recorded for the last cycle.

Crystallinity content can be calculated using Equation (1) [20]:

$$X_c = \frac{\Delta H_f}{\Delta H_f^0 \omega_{PA6}} \times 100 \quad (1)$$

where ΔH_f^0 is heat of fusion [J/g] for a theoretical completely (100%) crystalline PA6, reported in the literature to be about 190.8 J/g [21], ΔH_f is the experimentally measured fusion heat of nanocomposite by DSC and ω_{PA6} is the PA6 weight fraction in the nanocomposites.

2.5. X-ray Diffraction (XRD)

XRD measurements of the nanocomposites, neat PA6, PCNTs and CCNTs were carried out in reflection mode with a D5000 diffractometer (Siemens) using CuK_α radiation at a scan rate of 0.3°/min in a 2θ range of 10–30°, and operated at 20 mA and 30 kV.

2.6. Mechanical properties

Tensile samples were punched from sheets according to ASTM D638 type IV. The testing with a cross-head speed of 50 mm/min was carried out on an Instron 3367 universal testing machine to measure tensile modulus, strength and elongation at break. All samples were dried at 80°C for 15 h prior to testing.

2.7. Thermogravimetric analysis

TGA (TA Instrument, SDT Q600) was done for CCNTs, PCNTs, neat PA6 and prepared nanocomposites, both in air and nitrogen atmosphere from room temperature up to 700°C. Heating rate of 10°C/min was chosen.

2.8. Melt flow index

MFI was performed in the Dynisco Melt Flow Indexer according to ASTM D1238 (235°C and 1 kg). All samples were dried at 80°C for 15 h before rheological measurements.

3. Results and discussion

3.1. Carbon nanotube characterization

Figure 1a shows TEM image of PCNTs obtained on the bimetallic catalyst. It can be seen that deposited materials are rope-like carbon nanostructures with hollow core, and their average diameters are about 10–20 nm. TGA profiles of PCNTs and CCNTs are shown in Figure 1b. It can be seen that about 60% carbonaceous materials are grown on the catalyst in the final product. Amorphous carbon content is about 5% (loss weight at about 350°C). High thermal stability (>500°C) confirms the carbon nanotube formation. TGA reveals that PCNTs are more thermodynamically stable than CCNTs and their decomposition temperature is at least 60°C higher than CCNTs. Raman spectroscopy of PCNTs (Figure 1c) shows two main peaks at 1594 and 1326 cm^{-1}. The 1585 cm^{-1} peak corresponds to G-band characteristic feature of the graphitic layers that are related to the tangential vibration of the sp^2 carbon atoms. The second peak is a typical sign for defective graphitic structures (D-band). G-band and D-band peaks for CCNTs are at 1595 and 1332 cm^{-1}, respectively. Generally, D to G band intensity ratio (I_D/I_G) is used as a criterion for quality determination of

synthesized CNT. The higher ratio shows more amorphous carbon on the surface of CNTs and/or more disorders in carbon nanotubes. I_D/I_G of PCNTs and CCNTs were 1.54 and 1.37 respectively. Higher value for PCNTs arises from more amorphous carbon which can be seen in the DTG curve between 300 to 400°C. Oxidation of PCNTs in the air for 2 hr reduced D-band to G-band intensity to 1.17 which shows amorphous carbon can strongly influence the intensity of disorder band in the CNTs.

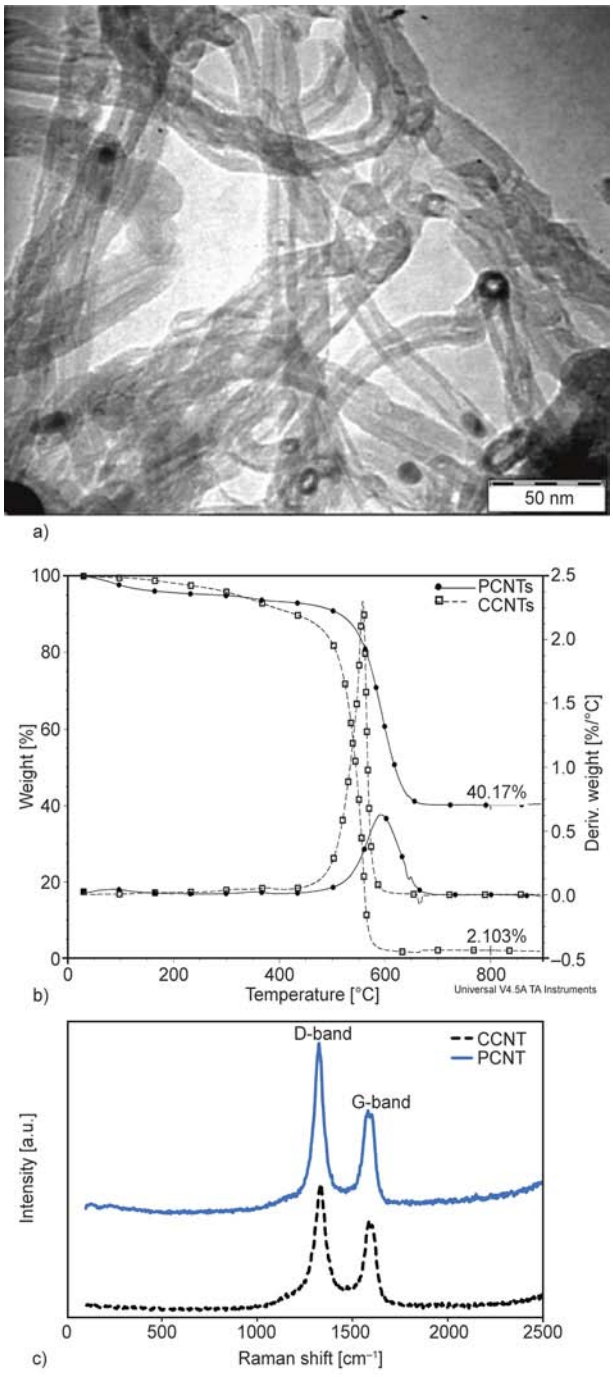

Figure 1. a) TEM of PCNTs, b) TGA curves, and c) Raman spectra of PCNTs and CCNTs

3.2. Nanocomposite properties

Crystallization behaviour of neat PA6 and its nanocomposites were studied to analyze MWCNTs effect in the PA6 matrix. The cooling process used in this study is similar to the real manufacturing process, i.e. injection moulding, extrusion and fibre spinning. Figure 2 shows cooling and heating curves for PA6 and its composites. Crystallization peak and its onset, melting peak and its onset as well as the degree of crystallinity are presented in Table 1. It can be seen that with increasing both PCNTs and CCNTs loading in composite, crystallization peak is shifted to higher temperatures. This indicates that CNTs act as nucleating agents in the polymer matrix. It can be also seen with increasing both types of CNTs in the continuous phase, more heterogeneous nucleation sites are available, and hence more polymer chains are induced to crystallize. Indeed more CNTs in polymer increase crystallization temperature. The degree of crystallinity is significantly increased by using 0.2% of carbon nanotube for both types of CNTs. The reduction in the degree of crystallinity with the CNT loading of more than 0.2% implies that CNTs could act as an efficient nucleating agent at low concentrations. Their nucleating ability gradually reduced at high content. However, it is worth mentioning that the degree of crystallinity of nanocomposites at high CNT loadings is still more than neat PA6 indicating the occurrence of the nucleation process at high CNT content. Randomly dispersed MWCNs at higher concentrations can restrict

Table 1. Melting peak (T_m) and its onset, crystallization peak (T_c) and its onset and, crystallinity percent of neat PA 6 and nanocomposites

Samples	T_m		X_m* [%]	T_c	
	Onset	Peak		Onset	Peak
PA 6	207.0	221.1	30.3	186.4	181.0
CCNT-0.1%	208.3	220.5	30.5	197.4	192.7
CCNT-0.2%	207.9	220.5	37.2	198.6	193.3
CCNT-0.5%	207.6	220.6	37.3	200.2	193.9
CCNT-1%	206.9	220.8	32.9	201.7	193.8
CCNT-2%	206.4	220.6	34.8	202.7	194.4
CCNT-3%	205.9	220.5	31.2	203.8	195.1
PCNT-0.1%	207.6	220.6	38.4	199.4	193.5
PCNT-0.2%	207.5	221.3	60.0	200.6	193.7
PCNT-0.5%	207.7	220.8	41.1	200.7	193.9
PCNT-1%	207.3	220.3	39.3	202.2	194.8
PCNT-2%	206.7	221.0	49.4	203.8	195.1
PCNT-3%	206.7	220.9	38.0	204.6	195.7

*Normalized crystallinity according to Equation (1)

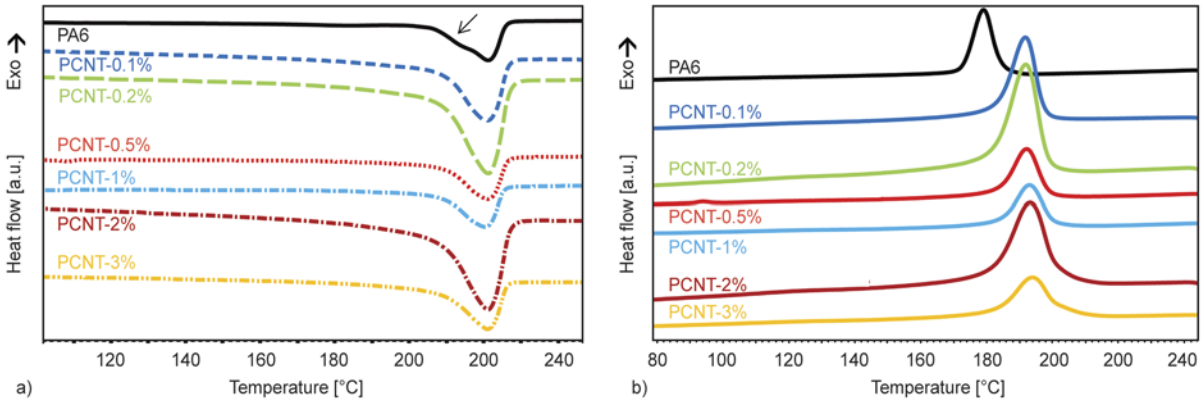

Figure 2. DSC thermograms of neat PA6 and its nanocomposites containing different loadings of PCNTs; a) heating curves, b) cooling curves

crystals and thus the crystal growth rate will be retarded [22].

Table 1 shows that PCNTs possessed a relatively higher degree of crystallinity than CCNTs. This may be attributed to better interaction between the catalyst in PCNTs and the polar amide group in PA6 chains. Another possible reason is the existence of more entanglement in PCNTs in comparison to CCNTs according to higher D-band to G-band intensities that could act as nodes to make more nucleating agents and consequently, such nodes can increase the degree of crystallinity. Melting point temperature will decrease at high content CNTs because of high thermal conductivity of CNTs that facilitate heat transfer into the crystalline parts and hence melting would happen at a lower temperature. Neat PA6 shows a broader peak and a small shoulder around 215°C which corresponds to γ-crystalline form. This is in agreement with the observation obtained by XRD that will be discussed later.

The XRD spectra of PA6, PCNTs, CCNTs and all nanocomposites are presented in Figure 3. It can be seen neat PA6 has a sharp peak at 21.4° that corresponds to pseudohexagonal γ-crystalline form as dominant phase and two short shoulders at approximately 2θ = 20 and 23.7° for the α-crystalline form [23]. For both types of the CNTs (002) diffraction plane is observed at around 2θ ≅ 26° that confirms graphitic planes in their structure [24, 25]. Two main peaks are observed for all 12 nanocomposites at about 2θ = 20.5°±0.1 and 2θ = 23.9°±0.1where correspond to (200), (002) and (220) [26, 27] or (100), (010) and (110) [28] reflections which are characteristic of the α-crystalline form. These peaks depict induced α-form crystalline microstructure by PCNTs and CCNTs in the nanocomposites. It is known that structure changing of material affects physical and mechanical properties. Here, metastable γ-crystalline form involving orderless hydrogen bonding among parallel chains in neat PA6 is converted to more thermodynamic stable α-from that includes sheets of hydrogen-bonded chains created between antiparallel chains by adding both types of CNTs. Indeed this behaviour is different from the normally reported

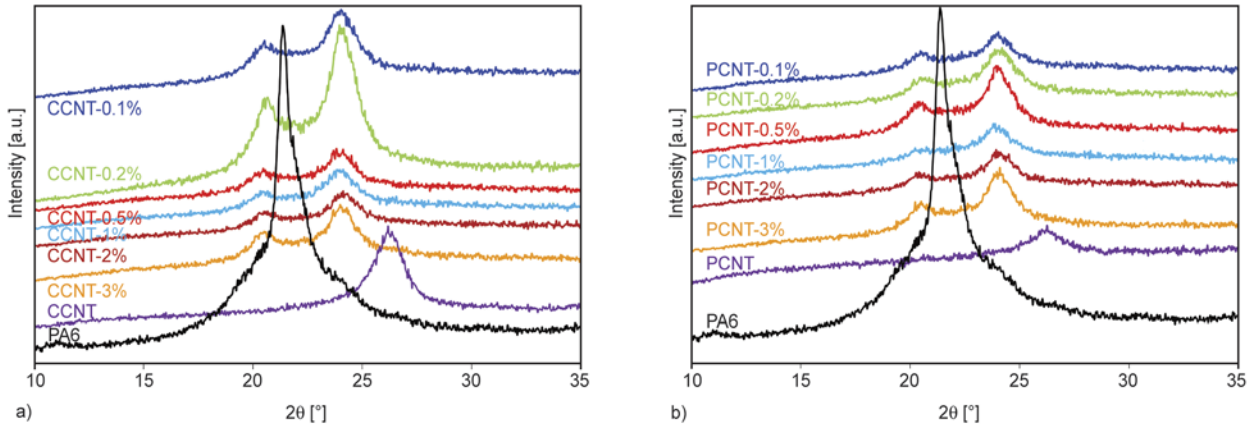

Figure 3. a) XRD patterns of PA6, CCNTs and their nanocomposites; b) XRD patterns of PA6, PCNTs and their nanocomposites

data for PA6/nanoclay nanocomposites [29]. Liu *et al*. [4] have presented the same observation in polyamide filled MWCNTs. They proposed that polymer chain movement in the presence of one-dimensional CNT is less restricted compared with two-dimensional nanoclays. Therefore, CNTs may only act as the nucleation agent for PA6 chains to create α-crystalline form. Thus, CNTs have nucleating effect in the polymer matrix. It can be seen that a small amount of CNTs (only 0.1%) increased crystallinity and changed the morphology of the polymer matrix from metastable γ-form crystal to thermodynamically stable α-form and thus, better mechanical or physical properties would be expected. Indeed CNTs change the kinetics of crystallization and this leads to a different degree of crystallinity and crystals dimensions.

Figure 4 shows the TGA behaviour of neat PA6 and its nanocomposites under air and nitrogen. Onset decomposition temperature ($T_{5\ wt\%}$) and maximum degradation temperature for neat PA6 and its nanocomposites under air and nitrogen atmosphere are presented in Table 2.

Thermal behaviour under air and nitrogen atmosphere is the same for nanocomposites and pure PA6. Decomposition of PA6 and nanocomposites containing PCNTs under air (Figure 4a) displayed a two-stage decomposition. The maximum decomposition temperatures for these two stages are summarized in Table 2. A slight change can be seen in first stage. Also, a small decreasing of decomposition temperature in second stage is observed for both types of CNT nanocomposites. This behaviour can be attributed to the high thermal conductivity of CNTs. Decomposition temperature at 5 wt% under N_2 atmosphere (Figure 4b) has been enhanced with the increasing CNTs loading. As can be seen in Table 2, thermal stability enhancement of the PA6 matrix by PCNTs is better than CCNTs. Different catalyst types, carbon nanotube heat capacity, thermal conductivity, volume fraction, aspect ratio, orientation and packing of the filler material can affect thermal

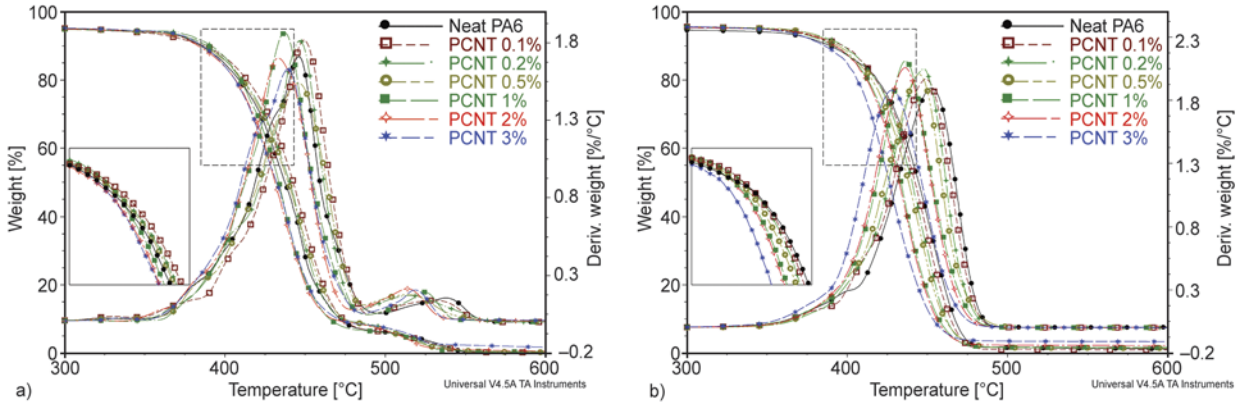

Figure 4. TGA and DTG curves of PA6 and PA6/PCNTs nanocomposites; a) under air, b) under nitrogen

Table 2. Decomposition temperature for 5, 10% weight loss and residue in air and nitrogen atmosphere and their maximum peaks

Samples	Air environment					N_2 environment			
	5 wt% [°C]	10 wt% [°C]	max1 [°C]	max2 [°C]	Residue at 600°C [%]	5 wt% [°C]	10 wt% [°C]	max [°C]	Residue at 600°C [%]
PA 6	307.1	385.1	447.6	540.7	0.5	246.2	389.6	453.0	1.2
CCNT-0.1%	266.4	386.3	446.6	523.4	0.1	321.1	392.2	452.1	0.9
CCNT-0.2%	326.9	384.2	446.6	523.4	0.1	305.4	394.7	451.9	0.9
CCNT-0.5%	292.8	388.2	445.4	539.0	0.3	337.9	397.6	454.4	0.9
CCNT-1%	307.1	384.9	447.0	535.0	0.5	324.1	395.6	453.9	1.4
CCNT-2%	358.0	399.9	448.4	521.9	0.5	337.5	394.5	453.5	2.0
CCNT-3%	299.8	389.5	450.5	500.3	0.5	332.1	393.5	455.1	3.2
PCNT-0.1%	316.0	386.8	449.8	531.4	0.2	354.2	397.6	449.7	0.9
PCNT-0.2%	298.7	391.8	446.0	516.1	0.2	356.1	397.8	443.9	1.4
PCNT-0.5%	326.9	393.3	448.3	519.3	0.2	359.9	394.7	445.9	1.4
PCNT-1%	285.6	388.7	437.2	526.8	0.4	343.8	392.2	436.8	1.6
PCNT-2%	291.4	383.3	429.7	516.0	0.5	345.6	392.3	437.9	2.2
PCNT-3%	324.5	386.1	439.2	521.1	1.7	344.9	386.1	429.1	3.3

behaviour of nanocomposites. However, after decomposition initiation, nanocomposites including PCNTs show lower degradation temperature which depends on PCNTs loading. At lower temperatures, CNTs act as heat conductive material and pass heat from the nanocomposite core to the outer surface. Therefore, the polymer chain degradation would be retarded. On the other hand, when activation energy is enough to decompose PA6, CNTs conduct heat of decomposition to other parts through the polymer matrix. In this case, nanocomposite would degrade at lower temperatures. This decomposition temperature at different PCNTs loading in constant weight loss in the range of 20 to 80% can be estimated from linear Equation (2):

$$T = \alpha \cdot \omega_{PCNT} + \beta \quad (2)$$

where T is the nanocomposite decomposition temperature in °C and ω_{PCNT} is PCNT weight percent in nanocomposites. Parameters α and β are constants obtained from degradation curves at constant weight loss. Here, parameter α is calculated as –5.4115°C and β is the decomposition temperature of neat PA6 at certain weight loss. This parameter (β) for 50% weight loss is 442.07°C.

As it is known incorporating MWCNTs in the polyamide matrix will increase the melt viscosity of the polymer melt and as a result, MFI will decrease [22, 30, 31]. MFI for neat PA6 and its nanocomposites are presented in Table 3. A slight increase in MFI of neat PA6 is observed for low CCNT loading. A similar behavior has been reported by Shen *et al*. [30]. At low CNTs concentrations MFI would not change. Even so, in high CNTs loading, MFI is decreased for both types of CNTs. This may be due to the fact that in low CNTs content, polymer chains can move easily and probably CNTs facilitate polymer chain movement due to non-polar CNTs nature. In this case CNTs could act as a barrier and hinder polar-polar interaction (i.e. hydrogen bonding) between PA6 chains. As a result hydrogen bonding will decrease among polymer chains and polymer movement take place easily. As mentioned before, MWCNTs are in entangled and rope like form. These entanglements can wrap with polymer chains and form larger entanglements. Thus the polymer chain movement in the molten state will be decreased and consequently, melt viscosity will increase. This is in agreement with the degree of crystallinity results as discussed earlier. Degree of crystallinity decreases with increasing CNTs loading more than 1% that shows nucleating sites are reduced among polymer chains. It can be resulted that CNTs form agglomerates and their dispersion is not desirable in the polymer matrix.

Table 3. MFI of PA6 and its nanocomposites containing PCNTs and CCNTs in different CNTs loading

Sample names	MFI [g/10 min]
Neat PA6	23.9±0.9
CCNT 0.1%	24.4±0.4
CCNT 0.2%	25.0±1.7
CCNT 0.5%	25.0±0.7
CCNT 1%	21.5±1.5
CCNT 2%	19.8±1.1
CCNT 3%	14.6±3.3
PCNT 0.1%	23.4±0.6
PCNT 0.2%	23.3±0.5
PCNT 0.5%	19.7±0.5
PCNT 1%	18.8±0.9
PCNT 2%	19.0±2.8
PCNT 3%	18.8±4.2

Mechanical properties of PA6 and its nanocomposite are summarized in Table 4. It can be seen that elongation at break, which is known as toughness/flexibility of the material, drastically decreased by adding both types of unmodified MWCNTs to the PA6. It is known that elongation at break can be reduced by the addition of stiff filler to the polymer matrix. Moreover, the reduction in elongation at break may be due to CNTs aggregation in the PA6 matrix that behaves like physical cross-linked points between individual CNTs. These aggregations can confine the PA6 chains mobility and consequently, reduce elongation at break of nanocomposites. It is worth mentioning that elongation at break of PCNTs nanocomposites at low content loading is higher than that of CCNTs nanocomposites. This may be due to better dispersion of PCNTs in the PA6 matrix in low concentrations that is in agreement with higher tensile strength, modulus and crystallinity. Mechanical properties of CNT composites are affected by the dispersion, orientation and aspect ratio of CNTs. The tensile strength did not increase in the presence of both types of CNTs in the polymer matrix. The rather poor reinforcement effect of CNT may be attributed to undesirable dispersion on CNTs in the matrix i.e. high surface energy of CNTs leads them to form agglomerates. These compact agglomerates lead to inhomogeneous dispersion and stress con-

Table 4. Summary of mechanical properties of neat PA 6 and its nanocomposite containing PCNTs and CCNTs

Samples	Tensile modulus [MPa]	Tensile strength [MPa]	Elongation at break [%]
PA 6	1557±106	75±1	28.5±12.1
CCNT-0.1%	1540±161	63±7	5.7±2.6
CCNT-0.2%	1599±139	69±5	9.2±5.5
CCNT-0.5%	1496±169	67±8	6.4±3.4
CCNT-1%	1669±111	64±14	5.8±5.3
CCNT-2%	1675±48	65±15	4.1±1.4
CCNT-3%	1670±45	54±10	2.8±0.4
PCNT-0.1%	1650±8	73.0±0.2	20.0±7.1
PCNT-0.2%	1638±110	71±3	13.9±7.6
PCNT-0.5%	1390±36	66±3	4.3±0.4
PCNT-1%	1603±131	61±20	3.8±1.5
PCNT-2%	1556±128	66±6	3.5±0.4
PCNT-3%	1642±22	58±1	3.0±0.0

centration sites in the polymer matrix [32]. In addition, lack of any chemical or hydrogen bonding between CNTs and matrix could be another possible reason. As it is known, CNTs without modification have smooth surface and the absence of functional groups (such as OH, COOH and NH) on their surface will have poor interaction with the polymer matrix [33]. It seems that the presence of polarity such as CONH group in PA6 alone is still not capable of forming good CNT-PA6 interactions. This may explain the inferior strength of the PA6/CNT nanocomposites as observed in this study. As has been reported in different studies, in order to increase interaction between CNTs and polymers, chemical functionalization of CNTs is performed [34–36]. On the other hand, one of the interesting properties of CNTs is their electrical properties. These will be the outline of our future publications. Tensile modulus has a small increase due to the addition of CNTs to the polymer matrix. This increase was about 6 and 8% for PA6/PCNTs-0.1% and PA6/CCNTs-2%, respectively.

4. Conclusions

In this work, we have prepared bulk MWCNTs based on bimetallic Co-Mo/MgO catalyst in a rotary tubular reactor. As-produced CNTs characterized by using TEM, TGA and Raman spectroscopy. Their thermal stability was better than commercial ones but they are not fully graphitized according to Raman spectrum (I_D/I_G = 1.54) and TEM image. Then we introduced PCNTs and CCNTs in PA6 via melt mixing method. DSC results showed that the crystallization temperature shifted to a higher temperature by incorporating both types of CNTs. CNTs act as nucleating agent and their thermal conductivity affect this operation. More than 30% increase in crystallinity detected for PA6/PCNTs nanocomposites. XRD patterns of nanocomposites showed that crystalline structure of PA6 has changed from α/γ phase to more thermodynamically stable α-form. Melting point of nanocomposites showed narrower range due to high thermal conductivity of CNTs. Thermal degradation behaviour of all nanocomposites was the same as neat PA6. Decomposition temperature at 5 wt% under N_2 atmosphere enhanced by increasing CNTs loading. PCNTs had more impact on changing the thermal and crystalline properties of PA6 compared to CCNTs due to higher metal contents since this metal can facilitate heat conduction and therefore could help mobility or the decomposition of polymer chains. Tensile tests showed unmodified non-polar CNTs do not have any affinity and interfacial interaction with polar polyamide chains and hence, no significant improvement observed in mechanical properties.

Acknowledgements

The authors wish to acknowledge the financial support provided by Malaysian Technology Development Corporation (MTDC) (project no. 6053013) and RU grant (No. 814004).

References

[1] Iijima S.: Helical microtubules of graphitic carbon. Nature, **354**, 56–58 (1991).
DOI: 10.1038/354056a0

[2] Zhao C., Hu G., Justice R., Schaefer D. W., Zhang S., Yang M., Han C.: Synthesis and characterization of multi-walled carbon nanotubes reinforced polyamide 6 via *in situ* polymerization. Polymer, **46**, 5125–5132 (2005).
DOI: 10.1016/j.polymer.2005.04.065

[3] Chen E-C., Wu T-M.: Isothermal and nonisothermal crystallization kinetics of nylon 6/functionalized multi-walled carbon nanotube composites. Journal of Polymer Science Part B: Polymer Physics, **46**, 158–169 (2008).
DOI: 10.1002/Polb.21351

[4] Liu T., Phang I. Y., Shen L., Chow S. Y., Zhang W-D.: Morphology and mechanical properties of multiwalled carbon nanotubes reinforced nylon-6 composites. Macromolecules, **37**, 7214–7222 (2004).
DOI: 10.1021/Ma049132t

[5] Pavlidou S., Papaspyrides C.: A review on polymer–layered silicate nanocomposites. Progress in Polymer Science, **33**, 1119–1198 (2008).
DOI: 10.1016/j.progpolymsci.2008.07.008

[6] De Zhang W., Shen L., Phang I. Y., Liu T.: Carbon nanotubes reinforced nylon-6 composite prepared by simple melt-compounding. Macromolecules, **37**, 256–259 (2004).
DOI: 10.1021/Ma035594f

[7] Xia H., Wang Q., Qiu G.: Polymer-encapsulated carbon nanotubes prepared through ultrasonically initiated *in situ* emulsion polymerization. Chemistry of Materials, **15**, 3879–3886 (2003).
DOI: 10.1021/Cm0341890

[8] Gao J., Itkis M. E., Yu A., Bekyarova E., Zhao B., Haddon R. C.: Continuous spinning of a single-walled carbon nanotube–nylon composite fiber. Journal of the American Chemical Society, **127**, 3847–3854 (2005).
DOI: 10.1021/Ja0446193

[9] Zhang R. H., Yang Y. K., Xie X. L., Li R. K. Y.: Dispersion and crystallization studies of hyper-branched poly(urea-urethane)s-grafted carbon nanotubes filled polyamide-6 nanocomposites. Composites Part A: Applied Science and Manufacturing, **41**, 670–677 (2010).
DOI: 10.1016/j.compositesa.2010.01.017

[10] Rangari V. K., Yousuf M., Jeelani S., Pulikkathara M. X., Khabashesku V. N.: Alignment of carbon nanotubes and reinforcing effects in nylon-6 polymer composite fibers. Nanotechnology, **19**, 245703/1–245703/9 (2008).
DOI: 10.1088/0957-4484/19/24/245703

[11] Pötschke P., Bhattacharyya A. R., Alig I., Dudkin S. M., Leonhardt A., Täschner C., Ritschel M., Roth S., Hornbostel B., Cech J.: Dispersion of carbon nanotubes into thermoplastic polymers using melt mixing. AIP Conference Proceedings, **723**, 478–482 (2004).
DOI: 10.1063/1.1812133

[12] Zhao X., Ye L.: Structure and mechanical properties of polyoxymethylene/multi-walled carbon nanotube composites. Composites Part B: Engineering, **42**, 926–933 (2011).
DOI: 10.1016/j.compositesb.2011.01.002

[13] Brosse A-C., Tencé-Girault S., Piccione P. M., Leibler L.: Effect of multi-walled carbon nanotubes on the lamellae morphology of polyamide-6. Polymer, **49**, 4680–4686 (2008).
DOI: 10.1016/j.polymer.2008.08.003

[14] Phang I. Y., Ma J., Shen L., Liu T., Zhang W-D.: Crystallization and melting behavior of multi-walled carbon nanotube-reinforced nylon-6 composites. Polymer International, **55**, 71–79 (2006).
DOI: 10.1002/Pi.1920

[15] Sun L., Yang J-T., Lin G-Y., Zhong M-Q.: Crystallization and thermal properties of polyamide 6 composites filled with different nanofillers. Materials Letters, **61**, 3963–3966 (2007).
DOI: 10.1016/j.matlet.2006.12.090

[16] Zein S. H. S., Mohamed A. R., Sai P. S. T.: Kinetic studies on catalytic decomposition of methane to hydrogen and carbon over Ni/TiO_2 catalyst. Industrial and Engineering Chemistry Research, **43**, 4864–4870 (2004).
DOI: 10.1021/ie034208f

[17] Chai S-P., Lee K-Y., Ichikawa S., Mohamed A. R.: Synthesis of carbon nanotubes by methane decomposition over Co–Mo/Al_2O_3: Process study and optimization using response surface methodology. Applied Catalysis A: General, **396**, 52–58 (2011).
DOI: 10.1016/j.apcata.2011.01.038

[18] Sivakumar V. M., Abdullah A. Z., Mohamed A. R., Chai S. P.: Optimized parameters for carbon nanotubes synthesis over Fe and Ni catalyst via methane CVD. Reviews on Advanced Materials Science, **27**, 25–30 (2011).

[19] Yeoh W-M., Lee K-Y., Chai S-P., Lee K-T., Mohamed A. R.: Synthesis of high purity multi-walled carbon nanotubes over Co-Mo/MgO catalyst by the catalytic chemical vapor deposition of methane. New Carbon Materials, **24**, 119–123 (2009).
DOI: 10.1016/S1872-5805(08)60041-4

[20] Liu X., Wu Q., Berglund L. A., Qi Z.: Investigation on unusual crystallization behavior in polyamide 6/montmorillonite nanocomposites. Macromolecular Materials and Engineering, **287**, 515–522 (2002).
DOI: 10.1002/1439-2054(20020801)287:8<515::aid-mame515>3.0.co;2-b

[21] Chow W. S., Mohd Ishak Z. A., Karger-Kocsis J., Apostolov A. A., Ishiaku U. S.: Compatibilizing effect of maleated polypropylene on the mechanical properties and morphology of injection molded polyamide 6/polypropylene/organoclay nanocomposites. Polymer, **44**, 7427–7440 (2003).
DOI: 10.1016/j.polymer.2003.09.006

[22] Ha H., Kim S. C., Ha K.: Morphology and properties of polyamide/multi-walled carbon nanotube composites. Macromolecular Research, **18**, 660–667 (2010).
DOI: 10.1007/s13233-010-0702-y

[23] Fornes T. D., Paul D. R.: Crystallization behavior of nylon 6 nanocomposites. Polymer, **44**, 3945–3961 (2003).
DOI: 10.1016/S0032-3861(03)00344-6

[24] Cuentas-Gallegos A. K., Miranda-Hernández M., Vargas-Ocampo A.: Dispersion effect of Cs-PW particles on multiwalled carbon nanotubes and their electrocatalytic activity on the reduction of bromate. Electrochimica Acta, **54**, 4378–4383 (2009).
DOI: 10.1016/j.electacta.2009.03.010

[25] Cuentas-Gallegos A., Jimenez-Penaloza S., Baeza-Rostro D., German-Garcia A.: Influence of the functionalization degree of multiwalled carbon nanotubes on the immobilization of polyoxometalates and its effect on their electrochemical behavior. Journal of New Materials for Electrochemical Systems, **13**, 369–376 (2010).

[26] Sahoo N. G., Cheng H. K. F., Cai J., Li L., Chan S. H., Zhao J., Yu S.: Improvement of mechanical and thermal properties of carbon nanotube composites through nanotube functionalization and processing methods. Materials Chemistry and Physics, **117**, 313–320 (2009). DOI: 10.1016/j.matchemphys.2009.06.007

[27] Zhang F., Zhou L., Xiong Y., Liu G., Xu W.: Isothermal crystallization kinetics of high-flow nylon 6 by differential scanning calorimetry. Journal of Applied Polymer Science, **111**, 2930–2937 (2009). DOI: 10.1002/App.29352

[28] Li J., Fang Z., Zhu Y., Tong L., Gu A., Liu F.: Isothermal crystallization kinetics and melting behavior of multiwalled carbon nanotubes/polyamide-6 composites. Journal of Applied Polymer Science, **105**, 3531–3542 (2007). DOI: 10.1002/App.24606

[29] Liu T., Tjiu W. C., He C., Na S. S., Chung T-S.: A processing-induced clay dispersion and its effect on the structure and properties of polyamide 6. Polymer International, **53**, 392–399 (2004). DOI: 10.1002/pi.1359

[30] Shen Z., Bateman S., Wu D. Y., McMahon P., Dell'Olio M., Gotama J.: The effects of carbon nanotubes on mechanical and thermal properties of woven glass fibre reinforced polyamide-6 nanocomposites. Composites Science and Technology, **69**, 239–244 (2009). DOI: 10.1016/j.compscitech.2008.10.017

[31] Kuan H-C., Ma C-C. M., Chang W-P., Yuen S-M., Wu H-H., Lee T-M.: Synthesis, thermal, mechanical and rheological properties of multiwall carbon nanotube/waterborne polyurethane nanocomposite. Composites Science and Technology, **65**, 1703–1710 (2005). DOI: 10.1016/j.compscitech.2005.02.017

[32] Zhu B-K., Xie S-H., Xu Z-K., Xu Y-Y.: Preparation and properties of the polyimide/multi-walled carbon nanotubes (MWNTs) nanocomposites. Composites Science and Technology, **66**, 548–554 (2006). DOI: 10.1016/j.compscitech.2005.05.038

[33] Zhao F., Huang Y.: Preparation and properties of polyhedral oligomeric silsesquioxane and carbon nanotube grafted carbon fiber hierarchical reinforcing structure. Journal of Materials Chemistry, **21**, 2867–2870 (2011). DOI: 10.1039/C0JM03919E

[34] Li Q., Xue Q., Hao L., Gao X., Zheng Q.: Large dielectric constant of the chemically functionalized carbon nanotube/polymer composites. Composites Science and Technology, **68**, 2290–2296 (2008). DOI: 10.1016/j.compscitech.2008.04.019

[35] Meng H., Sui G. X., Fang P. F., Yang R.: Effects of acid- and diamine-modified MWNTs on the mechanical properties and crystallization behavior of polyamide 6. Polymer, **49**, 610–620 (2008). DOI: 10.1016/j.polymer.2007.12.001

[36] Meng H., Sui G. X., Xie G. Y., Yang R.: Friction and wear behavior of carbon nanotubes reinforced polyamide 6 composites under dry sliding and water lubricated condition. Composites Science and Technology, **69**, 606–611 (2009). DOI: 10.1016/j.compscitech.2008.12.004

eXPRESS Polymer Letters Vol.8, No.3 (2014) 187–196
Available online at www.expresspolymlett.com
DOI: 10.3144/expresspolymlett.2014.22

Adsorption of heavy metal ions and azo dyes by crosslinked nanochelating resins based on poly(methylmethacrylate-co-maleic anhydride)

*A. Masoumi, M. Ghaemy**

Polymer research laboratory, Faculty of Chemistry, University of Mazandaran, Babolsar, Iran

Received 24 August 2013; accepted in revised form 28 October 2013

Abstract. Chelating resins are suitable materials for the removal of heavy metals in water treatments. A copolymer, Poly(MMA-co-MA), was synthesized by radical polymerization of maleic anhydride (MA) and methyl methacrylate (MMA), characterized and transformed into multifunctional nanochelating resin beads (80–150 nm) via hydrolysis, grafting and crosslink reactions. The resin beads were characterized by swelling studies, field emission scanning electron microscopy (FESEM) and Fourier transform infrared spectroscopy (FTIR). The main purpose of this work was to determine the adsorption capacity of the prepared resins (swelling ratio ~55%) towards metal ions such as Hg^{2+}, Cd^{2+}, Cu^{2+} from water at three different pH values (3, 6 and 9). Variations in pH and types of metal ions have not significantly affected the chelation capacity of these resins. The maximum chelation capacity of one of the prepared resin beads (Co-g-AP_3) for Hg^{2+} was 63, 85.8 and 71.14 mg/g at pH 3, 6 and 9, respectively. Approximately 96% of the metal ions could be desorbed from the resin. Adsorption capacity of these resins towards three commercial synthetic azo dyes was also investigated. The maximum adsorption of dye AY42 was 91% for the resin Co-g-AP_3 at room temperature. This insures the applicability of the synthesized resins for industrial applications.

Keywords: *industrial applications, nanochelating crosslinked resin, heavy metal removal, dye removal*

1. Introduction

Industrial and domestic wastewater containing heavy metal ions are increasingly discharged into the environment, especially in developing countries. Unlike some organic pollutants, heavy metals are not biodegradable and cannot be metabolized or decomposed [1]. They are responsible for causing damages to the environment and can also easily enter the food chain through a number of pathways and adversely affecting the health of people [2]. Therefore, reliable methods are needed to detect and remove heavy metals in environmental and biological samples. The traditional methods commonly used for their removal from aqueous solution include ion-exchange [3], solvent extraction [4], chemical precipitation [5], nano-filtration [6, 7], reverse osmosis [8], and adsorption [9–12]. Among these techniques, adsorption is generally preferred due to its high efficiency, low cost possibilities, easy handling, and also the availability of different adsorbents. Nowadays, among the various solid adsorbents, polymeric chelating resins are widely used in the removal of metal ions due to their high adsorption capacities and selectivity [13–17]. Several criteria such as specific and fast complexation of the metal ions as well as the reusability of the adsorbent are important in the design of metal-chelating polymers. Synthetic chemicals including dyes have been extensively used in many industries such as textile, plastic, leather tanning, paper production, food tech-

*Corresponding author, e-mail: ghaemy@umz.ac.ir

nology, etc. They are toxic to some aquatic organisms and are of serious health risk to human beings [18]. Many physical and chemical methods have been used for the treatment of chemical-containing effluents [19–22]. Adsorption methods have been invariably successful to decolorize textile effluents, although this application can be limited by the high cost of adsorbents. This work describes preparation and characterization of nanochelating resin beads for the removal of heavy-metal ions and azo dyes from water. For these reasons, we have focused our attention on the development of new class functionalized adsorbents based on the copolymer poly (MMA-co-MA). To produce efficient metal-complexing ligand, different functional groups such as carboxylate and amine were introduced into the network structure of this copolymer via hydrolysis, grafting and crosslink reactions. Characterization of the chelating resins was carried out by swelling tests, FT-IR, XRD, AFM and SEM. The results of adsorption of Hg^{2+}, Cd^{2+} and Cu^{2+} ions and synthetic azo dyes such as yellow 42 (AY42), red 151 (AR151) and blue 9 (MB9) by these resin beads from water are reported here. Desorption of the metal ions from the pre-adsorbed resins was also examined using HCl solution.

2. Experimental

2.1. Materials

Benzoyl peroxide (BPO), ethylenediamine (ED), diethylenetriamine (DETA), triethylenetetramine (TETA), (MMA), (MA), 2-aminopyridine (AP), triethylamine (TEA) and solvents were purchased from Fluka Co. (Germany). Copper chloride ($CuCl_2 \cdot 2H_2O$), mercury chloride ($HgCl_2$), cadmium chloride ($CdCl_2$), and dyes such as acid yellow 42 (AY42), acid red 151 (AR151) and mordant blue 9 (MB9) were purchased from Aldrich-Sigma Co. (Germany). All the chemicals and reagents were analytical grade and used as received without further purification. pH adjustments were performed with HCl and NaOH solutions.

2.2. Synthesis

(a) Synthesis of Poly(MMA-co-MA) was carried out via free-radical polymerization of (MA) and (MMA) in the presence of benzoyl peroxide (BPO) as an initiator and under argon atmosphere according to the procedure given in literature with slight modification [23]. Briefly, in a 250 mL three-necked round bottom flask equipped with a magnetic stirrer, a condenser and an inlet for inert gas, 2.33 mL (0.020 mol) MMA, 2.0 g (0.020 mol) MA, and 50 mL THF were placed. Then the reaction mixture was degassed for 30 min by argon to remove oxygen from the solution. BPO (1 wt%) was added to the reaction mixture and refluxed under these conditions for 8 h. Finally the copolymer was precipitated by adding the reaction mixture into the nonsolvent of methanol and water (1:2, v:v). The obtained white precipitate was washed thoroughly with water and then dried under vacuum at 80°C (yield = 96%).

(b) The graft copolymer (Co-g-AP) was prepared by mixing a mole ratio of 1:0.5 of poly(MMA-co-MA):AP in 50 mL THF in a 100 mL flask equipped with a magnetic stirrer, a condenser and an inlet for inert gas. Then, 0.5 mL (0.004 mol) TEA was added as a catalyst and the reaction mixture was refluxed with stirring for 4 h. The solid product was formed by adding the reaction mixture into n-hexane. After filtration, the solid product was washed by n-hexane several times and then dried in a vacuum oven at 80°C (yield = 95%).

(c) The hydrolyzed copolymer (Co-Hyd) was prepared by adding 1 g poly(MMA-co-MA) and 15 mL NaOH (2 M) into a 100 mL flask equipped with a magnetic stirrer, a condenser and an inlet for inert gas. The mixture was stirred at room temperature for 7 hours until a clear homogeneous solution was formed. The hydrolyzed product was recovered as precipitate from basic solution by addition of HCl (1 M) solution. The precipitate was separated by filtration, washed several times with distilled water and then dried under vacuum at 80ºC for 12 h.

(d) The crosslinked resin beads (Co-g-AP_1, Co-g-AP_2, Co-g-AP_3) were prepared in THF by the reaction between poly(MMA-co-MA), AP as a grafting agent and a crosslink agent such as ED, DETA or TETA with a mole ratio of 1:0.5:0.25, respectively. 0.5 mL (0.004 mol) TEA was used as a catalyst of the reaction. The mixture was refluxed for 3 h under inert gas with stirring using an ultrasonic water bath. A solid precipitate was formed as the reaction proceeded which

was finally filtered, washed several times with THF, and dried in a vacuum oven at 80°C for 12 h. The yields were in the range of 94–98%.

2.3. Adsorption studies

To investigate the tendency of the chelating resin beads for the removal of heavy metal ions such as Cu^{2+}, Cd^{2+} and Hg^{2+} in aqueous solutions, constant weight of dried adsorbents were used in all batch experiments. Extraction of metal ions was carried out individually by using their chloride salts, $CuCl_2{\cdot}2H_2O$, $CdCl_2$ and $HgCl_2$. All experiments were performed at room temperature by using mixture of 50 mg beads and 50 mL metal ion solution (initial concentration: 100 mg/L) in separate flasks which were stirred magnetically for 24 h. The suspensions were brought to the desired pH (3, 6, 9) by adding NaOH (0.1 M) and HCl (0.1 M). After the adsorption was complete, the mixture was filtered, and the residual metal-ion content in the filtrate was determined by AAS. The amount of metal ion adsorbed into the unit of the chelating resin i.e. the adsorption capacity (Q, in mmol·g^{-1} polymer) was calculated on the basis of Equation (1):

$$Q = \frac{(C_0 - C_A)\cdot V}{W} \tag{1}$$

where C_0 and C_A are the concentration (mmol/L) of metal ion in the initial solution and in the aqueous phase after adsorption, respectively, V is the volume of the aqueous phase (L) and W is the weight of the adsorbent (0.05 g). The efficiency for ions adsorption from the solution (R [%]) was calculated using Equation (2):

$$R = \frac{C_0 - C_A}{C_0}\cdot 100 \tag{2}$$

2.4. Desorption behavior

For the desorption experiment, the chelating resin beads which had been adsorbed with the metal ions according to the procedure set-forth in the above section was used. The desorption of metal ions was carried out in 25 mL of 0.2 M HCl solution [24], while the mixture was stirred at room temperature for 1 h. After filtration, the metal ion concentration in the aqueous phase was measured by AAS. The desorption ratio (D [%]) was calculated by using Equation (3):

$$D[\,\%\,] = \frac{A}{B}\cdot 100 \tag{3}$$

where A is the amount of metal ions desorbed to the elution medium [mg] and B is the amount of metal ions adsorbed on the resin [mg].

2.5. Dyes removal

To investigate the tendency of the chelating resin beads for the removal of dyes in aqueous solutions, constant weight of dried adsorbents were used in all batch experiments. The chemical structures of the azo dyes are shown in Figure 1. 0.05 g of the resin beads (Co-g-AP_3, MMA-Co-MA, and Co-Hyd) and 10 mL aqueous solution of a dye such as AY42, AR151and MB9 (initial concentration, 100 mg/L) were shaken in a shaker at room temperature for 12 h without pH adjustment. The concentration of dye in the filtrate was determined by measuring the maximum absorption intensity of each dye at the corresponding wavelength using a UV-vis spectrophotometer (λ_{max} = 408 nm for AY42, λ_{max} = 500 nm for AR151 and λ_{max} =533 nm for MB9) and the following Beer-Lambert law (Equation (4)):

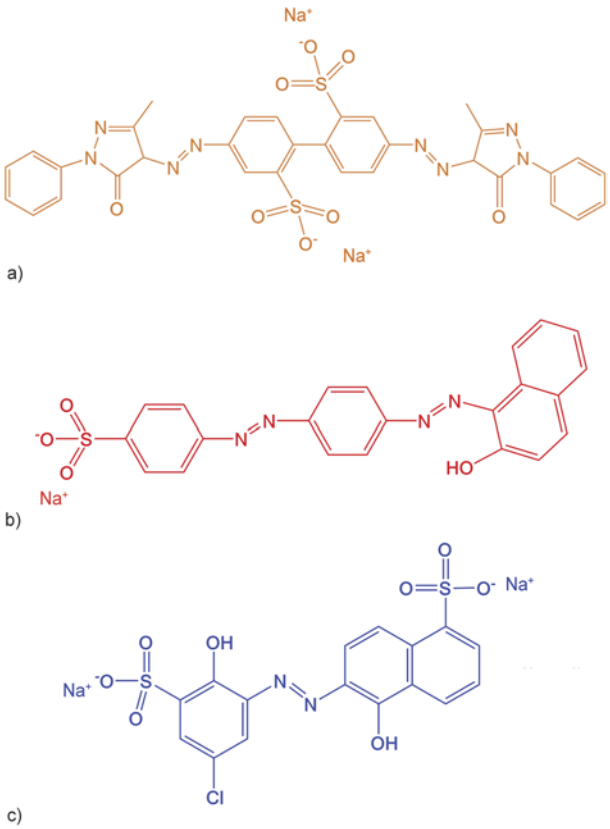

Figure 1. Chemical structural of the tested dyes; AY42 (a), AR151 (b) and MB9 (c)

$$A_0 - A = \varepsilon b(C_0 - C) \quad (4)$$

where A is the absorption of dye at a given wavelength, ε is molar absorptivity, unique to each molecule and varying with wavelength, b is the path length through the solution that the light has to travel (1 cm), and C_0 (100 mg/L) and C is the concentration of dye in the solution before and after adsorption, respectively. The sorption percentage of the chelating resin was calculated using Equation (5):

$$R[\%] = \frac{W}{W_0} \cdot 100 \quad (5)$$

where W is the amount of adsorbed dye and W_0 the initial amount of dye.

2.6. Measurements

FT-IR analysis was carried out on a Bruker Tensor 27 spectrometer (Bruker, Karlsruhe, Germany). X-ray diffraction (XRD) patterns were obtained on a RigakuD/Max-2550 powder diffractometer with a scanning speed of 5°·min^{-1} in the 2θ range of 10–70°. The surface morphology of the beads was examined by using field emission scanning electron microscopy (FESEM) (Model: Hitachi S4160). A fragment of the dried bead was mounted on a FESEM sample mount and was sputter coated with gold for 2 min, and then was mounted in FESEM and scanned at the desired magnification. A PHS-3C pH-meter (Shanghai, Tianyou) was used for pH measurements. The concentration of metal ions in the solution was measured by use of a flame atomic absorption spectrophotometer (AAS) (Hewlett-Packard 3510). Atomic force microscopy (AFM, Easy Scan 2 Flex AFM, Swiss Co.) was also used to investigate the surface phase and topography of the resin beads before and after the sorption process. The concentration of dye in the filtrate was measured using a UV-visible spectrophotometer. The gel permeation chromatography (GPC) measurements were conducted at 30°C with a Perkin-Elmer instrument equipped with a differential refractometer detector. The columns used were packed with a polystyrene/divinylbenzene copolymer (PL gel MIXED-B from Polymer Laboratories) and THF was used as fluent at a flow rate of 1 mL/min. Calibration of the instrument was performed with monodisperse polystyrene standards. Water absorption measurements of the chelating resins were determined gravimetrically in distilled water at room temperature. Briefly, 0.2 g dry resin beads (Co-g-AP, Co-g-AP$_1$, Co-g-AP$_2$, Co-g-AP$_3$, and Co–Hyd) were placed in separate 50 mL vials containing distilled water for 3 days. The beads were taken out from the water at different times, wiped using a filter paper, and weighed. The weight difference before and after immersion was determined and used for calculation of the swelling ratio.

3. Results and discussion

3.1. Characterization and properties of the chelating resins

The FT-IR spectrum of poly(MMA-co-MA), Figure 2a, showed characteristic absorption bands of anhydride at 1747, 1809 and 1856 cm^{-1} and of ester group in the MMA repeating unit at 1724 cm^{-1}. The number and weight average molar masses (M_n and M_w) of this copolymer were determined by GPC were 5.096·10^3 and 9.34·10^3 g/mol, respectively, with distribution index of 1.83. Earlier studies have indicated that carboxylic acid and amide functional groups in polymer backbone provide more adsorption sites for heavy metal ions in wastewater. In order to obtain chelating resins as adsorbents of heavy metals with satisfactory adsorption capacity, following transformations were performed: (1) poly (MMA-co-MA) was hydrolyzed with NaOH (2 M) to form carboxylate ions which then neutralized by HCl to form –COOH groups along the copolymer chains, (2) poly(MMA-co-MA) was reacted with

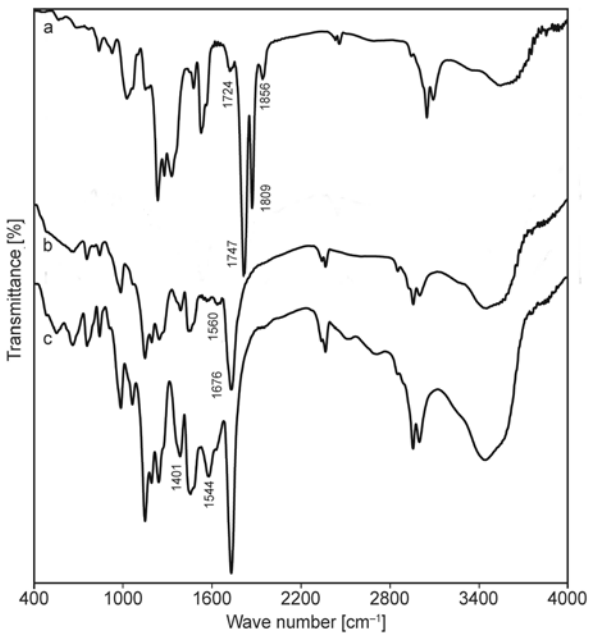

Figure 2. Representative FT-IR spectra of poly(MMA-co-MA) (a), Co-g-AP$_3$ (b) and metal-resin complex {Hg–(Co–g-AP$_3$)} (c)

AP to form an alkylamide linkage and a carboxylic acid group, and (3) poly(MMA-co-MA) was reacted with AP and a crosslink agent such as ED, DETA, and TETA to form a network structure with many adsorption sites for metal ions. Comparison of the FT-IR spectra of poly(MMA-co-MA) and Co-g-AP_3, as shown in Figure 2a and 2b, indicates that characteristic bands of the anhydride linkage in poly(MMA-co-MA) at 1747, 1809 and 1856 cm^{-1} disappeared after reaction with TETA and the formed amide linkage (–CO–NH–) showed absorption band at ~1676 cm^{-1}. To investigate the effect of chemical reactions in the copolymer matrix, the phase morphology was studied using SEM. Figure 3a–3c shows representative SEM images of Co-g-AP, Co-g-AP_3 and Co-Hyd. As can be seen in these figures, the roughness of the surface and particularly the porous surface after hydrolysis, Figure 3c, should be considered as a factor providing chelating ability for the resins. On that basis, the adsorbents present an adequate morphology with disordered distribution of sizes which can be the main reason of their high surface ability for the removal of metal ions. To observe morphological properties such as surface porosity, texture and roughness, micrographs of the surface and cross section of Co-g-AP_3 before and after metal ion adsorption were registered by using AFM. Figure 3d shows smoother surface of Co-g-AP_3 before metal ion adsorption while Figure 3e reveals a predominantly hill-valley-structured surface with irregular pores of nanoscale topography after metal ion adsorption. The roughness can also be seen in 3D images of the surface of metal ion adsorbed sample with their histograms show size distribu-

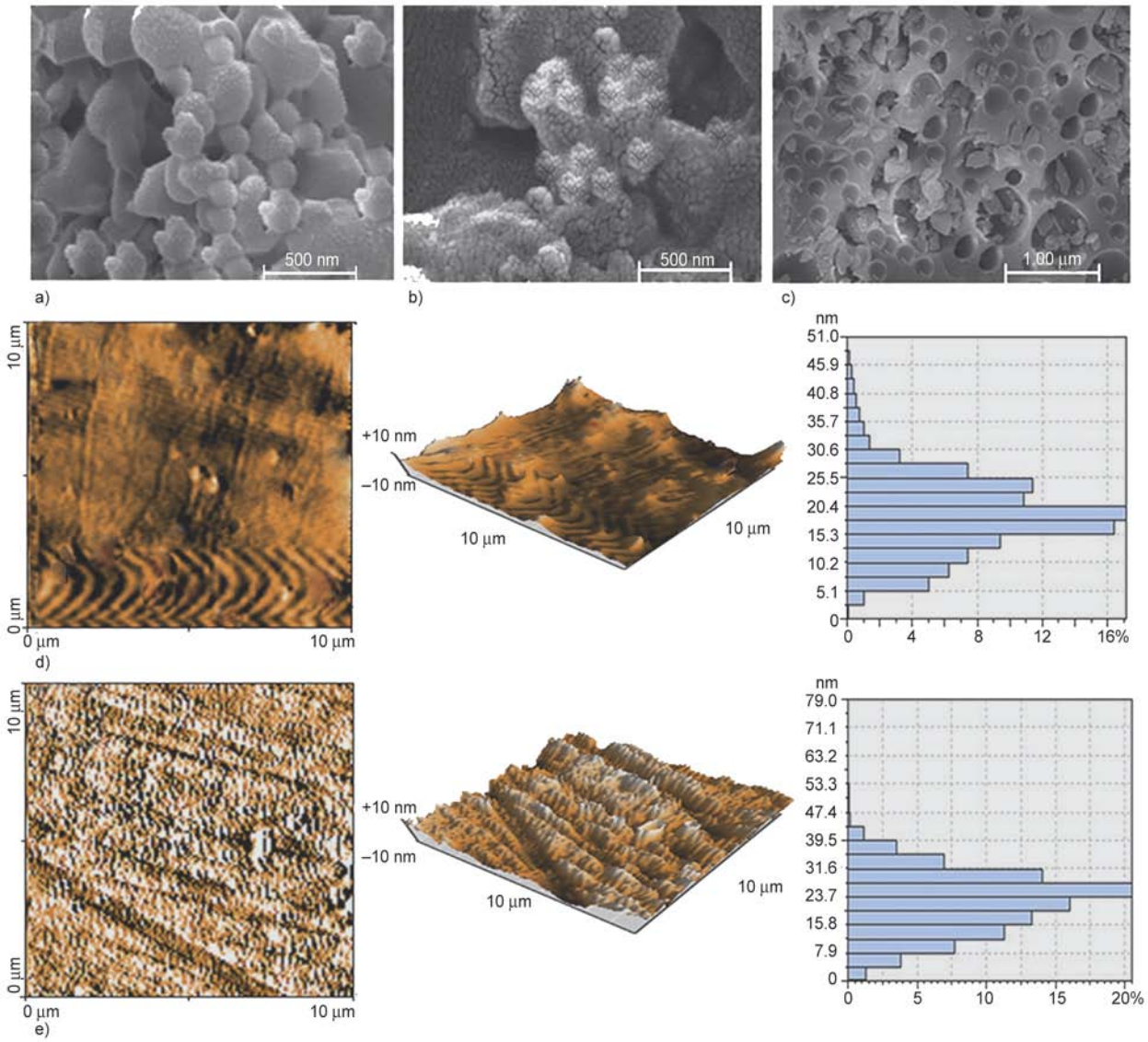

Figure 3. Representative FESEM images of Co-g-AP (a), Co-g-AP_3 (b) and Co–Hyd (c). AFM images of Co-g-AP_3, before (d) and after (e) Hg^{2+} ion adsorption

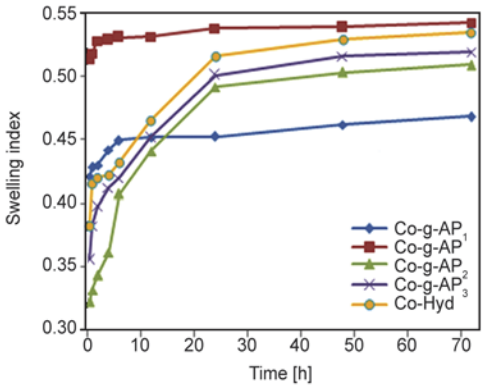

Figure 4. Water uptake of the chelating resins

tions. The average size for the particles of Co-g-AP_3 before adsorption is in the range of 15–17 nm and after metal ion adsorption is in the range of 20–28 nm, respectively. The crosslinked beads are hydrophilic matrices, i.e., hydrogels; therefore they do not dissolve in aqueous media, but do swell, depending on the degree of crosslinking and on the hydrophilicity of the matrix. The equilibrium swelling ratio of the resin beads are shown in Figure 4. Several possible factors are contributing in water absorption of the beads such as incorporation of hydrophilic amino and amide groups into the polymer matrix which increases water absorption and introduction of hydrophobic $–CH_2–$ units into the polymer structure via crosslink agent such as TETA which reduces water uptake of the resin. As can be seen in Figure 4, the copolymers Co-g-AP and Co-Hyd showed the highest water absorption. These two copolymers are not crosslinked and they are open systems with highly hydrophilic groups of carboxylic acids. The water absorption of three crosslinked copolymers showed order of Co-g-AP_3 >Co-g-AP_2>CO-g-AP_1 which depended on the chemical structure of the curing agent (ED, DETA and TETA, respectively) and the network structure. The XRD patterns of all copolymers showed only a broad diffraction hump at about 2θ = 15–20 indicating the amorphous nature of the prepared resin beads.

3.2. Adsorption of heavy metal ions

In this research, the FT-IR spectroscopy was used to monitor the structural changes take place in the chelating resins as a result of metal-ion complexation. Therefore, the first information about the structural changes such as shift or elimination of a certain band present in the starting resin as well as the appearance of new bands, caused by the complexation of the resin with metal ions, was provided by the FT-IR spectra. The bonding mode of Hg^{2+} to chelating resin was examined by comparing the FT-IR spectra of poly(MMA–co–MA) and Co-g-AP_3 with the spectrum of [Hg–(Co-g-AP_3)] complex. As shown in Figure 2c, the FT-IR spectrum of Hg-(Co-g-AP_3) is quite different from the spectrum of poly (MMA-co-MA) in Figure 2a. Two strong absorption bands at 1401 and 1544 cm^{-1} are observed in the spectrum of [Hg–(Co-g-AP_3)] complex, which are assigned to the symmetric (vs, $COO^–$) and asymmetric (vas, $COO^–$) vibration absorption of the carboxylic groups, respectively [25]. The shift of FT-IR peak for the carbonyl group of carboxylate could indicate whether the bonding between the ligand and metal ion was covalent or ionic [26]. In this study, there is small shift towards higher frequency which can be taken as evidence for formation of covalent bond between metal ions and carbonyl groups. The absorption bands characteristic of the aromatic AP in the resin matrix are observed at 1032, 914, 767, and 703 cm^{-1} which were not influenced by the metal complexation. The adsorption capacity of the chelating resin beads for the tested metal ions of Cu^{2+}, Cd^{2+} and Hg^{2+} at pH 3, 6 and 9 are shown in Figure 5. The results demonstrated a relatively weak dependency of metal ions sorption on the pH variations. A relatively high adsorption of about 60–80% was observed at various pH values for the tested metal ions by all the chelating resin beads. Adsorbents with carboxyl, sulfonic, and phosphonic groups on the surface, remove adsorbates through ion exchange, while those containing nitrogen such as amine, hydrazine, thioamide, and imidazoline groups, not only chelate cationic metal ions, but also adsorb anionic adsorbates through electrostatic interactions [27–29]. All the prepared resins have carboxylic acid and amine groups as potential ion exchange/complexing units. In the acidic conditions, the degree of protonation of amine groups affects their ability to bind metal ions. Therefore, the relatively high adsorption of metal ions in acidic conditions could be explained by the complex formation between M^{+2} and –COOH groups. The –COOH groups are formed as a result of reaction between anhydride of the copolymer and amine of the crosslink agent, and also can be due to hydrolysis of the ester linkage in the MMA repeating unit. As can be seen in Figure 5, the dependency of adsorption capacity of these resins on the pH value is related to the functional groups of adsorbent and

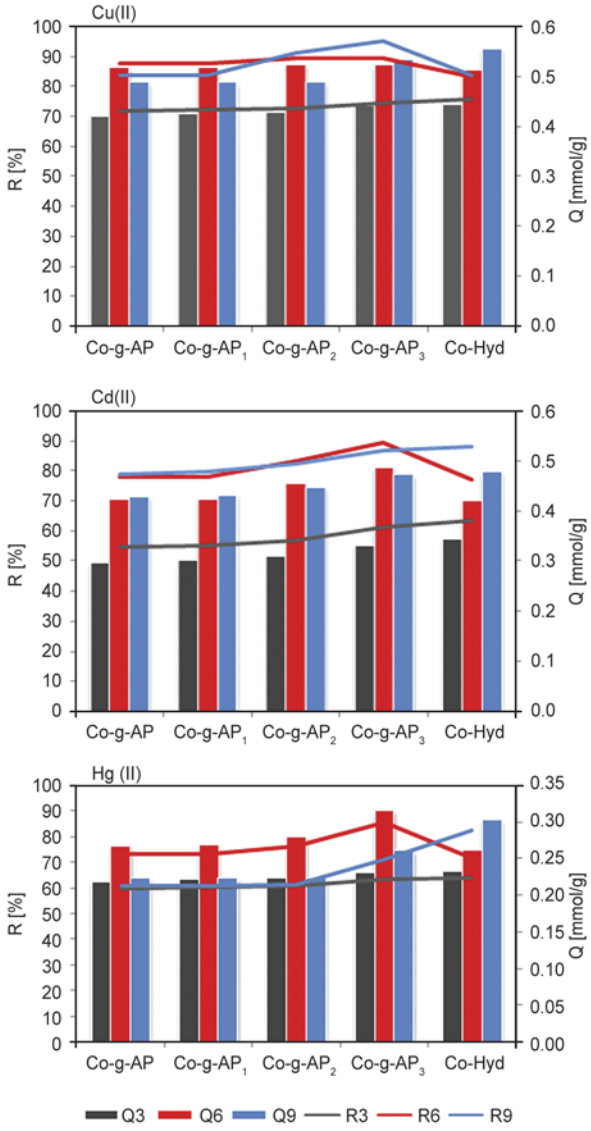

Figure 5. Effect of the initial pH of the testing solutions on the adsorption capacity (Q) and percentage (R [%]) for the tested metal ions. Initial ion concentration = 100 mg/L, sample dose = 5 mg/50 mL, temperature = 25°C, and contact time = 24 h.

type of metal ion. For example, all the chelating resins adsorbed about 55% (Q = 0.31 mmol/g) Cd^{2+} at pH 3 which increased to over 81% (Q = 0.46 mmol/g) at pH 9, while adsorption of Cu^{2+} was 73% (Q = 0.42 mmol/g) and 87% (Q = 0.51 mmol/g), respectively, at same pH values. Therefore, in general, a high affinity was observed for adsorption of the tested metal ions by all the prepared resins especially by Co-Hyd and Co-g-AP_3 at various pH. This can be due to presence of different metal ion adsorption sites such as carboxylate and amine groups in the copolymer matrix. The order of adsorption percentage changed as follows: Co-g-AP_3≥Co-Hyd> Co-g-AP_2>Co-g-AP_1>Co-g-AP. The order of these

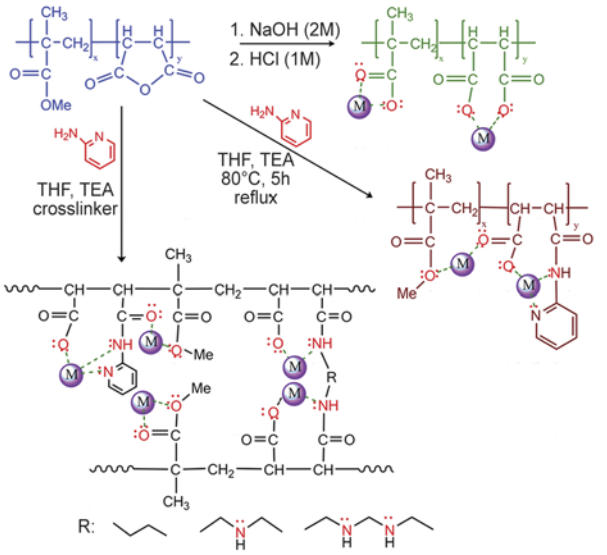

Figure 6. Illustration of metal–chelating resin complexes of Co-Hyd, Co-g-AP and the crosslinked chelating resin

three kinds of metal ion chelation on mass basis for the single component metal is Cu^{2+}>Cd^{2+}>Hg^{2+}. This affinity trend is presented on the mass basis [mg] metal chelation per gram resin beads and these units are important in quantifying respective metal capacities in real terms. Incorporation of TETA as crosslinking agent, with long alkyl chain and four amine groups, into the resin structure has significantly increased the adsorption capacity of the network. The results show that the adsorption capacity with Hg^{2+} (at pH = 6) is 71.4 mg/g for Co-Hyd, 72.63 mg/g for Co-g-AP, 73 mg/g for Co-g-AP_1, 76.3 mg/g for Co-g-AP_2 and 85.8 mg/g for Co-g-AP_3. Figure 6 illustrates the metal ions binding onto the chelating resins. Adsorbents used in heavy metal ions removal are in particulate form in most of the cases. In the literature, different affinity sorbents with a wide range of adsorption capacities for heavy metal ions have been reported. Shreedhara-Murthy and Ryan found 5–27 mg/g Cu(II) removal by cellulose dithiocarbamate resins [30]. Roozemond showed 32 mg/g Cu(II) with pyrazole-containing poly(styrene-divinyl-benzene) sorbents [31]. Say *et al.* [32] achieved 714.1, 468.8 and 639.4 mg/g adsorption capacities for Pb(II), Cr(III) and Cd(II), respectively, with poly(HEMA-MAH) beads. Kara *et al.* [33] have prepared poly(EGDMA-VIM) beads and found the chelation capacities of these beads were 69.4 and 114.8 mg/g for Cd(II) and Pb(II), respectively. Duran *et al.* [34] have prepared [poly (VP-PEGMA-EGDMA)] beads and found the chela-

tion capacities of these beads were 18.23, 16.50, 15.81 and 18.25 mg/g for Pb(II), Cd(II), Cr(III), and Cu(II), respectively.

3.3. Desorption of metal ions from the chelating resin

The repeated use of the resins is an essential parameter in improving process economics. Desorption of metal ions from resin–metal ion complexes was carried out by HCl (0.2 M) treatment at room temperature and the amount of metal ions desorbed in 1 hour was measured. As shown in Figure 7, more than 96% of adsorbed metal ions are recovered in the acid leaching process indicating that chelation (i.e., binding of heavy metal ions with functional groups in resin) is completely reversible. In order to obtain the reusability of the resins, chelation–elution cycle was repeated successfully five times by using the same adsorbent and the results are shown in Figure 7.

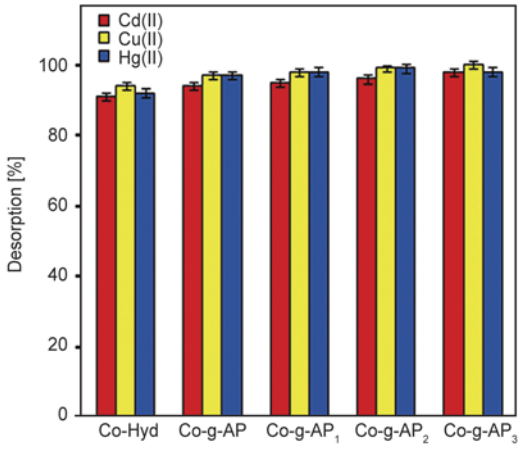

Figure 7. Desorption of Hg^{2+} ion from the chelating resins beads that had been preadsorbed, under conditions given in Figure 6, as a function of submersion time in 25 mL of HCl (0.2 M) solution for 1 h at 25°C

3.4. Dyes removal

The adsorption of dyes with the prepared chelating resin beads was carried out by using three commercial azo dyes containing different functional groups such as –N=N–, chlorine, oxadiazine and sulfate (Figure 1). The results for the dyes adsorption are shown in Figure 8. The order for the dyes removal by the resins is: Co-g-AP_3>Co-Hyd> poly(MMA-co-MA), indicating higher capacity for the crosslinked resin in comparison with the results obtained

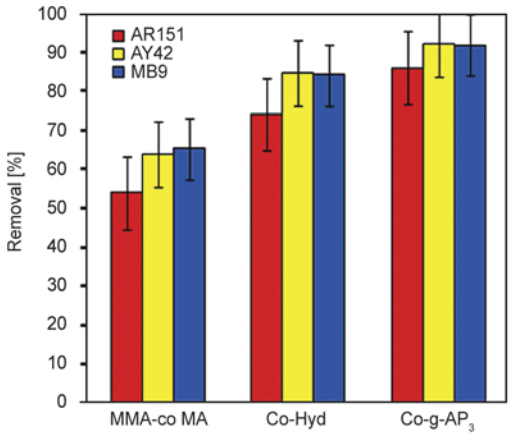

Figure 8. Dyes removal efficiency by the prepared resin beads; (0.05 g of the chelating resin in 10 mL aqueous solution containing a dye with initial concentration = 100 mg/L, at 25°C for 12 h without pH adjustment)

for the unmodified copolymer. This can be due to presence of network structure with different functional groups in the modified resin (Co-g-AP_3), which can accommodate large molecules and interact with the functional groups present in the dye molecules. Also, the relatively high adsorption percentage of Co-Hyd resin can be due to highly pores structure of this resin, as shown in Figure 3c.

4. Conclusions

Adsorption represents a potentially cost-effective way of eliminating toxic heavy metals from industrial wastewaters. Reusable polymer-based adsorbents have been recognized as a promising class of low-cost adsorbents for the removal of heavy-metal ions from aqueous waste streams. In this study, the reaction of AP and different crosslink agents with poly(MMA-co-MA) led to the synthesis of significantly capable chelating resins for the removal of heavy metal ions such as Cu^{2+}, Cd^{2+} and Hg^{2+} from aqueous solution. These results suggest that the prepared chelating resin beads are good heavy metal ions adsorbents in various pH values and can have great potential applications in environmental protection. The affinity order of metal ions on a molar basis is as: Cu^{2+}>Cd^{2+}>Hg^{2+}. The new adsorbents have higher adsorption properties than other adsorbents reported by some researchers. In addition, the capacity of dyes removal of the resin beads was investigated and the results showed that the adsorbed dye increased by using crosslinked resin.

References

[1] Matsuto T., Jung C. H., Tanaka N.: Material and heavy metal balance in a recycling facility for home electrical appliances. Waste Management, **24**, 425–436 (2004). DOI: 10.1016/j.wasman.2003.12.002

[2] Srivastava N. K., Majumder C. B.: Novel biofiltration methods for the treatment of heavy metals from industrial wastewater. Journal of Hazardous Materials, **151**, 1–8 (2008). DOI: 10.1016/j.jhazmat.2007.09.101

[3] Vaaramaa K., Lehto J.: Removal of metals and anions from drinking water by ion exchange. Desalination, **155**, 157–170 (2003). DOI: 10.1016/S0011-9164(03)00293-5

[4] Černá M.: Use of solvent extraction for the removal of heavy metals from liquid wastes. Environmental Monitoring and Assessment, **34**, 151–162 (1995). DOI: 10.1007/BF00546029

[5] Hu X., Li Y., Wang Y., Li X., Li H., Liu X., Zhang P.: Adsorption kinetics, thermodynamics and isotherm of thiacalix[4]arene-loaded resin to heavy metal ions. Desalination, **259**, 76–83 (2010). DOI: 10.1016/j.desal.2010.04.032

[6] Al-Rashdi B. A. M., Johnson D. J., Hilal N.: Removal of heavy metal ions by nanofiltration. Desalination, **315**, 2–17 (2013). DOI: 10.1016/j.desal.2012.05.022

[7] Ozaki H., Sharma K., Saktaywin W.: Performance of an ultra-low-pressure reverse osmosis membrane (ULPROM) for separating heavy metal: effects of interference parameters. Desalination, **144**, 287–294 (2002). DOI: 10.1016/S0011-9164(02)00329-6

[8] Petersková M., Valderrama C., Gibert O., Cortina J. L.: Extraction of valuable metal ions (Cs, Rb, Li, U) from reverse osmosis concentrate using selective sorbents. Desalination, **286**, 316–323 (2012). DOI: 10.1016/j.desal.2011.11.042

[9] Soleimani Lashkenari M., Davodi B., Ghorbani M., Eisazadeh H.: Use of core-shell polyaniline/polystyrene nanocomposite for removal of Cr(VI). High Performance Polymers, **24**, 345–355 (2012). DOI: 10.1177/0954008311436222

[10] Li L., Li Y., Luo X., Deng J., Yang W.: Helical poly(*N*-propargylamide)s with functional catechol groups: Synthesis and adsorption of metal ions in aqueous solution. Reactive and Functional Polymers, **70**, 938–943 (2010). DOI: 10.1016/j.reactfunctpolym.2010.09.006

[11] Jitjaicham S., Kampalanonwat P., Supaphol P.: Metal adsorption behavior of 2,4-dinitrophenyl hydrazine modified polyacrylonitrile nanofibers. Express Polymer Letters, **7**, 832–841 (2013). DOI: 10.3144/expresspolymlett.2013.80

[12] Coşkun R., Soykan C., Saçak M.: Removal of some heavy metal ions from aqueous solution by adsorption using poly(ethylene terephthalate)-g-itaconic acid/acrylamide fiber. Reactive and Functional Polymers, **66**, 599–608 (2006). DOI: 10.1016/j.reactfunctpolym.2005.10.012

[13] Sankar R., Sasidaran M., Kaliyappan T.: Synthesis, characterization, thermal and chelation properties of new polymeric hydrazone based on 2,4-dihydroxy benzaldehyde. High Performance Polymers, **23**, 32–39 (2011). DOI: 10.1177/0954008310381148

[14] Sasidaran M., Sankar R., Kandasamy P., Vijayalakshmi S., Kaliyappan T.: Chelating and biological properties of an azo polymer resin: Synthesis, characterization and its application. High Performance Polymers, **23**, 602–609 (2011). DOI: 10.1177/0954008311428531

[15] Dinu M. V., Dragan E. S.: Heavy metals adsorption on some iminodiacetate chelating resins as a function of the adsorption parameters. Reactive and Functional Polymers, **68**, 1346–1354 (2008). DOI: 10.1016/j.reactfunctpolym.2008.06.011

[16] Vasconcelos H. L., Fávere V. T., Gonçalves N. S., Laranjeira M. C. M.: Chitosan modified with Reactive Blue 2 dye on adsorption equilibrium of Cu(II) and Ni(II) ions. Reactive and Functional Polymers, **67**, 1052–1060 (2007). DOI: 10.1016/j.reactfunctpolym.2007.06.009

[17] Takagi K., Miwa S., Yuki Y.: Synthesis of poly(triazinylstyrene) containing nitrogen-based ligand and function as metal ion adsorbent and oxidation catalyst. Reactive and Functional Polymers, **66**, 1718–1724 (2006). DOI: 10.1016/j.reactfunctpolym.2006.07.005

[18] Ahamed M. E. H., Mbianda X. Y., Mulaba-Bafubiandi A. F., Marjanovic L.: Ion imprinted polymers for the selective extraction of silver(I) ions in aqueous media: Kinetic modeling and isotherm studies. Reactive and Functional Polymers, **73**, 474–483 (2013). DOI: 10.1016/j.reactfunctpolym.2012.11.011

[19] Wang C-C., Wang C-C.: Adsorption characteristics of metal complexes by chelated copolymers with amino group. Reactive and Functional Polymers, **66**, 343–356 (2006). DOI: 10.1016/j.reactfunctpolym.2005.08.011

[20] Vasconcelos H. L., Camargo T. P., Gonçalves N. S., Neves A., Laranjeira M. C. M., Fávere V. T.: Chitosan crosslinked with a metal complexing agent: Synthesis, characterization and copper(II) ions adsorption. Reactive and Functional Polymers, **68**, 572–579 (2008). DOI: 10.1016/j.reactfunctpolym.2007.10.024

[21] Huang J., Zhang K.: The high flux poly (m-phenylene isophthalamide) nanofiltration membrane for dye purification and desalination. Desalination, **282**, 19–26 (2011). DOI: 10.1016/j.desal.2011.09.045

[22] Teng M-Y., Lin S-H.: Removal of methyl orange dye from water onto raw and acidactivated montmorillonite in fixed beds. Desalination, **201**, 71–81 (2006). DOI: 10.1016/j.desal.2006.03.521

[23] Yan B., Wang Q.: Covalently bonded assembly and photoluminescent properties of rare earth/silica/poly (methyl methacrylate-*co*-maleic anhydride) hybrid materials. Journal of Photochemistry and Photobiology A: Chemistry, **197**, 213–219 (2008). DOI: 10.1016/j.jphotochem.2007.12.025

[24] El-Hag Ali A., Shawky H. A., Abd El Rehim H. A., Hegazy E. A.: Synthesis and characterization of PVP/AAc copolymer hydrogel and its applications in the removal of heavy metals from aqueous solution. European Polymer Journal, **39**, 2337–2344 (2003). DOI: 10.1016/S0014-3057(03)00150-2

[25] Albunia A. R., Rizzo P., Guerra G., Torres F. J., Civalleri B., Zicovich-Wilson C. M.: Uniplanar orientations as a tool to assign vibrational modes of polymer chain. Macromolecules, **40**, 3895–3897 (2007). DOI: 10.1021/ma070380+

[26] Wang C-C., Chang C-Y., Chen C-Y.: Study on metal ion adsorption of bifunctional chelating/ion-exchange resins. Macromolecular Chemistry and Physics, **202**, 882–890 (2001). DOI: 10.1002/1521-3935(20010301)202:6<882::AID-MACP882>3.0.CO;2-K

[27] Dinu M. V., Dragan E. S.: Evaluation of Cu^{2+}, Co^{2+} and Ni^{2+} ions removal from aqueous solution using a novel chitosan/clinoptilolite composite: Kinetics and isotherms. Chemical Engineering Journal, **160**, 157–163 (2010). DOI: 10.1016/j.cej.2010.03.029

[28] Murugesan A., Ravikumar L., SathyaSelvaBala V., SenthilKumar P., Vidhyadevi T., Dinesh Kirupha S., Kalaivani S. S., Krithiga S., Sivanesan S.: Removal of Pb(II), Cu(II) and Cd(II) ions from aqueous solution using polyazomethineamides: Equilibrium and kinetic approach. Desalination, **271**, 199–208 (2011). DOI: 10.1016/j.desal.2010.12.029

[29] Chaisuwan T., Komalwanich T., Luangsukrerk S., Wongkasemjit S.: Removal of heavy metals from model wastewater by using polybenzoxazine aerogel. Desalination, **256**, 108–114 (2010). DOI: 10.1016/j.desal.2010.02.005

[30] Shreedhara-Murthy R. S., Ryan D. E.: Preconcentration of copper, cadmium, mercury and lead from sea and tap water samples on a dithiocarbamatecellulose derivative. Analytica Chimica Acta, **140**, 163–169 (1982). DOI: 10.1016/S0003-2670(01)95461-3

[31] Roozemond D. A., den Hond F., Veldhuis J. B. J., Strasdeit H., Driessen W. L.: Preferred uptake of Cu(II) and Cd(II) by novel pyrazole-functionalized chelating polymers. European Polymer Journal, **24**, 867–872 (1988). DOI: 10.1016/0014-3057(88)90161-9

[32] Say R., Garipcan B., Emir S., Patır S., Denizli A.: Preparation and characterization of the newly synthesized metal-complexing-ligand *N*-methacryloylhistidine having PHEMA beads for heavy metal removal from aqueous solutions. Macromolecular Materials and Engineering, **287**, 539–545 (2002). DOI: 10.1002/1439-2054(20020801)287:8<539::AID-MAME539>3.0.CO;2-O

[33] Kara A., Uzun L., Beşirli N., Denizli A.: Poly(ethylene glycol dimethacrylate-*n*-vinyl imidazole) beads for heavy metal removal. Journal of Hazardous Materials, **106**, 93–99 (2004). DOI: 10.1016/j.jhazmat.2003.08.016

[34] Duran A., Soylak M., Tuncel S. A.: Poly(vinyl pyridine-poly ethylene glycol methacrylate-ethylene glycol dimethacrylate) beads for heavy metal removal. Journal of Hazardous Materials, **155**, 114–120 (2008). DOI: 10.1016/j.jhazmat.2007.11.037

eXPRESS Polymer Letters Vol.8, No.3 (2014) 197–206
Available online at www.expresspolymlett.com
DOI: 10.3144/expresspolymlett.2014.23

Poly (D,L-lactide-*co*-glycolide) nanoparticles: Uptake by epithelial cells and cytotoxicity

L. A. Nkabinde[1], L. N. N. Shoba-Zikhali[1], B. Semete-Makokotlela[2], L. Kalombo[2], H. Swai[2], A. Grobler[3], J. H. Hamman[4,5]*

[1]Council for Scientific and Industrial Research, Biosciences, P.O. Box 395, 0001 Pretoria, South Africa
[2]Council for Scientific and Industrial Research, Material Science and Manufacturing, Polymers and Bioceramics, P.O. Box 395, 0001 Pretoria, South Africa
[3]Pre-clinical Platform for Drug Development, North-West University, Private Bag X6001, 2520 Potchefstroom, South Africa
[4]Centre of Excellence for Pharmaceutical Sciences, North-West University, Private Bag X6001, 2520 Potchefstroom, South Africa
[5]Tshwane University of Technology, Department of Pharmaceutical Sciences, Private Bag X680, 0001 Pretoria, South Africa

Received 7 August 2013; accepted in revised form 29 October 2013

Abstract. Nanoparticles as drug delivery systems offer benefits such as protection of the encapsulated drug against degradation, site-specific targeting and prolonged blood circulation times. The aim of this study was to investigate nanoparticle uptake into Caco-2 cell monolayers, their co-localization within the lysosomal compartment and their cytotoxicity in different cell lines. Rhodamine-6G labelled poly(D,L-lactide-*co*-glycolide) (PLGA) nanoparticles were prepared by a double emulsion solvent evaporation freeze-drying method. Uptake and co-localisation of PLGA nanoparticles in lysosomes were visualized by confocal laser scanning microscopy. The cytotoxicity of the nanoparticles was evaluated on different mammalian cells lines by means of Trypan blue exclusion and the MTS assay. The PLGA nanoparticles accumulated in the intercellular spaces of Caco-2 cell monolayers, but were also taken up transcellularly into the Caco-2 cells and partially co-localized within the lysosomal compartment indicating involvement of endocytosis during uptake. PLGA nanoparticles did not show cytotoxic effects in all three cell lines. Intact PLGA nanoparticles are therefore capable of moving across epithelial cell membranes partly by means of endocytosis without causing cytotoxic effects.

Keywords: *biocompatible polymers, Caco-2 cells, cellular uptake, cytotoxicity, PLGA nanoparticles*

1. Introduction

Nanoparticles have received a lot of interest as carriers for drug molecules via the oral route of drug administration because they are capable to overcome certain drug delivery challenges. Nanoparticles can encapsulate a large variety of hydrophilic and hydrophobic drugs [1, 2], enhance the bioavailability of certain drugs, increase the residence time and can target specific tissues [3]. Nanoparticles also provide protection to drug molecules against enzymatic and hydrolytic degradation in the gastrointestinal tract [4] and can be directly taken up by enterocytes [5, 6]. Biomaterials that have been used as drug carriers include natural polymers (e.g. chitosan, cellulose, hydroxyapatite) and synthetic polymers (e.g. α-hydroxy acids such as poly(glycolic acid), poly(L-lactic acid) and poly(D,L-lactide-*co*-glycolide)) [7, 8]. The physical properties of nanoparticles prepared from natural polymers are less predictable and concerns were raised regarding their stability

*Corresponding author, e-mail: sias.hamman@nwu.ac.za

and immunogenicity. Synthetic polymers are therefore more favoured in some cases for drug delivery system development [9].

Poly(D,L-lactide-*co*-glycolide) (PLGA) is one of the most suitable polymers for bio-applications amongst the synthetic polymers owing to its favorable biodegradable and biocompatibility characteristics which has been proven over the past three decades [10]. This co-polymer degrades to compounds that are found in the human body (i.e. lactic and glycolic acid) and is safe for human consumption [11], which has been approved by the Food and Drug Administration (FDA) for use in drug delivery systems [12–14]. PLGA based nanoparticles are mainly produced by the double-emulsion, solvent evaporation or the spray drying techniques [15].

Since PLGA particles are hydrophobic in nature, the body recognizes them as foreign particles and eliminates them from the blood stream through the reticulo-endothelial system. This is probably one of the greatest disadvantages of particle-based controlled drug delivery systems [16] since long circulation times is key to optimised therapeutic outcomes for some drugs [17]. Researchers have attempted to overcome this limitation by modifying the surface properties of PLGA nanoparticles. This was achieved by coating with molecules that hide the hydrophobic nature of these nanoparticles by providing a hydrophilic layer at the surface and thereby increasing the blood circulation half-life of PLGA nanoparticles pronouncedly [18]. The most commonly used compounds for coating of PLGA micro- and nanoparticles are polyethylene glycol [19] and chitosan [20]. Although PLGA nanoparticle surface modification is done to improve its formulation properties [15], uncoated PLGA nanoparticles have been widely investigated to obtain fundamental information [21].

PLGA nanoparticles have been extensively investigated and have demonstrated good potential as carriers for several classes of drugs such as anticancer agents, antihypertensive agents, immunomodulators, hormones, nucleic acids, proteins, peptides and antibodies [22]. For purposes of oral drug delivery where prolonged blood circulation may be beneficial to the patient [23], it is important to investigate the movement of intact nanoparticles across epithelial cell monolayers and to identify the mechanisms by which these nanoparticles are taken up.

Since it is known that the interaction of nanoparticles varies from one cell line to another [24], it is important to test toxicity on the type of cells of interest. In this study, the toxicity of PLGA nanoparticles was investigated specifically in two epithelial cell lines (viz. Caco-2 and HeLa) and in a hepatic cell line (viz. HepG2). The epithelial cells were selected to represent the tissue type through which the nanoparticles are taken up after administration and the hepatic cells were selected to represent tissue from an organ to which the nanoparticles are exposed after uptake into the systemic circulation. The Caco-2 cell line originated from colorectal epithelial cells and under standard culturing conditions they spontaneously differentiate into columnar cells that resemble the characteristics of small intestinal enterocytes [25]. The Caco-2 cell line is an established *in vitro* model for predicting human intestinal drug permeability [26]. Both HeLa (human epithelial cells from cervical carcinoma) and HepG2 (human hepatocellular carcinoma cells) cells have been used successfully for *in vitro* toxicity studies [27]. Furthermore, both HeLa and HepG2 cell lines are commonly used to study three main cytotoxicity indicators (i.e Reactive oxygen species, intracellular glutathione depletion and calcein uptake) [28].

Although different *in vitro* methods are available to measure toxicity of compounds, the Trypan Blue exclusion method and MTS technique were utilised in this study to evaluate the toxicity effects of PLGA nanoparticles on the selected cell lines. Application of Trypan Blue dye to cells result in the selective staining of cells with compromised cell membranes. During the MTS technique, the compound 3-(4,5-dimethylthiazol-2-yl)-5-(3-carboxymethoxyphenyl)-2-(4-sulfophenyl)-2H-tetrazolium, is converted into a blue formazan dye by metabolically active mitochondria of viable cells [29–31].

The aim of this study was to determine the uptake and co-localisation of PLGA nanoparticles in the Caco-2 cell model by means of confocal laser scanning microscopy as well as to test the *in vitro* cytotoxicity of PLGA nanoparticles by means of Trypan Blue exclusion and MTS assays in the three selected cell lines (i.e. Caco-2, HeLa and HepG2).

2. Experimental

2.1. Materials and cell cultures

All mammalian cell cultures (i.e. Caco-2, HeLa and HepG2) were purchased from Highveld Biologicals (Pty) Ltd (Johannesburg, South Africa). The chemicals and growth media used to maintain cell growth

were purchased from Sigma-Aldrich (St. Louis, Mo, United State of America). These materials include Dulbecco's Modified Eagle's Medium (DMEM), Fetal Bovine Serum, penicillin/streptomycin solution and trypsin/EDTA. Hanks Balanced Salt Solution (HBSS), D-glucose, 4-(2-hydroxyethyl)-1-piperazineethanesulfonic acid (HEPES).

The following materials were employed to formulate poly(D,L-lactide-*co*-glycolide) (PLGA) nanoparticles and were purchased from Sigma-Aldrich (St. Louis, Mo, United State of America): 50:50 PLGA M_w = 40–75 kDa, with an inherent viscosity of 0.57 dL/g), polyvinyl alcohol (PVA, M_w = 13–23 kDa; 87–89% hydrolyzed) ethyl acetate, Rhodamine 6G fluorophore and phosphate buffer saline (PBS).

Tissue culture flasks and Transwell™ permeable supports were supplied by Corning-Costar® (Corning, New York, USA), while the LysoTraker Green DNP-26 dye used in the confocal laser scanning microscopy (CLSM) study was purchased from Celtic Molecular Diagnostic (Mowbray, South Africa). For toxicity studies, Trypan Blue dye and emetine were also purchased from Sigma-Aldrich (St. Louis, Mo, United State of America). CellTiter 96® AQ_{ueous} Non-Radioactive Cell Proliferation Assay kit used in MTS method was purchased from Promega Corporation (Madison, United State of America).

2.2. Formulation of poly(D,L-lactide-*co*-glycolide) nanoparticles

The PLGA nanoparticles were prepared using a double emulsion solvent evaporation method as previously described [32]. In brief, 100 mg of PLGA was dissolved in 8 mL ethyl acetate. For nanoparticle fluorescent labeling purposes, 1 mg of Rhodamine 6G was dissolved in 2 mL PBS at pH 7.4. The PLGA and Rhodamine 6G solutions were mixed and placed in an ice bath and then homogenized at 5000 rpm for 3 min using a high speed homogenizer (Silverson L4R, Silverson Machines Ltd, UK) to form the first oil-in-water (o/w) emulsion. This emulsion was poured into 40 mL of a 1% (w/v) PVA solution, which was homogenized at 8000 rpm for 3 min to form a water-in-oil-in-water (w/o/w) emulsion. This emulsion was stirred overnight on a magnetic stirring plate at 500 rpm to remove the organic solvent through evaporation under aseptic conditions. The pellet collected from the centrifugation step was placed at –72°C (for a minimum period of 2 h) prior to freeze drying. The particles were lyophilised using a Genesis 12, 25, 35 freeze-dryer (Virtis Co., New York, USA) for 24–48 h to obtain dry powder.

2.3. Characterization of the physical properties of the PLGA nanoparticles

The particle size, polydispersity index (PDI) as well as the zeta potential were determined by means of photon correlation spectroscopy using a Malvern Zetasizer Nano ZS apparatus (Malvern Instruments Ltd, Worcestershire, UK). A quantity of 2 mg of the lyophilized PLGA nanoparticles was suspended in 1 mL of distilled water and vortexed for 2 min and then introduced into the cell of the Zetasizer apparatus for analysis. The analysis of the nanoparticle sample was performed at 25°C in triplicate. The surface morphology of the PLGA nanoparticles was analyzed using a scanning electron microscope (LEO 1525 Field Emission scanning electron microscope, Zeiss, Oberkochen, Germany).

2.4. Caco-2 cell monolayer integrity

Transepithelial electrical resistance (TEER) measurements have become universally established as the most convenient method to evaluate and monitor the development of confluent epithelial cell culture monolayers. TEER was measured with a Millicell®-ERS meter (Microsep (Pty) Ltd, Johannesburg, SA) for 21 days until an acceptable reading has been obtained. A TEER value of ≥250 Ω/cm^2 was used as a reference point to indicate the formation of an intact monolayer in order to perform cellular uptake studies [33, 34]. TEER measurements were also used to check if the PLGA nanoparticles did not affect the monolayer integrity during treatment. At the end of the uptake experiment, the cell monolayers were washed with PBS and culture medium (DMEM) was added to both apical and basolateral chambers and incubated in the incubator for 48 h and the TEER was then measured to determine recovery. The following Equations (1) and (2) were used to calculate TEER and TEER difference [%]:

$$\text{TEER } [\Omega\cdot\text{cm}] = (T_{wc} - T_{nc})\cdot A \quad (1)$$

where T_{wc} is the TEER readings across filters with cells, T_{nc} is the TEER readings across filters without cells and A is the membrane surface area.

$$\text{TEER difference [\%]} = (T_{bt} - T_{at}) \cdot 100 \quad (2)$$

where T_{bt} is the TEER readings before treatment at 21 days, T_{at} is the TEER readings after treatment with PLGA nanoparticles.

2.5. Cellular uptake and lysosomal co-localization of the PLGA nanoparticles

Caco-2 cells at passage between 28–35 were seeded at a density of $1.5 \cdot 10^5$ cells/cm^2 on polycarbonate-treated filter membranes in Transwell plates (6-well plates, 0.4 μm pores, 4.7 cm^2 area) and monitored for at least 21 days until confluence was obtained. The culture medium (2 mL in the filter and 3 mL in the well) was replaced at every 48 h during monitoring of the cell monolayers. The culture medium was decanted off from the Caco-2 cells and the cells were then washed three times with phosphate buffer saline and equilibrated for 1 h in the incubator with the assay medium HBSS supplemented with 10 mM D-glucose and 10 mM HEPES (pH 7.4).

The Caco-2 cell monolayers were treated with 100 μg/mL of Rhodamine 6G-labelled PLGA nanoparticles and also stained with 1 μg/mL of LysoTraker Green DNP-26 dye in order to visualize the compartmentalization of nanoparticles within lysosomes. The cells were incubated over a 2 h period and the cells were visualized with the CLSM at 0.5, 1 and 2 h. At each time point, the medium was removed and the cells were washed with PBS to remove excess Rhodamine 6G-labelled PLGA nanoparticles. The filter membrane with attached cell monolayer was cut using a sterile blade and mounted to a microscope slide and the cover slip was put in place. The images were acquired with a filter that is appropriate for each fluorescent dye as described below.

These experiments were performed with a PCM2000 CLSM with a pinhole setting of $^1/_4$ Array Units used for optimal sample viewing. The fluorescence of LysoTraker Green DNP-26 (488 nm line of Argon Ion laser with 515 nm emission filter) and Rhodamine 6G (525 nm line of Helium-Neon laser with 550 nm emission filter) was monitored in different optical sections. Z-series of optical sections were acquired at spacing steps of 0.6 μm from the surface through the vertical axis of the specimen by a computer-controlled motor drive. Images were captured with EZ2000 Software and converted to Tag Image File Format.

2.6. Cytotoxicity of PLGA nanoparticles

2.6.1. Trypan blue exclusion

Caco-2, HeLa and HepG2 cells were seeded in 100 mm tissue culture dishes at a density of $1 \cdot 10^5$ cells/cm^2 and grown for 24 h in DMEM. The cells were washed three times with PBS and treated with 1.2 mg/mL of PLGA nanoparticles for 24 h. As a control, selected dishes containing cells from each cell line were not treated with nanoparticles. After the 24 h period, the cells were detached from the surface area with 1 mL trypsin/EDTA and neutralized with DMEM. Stained cells (i.e. non-viable cells) and non-stained cells (i.e. viable cells) were counted with a haemocytometer under an inverted microscope (Axiovert, Zeiss) to calculate the percentage viability of the cells.

2.6.2. MTS assay

Caco-2 cells were seeded in 96-well plates in 100 μL of culture medium at a density of $1 \cdot 10^4$ cells/well and grown for 24 h in culturing medium. The Caco-2 cells were then washed three times with PBS. The cells were then treated with 100 μL of PLGA nanoparticles suspensions prepared in DMEM with the following concentrations: 0.01, 0.07, 0.64 and 5.8 mg/mL. The positive control group consisted of emetine solutions with the following concentrations: 0.01, 0.07, 0.64 and 5.8 μg/mL. The plate was then incubated at 37°C, 5% CO_2 and 90% humidity conditions for 24 h after which 20 μL of a mixture of MTS-based solution were added directly into each well. The plate was then incubated for additional 3 h under same atmospheric conditions and the absorbance measured at 490 nm in a spectrophotometric microtitre plate reader (Tecan Infinite F500, Männedorf, Switzerland) against blank wells (with only DMEM) to subtract background absorbance at 690 nm. Cells incubated with DMEM without PLGA nanoparticles were used as a negative control. The cell viability was expressed as a percentage relative to the control as calculated by Equation (3):

$$\text{Cell viability [\%]} = \frac{OD_{sample}}{OD_{control}} \quad (3)$$

where OD_{sample} is the optical density of the test compound, $OD_{control}$ is the optical density of the control group (untreated cells).

2.7. Data analysis and statistics

All results reported in this article are expressed as mean±standard deviation (SD) of three replicates ($n = 3$), unless otherwise stated. Statistical evaluation was performed with Student's t test using Microsoft Office Excel (2007) merged with GraphPad Prism 4.0 (2008) (Microsoft Corporation, Redmond, Washington, USA). A probability (p) value of less than or equal to 0.05 was considered statistically significant.

3. Results and discussion

3.1. Physical properties of the PLGA nanoparticles

The Rhodamine 6G-labelled PLGA nanoparticles had an average size of 266.8±10.5 nm with a PDI value of 0.061±0.005, indicating a relatively narrow particle size distribution. The zeta potential of Rhodamine 6G-labelled PLGA nanoparticles was found to be –16.1±1.7 mV.

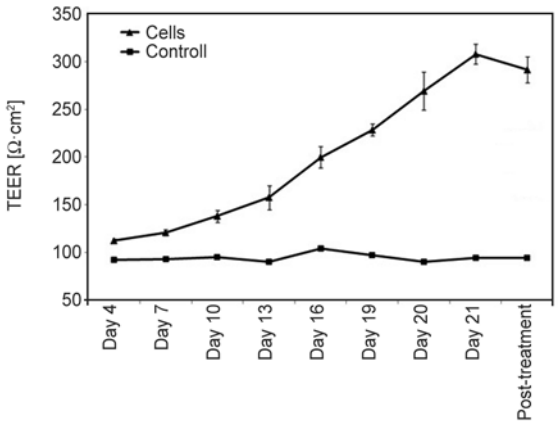

Figure 1. Transepithelial electrical resistance across the Caco-2 monolayers grown on a filter membrane as a function of culture time as well as before and after treatment compared to the control (filter membranes without cells)

3.2. Caco-2 cell monolayer integrity

The TEER values of the Caco-2 cell monolayers increased steadily over time under normal culturing conditions until values above 250 $\Omega \cdot cm^2$ were reached. This indicated that intact cell monolayers with well-developed tight junctions were formed. The decrease in TEER after treatment of the cell monolayers with PLGA nanoparticles was below 10%, which indicated that treatment with the PLGA nanoparticles did not compromise the cell monolayer integrity (Figure 1).

3.3. Cellular uptake of PLGA nanoparticles

Confocal laser scanning microscopy (CLSM) images presented in Figure 2 clearly indicate that the Rhodamine 6G-labeleld PLGA nanoparticles were internalized and accumulated within the Caco-2 cells in a time-dependent way. The Rhodamine 6G-labeleld PLGA nanoparticles were taken up to a lower extend after 30 min of incubation (Figure 2a) compared to 90 min incubation time (Figure 2b) as indicated by

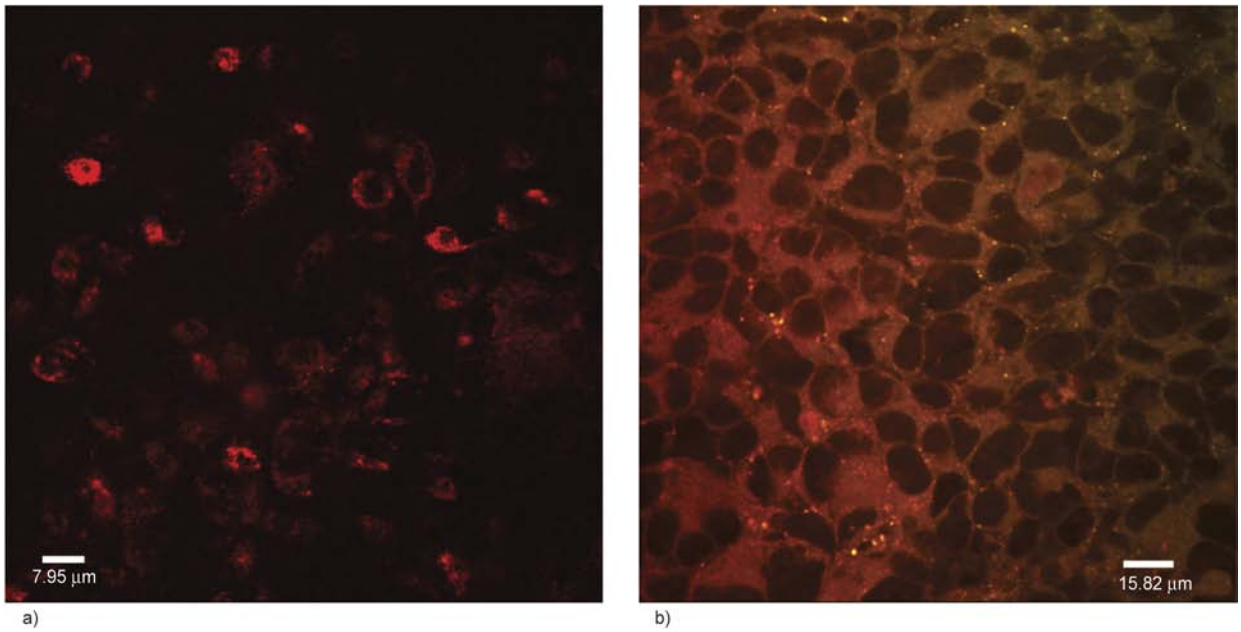

Figure 2. Confocal laser scanning microscopy images of Caco-2 cell monolayers treated with Rhodamine 6G-labelled PLGA nanoparticles after 30 min (a) and 90 min (b), respectively

the number of fluorescent dots in the cells. Figure 2b also indicates that accumulation of the Rhodamine 6G-labelled PLGA nanoparticles not only occurred within the Caco-2 cells, but they also accumulated in the intercellular spaces between the cells after 90 min of exposure time.

The fact that the PLGA nanoparticles have been internalized within the Caco-2 cells is in line with previous findings that indicated intact nanoparticles could gain access to the intracellular milieu of epithelial cells and could even move into cytoplasmic organelles [35].

3.4. Lysosomal co-localization of PLGA nanoparticles

Figure 3a shows a CLSM image of Rhodamine 6G-labelled PLGA nanoparticles taken up by a single Caco-2 cell (red fluorescing color) after 60 min incubation time, while the image in Figure 3b illustrates LysoTraker Green dye within the lysosomes (green fluorescing color) of the same cell. Figure 3c shows that the PLGA nanoparticles were co-loclize within some of the lysosomes of the cell as indicated by the yellowish fluorescence (some of which are pointed out by arrows on the image), which is a combination of both red and green fluorescence. This indicates that a portion of the PLGA nanoparticles were taken up by means of endocytosis and thereby co-localized within the lysosomes. The endocytosis pathway is the only uptake mechanism by which intracellular lysosomal/phagosomal co-localization of particles can be justified [36, 37]. Lysosomes are organelles that contain degradation enzymes which digest foreign particles [38], but a specialized endocytotic process (i.e. transcytosis) can escape endolysosomal degradation [39]. It was further confirmed in an *in vitro* study that nanoparticles taken up by means of transcytosis escaped lysosomal degradation to be released into the systemic circulation [40].

3.5. Cellular internalization of PLGA nanoparticles

In order to confirm that the PLGA nanoparticles were taken up into the Caco-2 cells and not only adsorbed onto the surface of the cell membrane, their uptake was quantified by acquiring and evaluating slices of the cell monolayer that was stacked together with cross-sectional slices perpendicular to the plane of the cell monolayer midpoint (*z*-axis). The *z*-direction image (Figure 4) shows that the Rhodamine 6G-labelled PLGA nanoparticles were taken up cross-sectional and when viewed from the side it is clear that they got transported from the apical surface of the cell membrane towards the basolateral membrane. The *z*-slices further show that PLGA nanoparticles were present in different planes throughout the thickness of the monolayer. This confirms transcellular uptake of the PLGA nanoparticles by intestinal epithelial cell monolayers and co-localisation in lysosomes (yellow fluorescence as indicated with arrows in Figure 3). In a previous study [41], localisation of PLGA nanoparticles was demonstrated within organelles such as the cell nucleus for particles in the 100 nm size range, whereas in this study the PLGA nanoparticles (with size of 266.8 nm) were found to be co-localised within the lysosomes. It is important to mention nanoparticle size and size distribution patterns are factors that may influence their interaction with the cell membrane [22]. Studies previously conducted on nanoparticles with an average size between 200 and 350 nm found that they were distributed to various tissues [32], while nano-

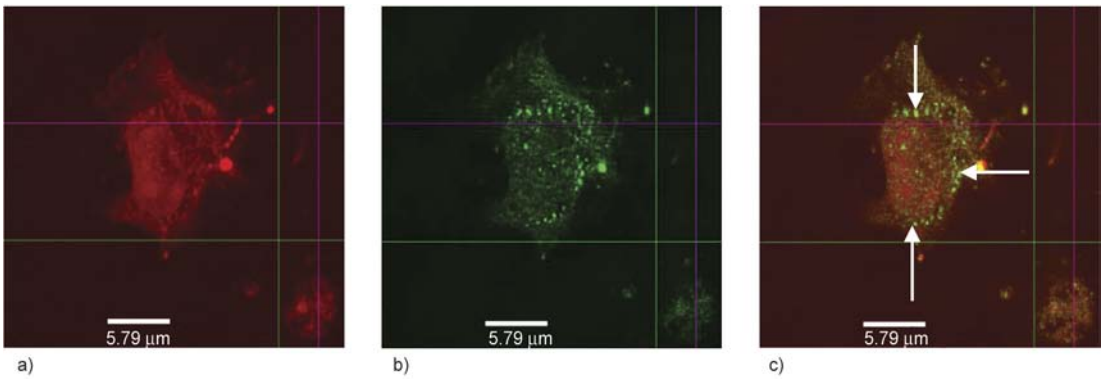

Figure 3. Confocal laser scanning microscopy images of a single Caco-2 cell exposed to Rhodamine 6G-labelled PLGA particles for 60 min. a) PLGA nanoparticles (red) taken up by the Caco-2 cell, b) compartmentalisation of green fluorescence from Lysotracker green within lysosomes in the Caco-2 cell and c) co-localisation of PLGA nanoparticles (yellowish green) within the lysosomes (indicated by arrows)

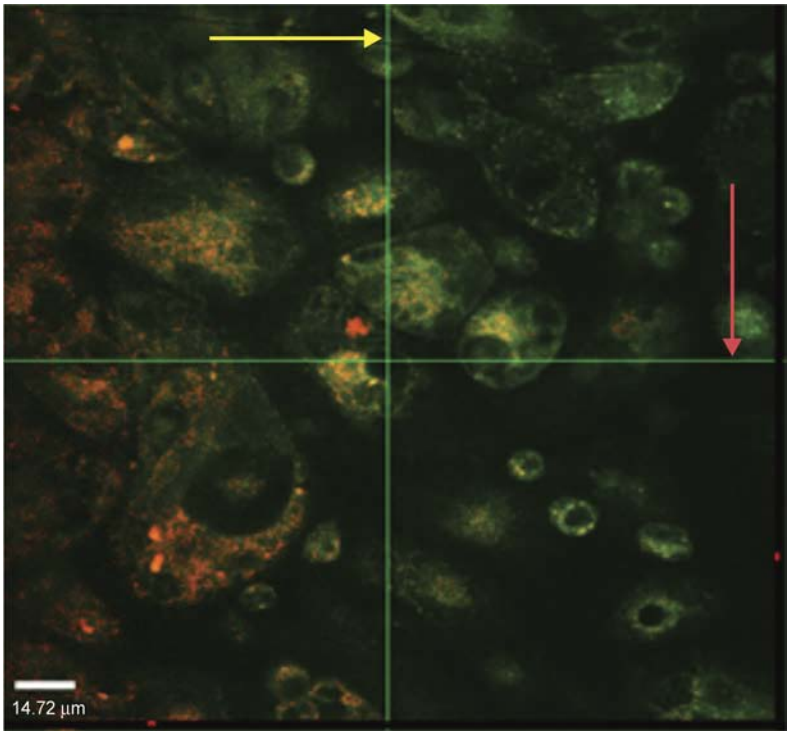

Figure 4. Z-stack images of Caco-2 cells 90 min after exposure to Rhodamine 6G-labelled PLGA nanoparticles. Images sectioned vertical (orange arrow) and parallel (red arrow) indicating cell adsorption of nanoparticles within cell monolayers

particles smaller than 70 nm was rapidly excreted by the kidneys. Surface charge or zeta potential of nanoparticles was also shown to be an important factor that may influence cellular internalization of nanoparticles, especially when they are oppositely charged than the cell's membrane [42].

3.6. Cytotoxicity of PLGA nanoparticles

3.6.1. Trypan blue exclusion and MTS assay

The viability of the different cell lines according to the Trypan blue exclusion test after exposure to PLGA nanoparticles is shown in Figure 5. There was no significant difference observed in the percentage cell viability for all three cell types (p = 0.95 for Caco-2; p = 0.91 for HepG2 and p = 0.63 for HeLa cells) between untreated cells (negative control) and those that were treated with PLGA nanoparticles at a concentration of 1.2 mg/mL. The trypan blue exclusion study therefore indicated that the PLGA nanoparticles were not cytotoxic to mammalian cell lines investigated. The MTS assay results confirmed that PLGA nanoparticles were not toxic to Caco-2 cells even when treated to a maximum concentration of 5.8 mg/mL (Figure 6) in comparison to emetine, which shown a markedly decrease in cell viability with increasing concentration (Figure 7). Team work previously conducted on similar PLGA nano-

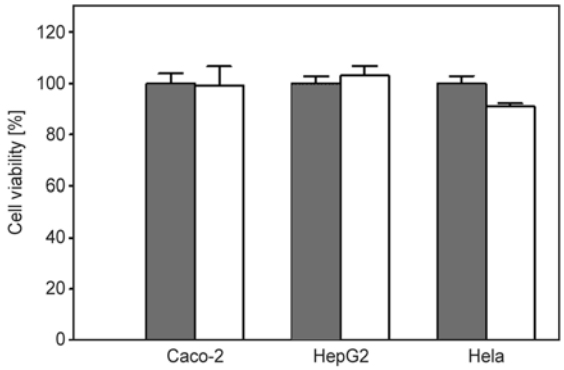

Figure 5. Viability of different mammalian cell lines determined by means of the Trypan blue exclusion test. (■) represents untreated cells (control) and (□) represents cells treated with PLGA nanoparticles. Data presented as mean ±SD, n = 3

particles used in this study showed that PLGA nanoparticles with an average size of 300 nm had no detrimental effects on mammalian cells including Caco-2 cells up to a concentration range of 0.001 mg/mL [32]. Particles prepared by the emulsion solvent evaporation technique were not toxic to human glioblastoma U87MG cells at 200 µg/mL [43] or mammalian cells [44, 45]. This study showed that PLGA nanoparticles are not toxic to Caco-2 cells even at relatively high concentrations, which have not been evaluated before. Emetine was used as the positive control (due to its toxicity on eukaryotic cells by

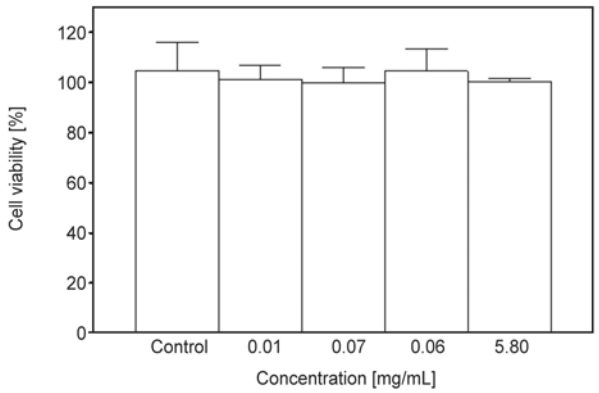

Figure 6. Viability of Caco-2 cells expressed relative to the control (not treated), which exposed to different concentrations of PLGA nanoparticles as determined by the MTS assay. Data presented as mean ±SD, $n = 3$

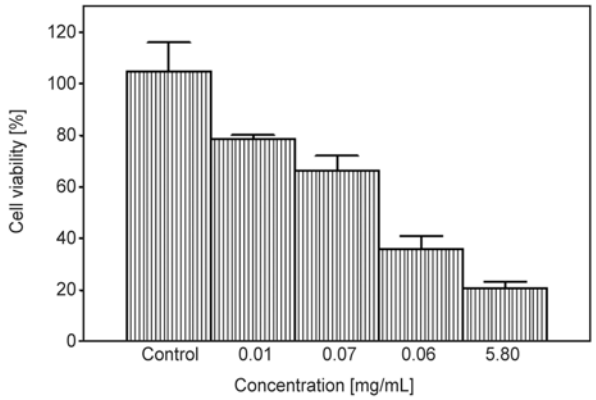

Figure 7. Viability of Caco-2 cells expressed relative to the control (not treated), which were exposed to various concentrations of emetine as determined by the MTS method. Data presented as mean ±SD, $n = 3$

blocking protein synthesis [46] and showed a toxic effect on the Caco-2 cells investigated in this study.

4. Conclusions

From the confocal laser scanning microscopy results it can be concluded that the PLGA nanoparticles accumulated to some extent in the intercellular spaces of Caco-2 cell monolayers which indicated paracellular movement of the nanoparticles across the epithelium. However, the PLGA nanoparticles were also clearly taken up by the transcellular pathway into the Caco-2 cells which indicated simultaneous transcellular movement. This transcellular uptake of the PLGA nanoparticles occurred partially through endocytosis as indicated by co-localisation in the lysosomes. Furthermore, PLGA nanoparticles were non-cytotoxic to three different mammalian cell lines, which confirm their safe use as drug carrier systems. Since it was shown in this study that intact PLGA nanoparticles move across epithelial cell monolayers without damaging these cells, they are suitable as drug carrier systems specifically for applications such as targeting specific tissues or to prolong blood circulation time after oral administration. It is recommended that future studies investigate the influence of physiological factors as well as physical properties of the nanoparticles on their mechanism of uptake in epithelial cells.

Acknowledgements

This study was supported in part by a grant-in-aid for Scientific Research (No. DMLIB-#49779-v2-MOA) from the Department of Science and Technology (DST) of South Africa. Also, gratitude expressed to CSIR Biosciences, for studentship financial support.

References

[1] Khuller G. K., Kapur M., Sharma S.: Liposome technology for drug delivery against mycobacterial infections. Current Pharmaceutical Design, **10**, 3263–3274 (2004).
DOI: 10.2174/1381612043383250

[2] Li X., Chen D., Le C., Zhu C., Gan Y., Hovgaard L., Yang M.: Novel mucus-penetrating liposomes as a potential oral drug delivery system: Preparation, *in vitro* characterization, and enhanced cellular uptake. International Journal of Nanomedicine, **6**, 3151–3162 (2011).
DOI: 10.2147/IJN.S25741

[3] Bob I.: Nanoparticle drug delivery systems. Innovation in Pharmaceutical Biotechnology, **24**, 58–62 (2007).

[4] Fattal E., Pecquet S., Couvreur P., Andremont A.: Biodegradable microparticles for the mucosal delivery of antibacterial and dietary antigens. International Journal of Pharmaceutics, **242**, 15–24 (2002).
DOI: 10.1016/S0378-5173(02)00181-3

[5] Desai M. P., Labhasetwar V., Walter E., Levy R. J., Amidon G. L.: The mechanism of uptake of biodegradable microparticles in Caco-2 cells is size dependent. Pharmaceutical Research, **14**, 1568–1573 (1997).
DOI: 10.1023/A:1012126301290

[6] Martinho N., Damgé C., Reis C. P.: Recent advances in drug delivery systems. Journal of Biomaterials and Nanobiotechnology, **2**, 510–526 (2011).
DOI: 10.4236/jbnb.2011.225062

[7] Anderson J. M., Shive M. S.: Biodegradation and biocompatibility of PLA and PLGA microspheres. Advanced Drug Delivery Review, **28**, 5–24 (1997).
DOI: 10.1016/S0169-409X(97)00048-3

[8] Nair L. S., Laurencin C. T.: Biodegradable polymers as biomaterials. Progress in Polymer Science, **32**, 762–798 (2007).
DOI: 10.1016/j.progpolymsci.2007.05.017

[9] Makadia H. K., Siegel S. J.: Poly lactic-*co*-glycolic acid (PLGA) as biodegradable controlled drug delivery carrier. Polymers, **3**, 1377–1397 (2011). DOI: 10.3390/polym3031377

[10] Jain R. A.: The manufacturing techniques of various drug loaded biodegradable poly(lactide-*co*-glycolide) (PLGA) devices. Biomaterials, **21**, 2475–2490 (2000). DOI: 10.1016/S0142-9612(00)00115-0

[11] Athanasiou K. A., Niederauer G. G., Agrawal C. M.: Sterilization, toxicity, biocompatibility and clinical applications of polylactic acid/polyglycolic acid copolymers. Biomaterials, **17**, 93–102 (1996). DOI: 10.1016/0142-9612(96)85754-1

[12] Chakravarthi S. S., Robinson D. H., De S.: Nanoparticulate drug delivery systems. in 'Nanoparticles prepared using natural and synthetic polymers' (eds.: Thassu D., Deleers M., Pathak Y.) Informa Healthcare, New York, 51–60 (2007).

[13] Lewis D. H.: Controlled release of bioactive agents from lactide/glycolide polymers. in 'Biodegradable polymers as drug delivery systems' (eds.: Chasin M., Langer R.) Marcel Dekker, New York, 1–41 (1990).

[14] Ishihara T., Kubota T., Choi T., Takahashi M., Ayano E., Kanazawa H., Higaki M.: Polymeric nanoparticles encapsulating betamethasone phosphate with different release profiles and stealthiness. International Journal of Pharmaceutics, **375**, 148–154 (2009). DOI: 10.1016/j.ijpharm.2009.04.001

[15] Mundargi R. C., Babu V. R., Rangaswamy V., Patel P., Aminabhavi T. M.: Nano/micro technologies for delivering macromolecular therapeutics using poly(D,L-lactide-*co*-glycolide) and its derivatives. Journal of Controlled Release, **125**, 193–209 (2008). DOI: 10.1016/j.jconrel.2007.09.013

[16] Kumari A., Yadav S. K., Yadav S. C.: Biodegradable polymeric nanoparticles based drug delivery systems. Colloids and Surfaces B: Biointerfaces, **75**, 1–18 (2010). DOI: 10.1016/j.colsurfb.2009.09.001

[17] Soppimath K. S., Aminabhavi T. M., Kulkarni A. R., Rudzinski W. E.: Biodegradable polymeric nanoparticles as drug delivery devices. Journal of Controlled Release, **70**, 1–20 (2001). DOI: 10.1016/S0168-3659(00)00339-4

[18] Owens D. E., Peppas N. A.: Opsonization, biodistribution, and pharmacokinetics of polymeric nanoparticles. International Journal of Pharmaceutics, **307**, 93–102 (2006). DOI: 10.1016/j.ijpharm.2005.10.010

[19] Danhier F., Feron O., Préat V.: To exploit the tumor microenvironment: Passive and active tumor targeting of nanocarriers for anti-cancer drug delivery. Journal of Controlled Release, **148**, 135–146 (2010). DOI: 10.1016/j.jconrel.2010.08.027

[20] Tahara K., Sakai T., Yamamoto H., Takeuchi H., Hirashima N., Kawashima Y.: Improved cellular uptake of chitosan-modified PLGA nanospheres by A549 cells. International Journal of Pharmaceutics, **382**, 198–204 (2009). DOI: 10.1016/j.ijpharm.2009.07.023

[21] Shenoy D. B., Amiji M. M.: Poly(ethylene oxide)-modified poly(ε-caprolactone) nanoparticles for targeted delivery of tamoxifen in breast cancer. International Journal of Pharmaceutics, **293**, 261–270 (2005). DOI: 10.1016/j.ijpharm.2004.12.010

[22] Danhier F., Ansorena E., Silva J. M., Coco R., Le Breton A., Préat V.: PLGA-based nanoparticles: An overview of biomedical applications. Journal of Controlled Release, **161**, 505–522 (2012). DOI: 10.1016/j.jconrel.2012.01.043

[23] Letendre L., Scott M., Dobson G., Hidalgo I., Aungst B.: Evaluating barriers to bioavailability *in vivo:* Validation of a technique for separately assessing gastrointestinal absorption and hepatic extraction. Pharmaceutical Research, **21**, 1457–1462 (2004). DOI: 10.1023/B:PHAM.0000036921.87928.72

[24] Vasir J. K., Labhasetwar V.: Quantification of the force of nanoparticle-cell membrane interactions and its influence on intracellular trafficking of nanoparticles. Biomaterials, **29**, 4244–4252 (2008). DOI: 10.1016/j.biomaterials.2008.07.020

[25] Hidalgo I. J., Raub T. J., Borchardt R. T.: Characterization of the human colon carcinoma cell line (Caco-2) as a model system for intestinal epithelial permeability. Gastroenterology, **96**, 736–749 (1989).

[26] Li A. P.: Screening for human ADME/Tox drug properties in drug discovery. Drug Discovery Today, **6**, 357–366 (2001). DOI: 10.1016/S1359-6446(01)01712-3

[27] du Plessis L. H., Hamman J. H.: *In vitro* evaluation of the cytotoxic and apoptogenic properties of aloe whole leaf and gel materials. Drug and Chemical Toxicology, in press, p.9 (2013). DOI: 10.3109/01480545.2013.834356

[28] Schoonen W. G. E. J., Westerink W. M. A., de Roos J. A. D. M., Débiton E.: Cytotoxic effects of 100 reference compounds on Hep G2 and HeLa cells and of 60 compounds on ECC-1 and CHO cells. I Mechanistic assays on ROS, glutathione depletion and calcein uptake. Toxicology in Vitro, **19**, 505–516 (2005). DOI: 10.1016/j.tiv.2005.01.003

[29] Mosmann T.: Rapid colorimetric assay for cellular growth and survival: Application to proliferation and cytotoxicity assays. Journal of Immunological Methods, **65**, 55–63 (1983). DOI: 10.1016/0022-1759(83)90303-4

[30] Vistica D. T., Skehan P., Scudiero D., Monks A., Pittman A., Boyd M. R.: Tetrazolium based assay for cellular viability: A critical examination of selected parameters affecting formazan production. Cancer Research, **51**, 2515–2520 (1991).

[31] Wrobel K., Claudio E., Segade F., Ramos S., Lazo K.: Measurement of cytotoxicity by propidium iodide staining of target cell DNA: Application to the quantification of murine TNF-α. Journal of Immunological Methods, **189**, 243–249 (1996).
DOI: 10.1016/0022-1759(95)00253-7

[32] Semete B., Booysen L., Lemmer Y., Kalombo L., Katata L., Verschoor J., Swai H. S.: *In vivo* evaluation of the biodistribution and safety of PLGA nanoparticles as drug delivery systems. Nanomedicine: Nanotechnology, Biology and Medicine, **6**, 662–671 (2010).
DOI: 10.1016/j.nano.2010.02.002

[33] Artursson P., Palm K., Luthman K.: Caco-2 monolayers in experimental and theoretical predictions of drug transport. Advanced Drug Delivery Reviews, **46**, 27–43 (2001).
DOI: 10.1016/S0169-409X(00)00128-9

[34] Hubatsch I., Ragnarsson E. E. G., Artursson P.: Determination of drug permeability and prediction of drug absorption in Caco-2 monolayers. Nature Protocols, **2**, 2111–2119 (2007).
DOI: 10.1038/nprot.2007.303

[35] Qaddoumi M. G., Ueda H., Yang J., Davda J., Labhasetwar V., Lee V. H.: The characteristics and mechanisms of uptake of PLGA nanoparticles in rabbit conjunctival epithelial cell layers. Pharmaceutical Research, **21**, 641–648 (2004).
DOI: 10.1023/B:PHAM.0000022411.47059.76

[36] Panyam J., Labhasetwar V.: Targeting intracellular targets. Current Drug Delivery, **1**, 235–247 (2004).
DOI: 10.2174/1567201043334768

[37] Cartiera M. S., Ferreira E. C., Caputo C., Egan M. E., Caplan M. J., Saltzman W. M.: Partial correction of cystic fibrosis defects with PLGA nanoparticles encapsulating curcumin. Molecular Pharmaceutics, **7**, 86–93 (2009).
DOI: 10.1021/mp900138a

[38] Ayala P., Lin L., Hopper S., Fukuda M., So M.: Infection of epithelial cells by pathogenic neisseriae reduces the levels of multiple lysosomal constituents. Infection and Immunity, **66**, 5001–5007 (1998).

[39] Panyam J., Zhou W-Z., Prabha S., Sahoo S. K., Labhasetwar V.: Rapid endo-lysosomal escape of poly(DL-lactide-*co*-glycolide) nanoparticles: Implications for drug and gene delivery. The FASEB Journal, **16**, 1217–1226 (2002).
DOI: 10.1096/fj.02-0088com

[40] Sanderson I. R., Walker W. A.: Uptake and transport of macromolecules by the intestine: Possible role in clinical disorder (an update). Gastroenterology, **104**, 622–629 (1993).

[41] Gaumet M., Gurny R., Delie F.: Localization and quantification of biodegradable particles in an intestinal cell model: The influence of particle size. European Journal of Pharmaceutical Sciences, **36**, 465–473 (2009).
DOI: 10.1016/j.ejps.2008.11.015

[42] He C., Hu Y., Yin L., Tang C., Yin C.: Effects of particle size and surface charge on cellular uptake and biodistribution of polymeric nanoparticles. Biomaterials, **31**, 3657–3666 (2010).
DOI: 10.1016/j.biomaterials.2010.01.065

[43] Mo L., Hou L., Guo D., Xiao X., Mao P., Yang X.: Preparation and characterization of teniposide PLGA nanoparticles and their uptake in human glioblastoma U87MG cells. International Journal of Pharmaceutics, **436**, 815–824 (2012).
DOI: 10.1016/j.ijpharm.2012.07.050

[44] Csaba N., Caamaño P., Sanchez A., Domınguez F., Alonso M. J.: PLGA:Poloxamer and PLGA:Poloxamine blend nanoparticles: New carriers for gene delivery. Biomacromolecules, **6**, 271–278 (2005).
DOI: 10.1021/bm049577p

[45] Mura S., Hillaireau H., Nicolas J., Le Droumaguet B., Gueutin C., Zanna S., Tsapis N., Fattal E.: Influence of surface charge on the potential toxicity of PLGA nanoparticles towards Calu-3 cells. International Journal of Nanomedicine, **6**, 2591–2605 (2011).
DOI: 10.2147/IJN.S24552

[46] Dimitrijevic S., Duncan R.: Synthesis and characterization of N-(2-Hydroxypropyl)-methacrylamide (HPMA) copolymer-emetine conjugates. Journal of Bioactive and Compatible Polymers, **13**, 165–178 (1998).
DOI: 10.1177/088391159801300301

eXPRESS Polymer Letters Vol.8, No.3 (2014) 207–218
Available online at www.expresspolymlett.com
DOI: 10.3144/expresspolymlett.2014.24

Preparation and comparative properties of membranes based on PANI and three inorganic fillers

K. C. Chang[1,2], *C. H. Hsu*[1], *C. W. Peng*[1], *Y. Y. Huang*[1], *J. M. Yeh*[1*], *H. P. Wan*[3], *W. C. Hung*[3]

[1]Department of Chemistry, Center for Nanotechnology and Biomedical Technology at Chung-Yuan Christian University (CYCU), Chung Li, 32023 Taiwan, Republic of China
[2]R&D Center for Membrane Technology, Chung-Yuan Christian University, Chung-Li, 32023 Taiwan, Republic of China
[3]Green Energy and Environment Research Laboratories, Industrial Technology Research Institute, Room 308B, Building 64, 195, Section 4, Chung Hsing Road, Chutung, 31040 Hsinchu, Taiwan

Received 14 August 2013; accepted in revised form 9 November 2013

Abstract. In this study, we compare the effects of aniline-modified mesoporous silica (AMS), raw silica (ARS) and non-modified raw silica (NRS) particles on the physical properties of as-prepared polyaniline (PANI)-silica mesocomposites (PSM) and nanocomposites (PSN) and PANI-raw silica (PRSN) membranes. First, aniline-modified silica particles were synthesized by a conventional base-catalyzed sol-gel reaction of tetraethyl orthosilicate (TEOS) in the presence or absence of N-[3-(Trimethoxysilyl) propyl]aniline (PAPTMS). Subsequently, PSM, PSN and PRSN materials were prepared through *in situ* oxidation polymerization reaction of aniline monomer in the presence of AMS, ARS and NRS particles. It should be noted that all the properties of PSM membranes improved substantially from those of PSN and PRSN. For example, upon 3 wt% loading of AMS particles, 10, 25, 10, and 85% increases in thermal stability, mechanical strength, surface hydrophilicity and gas permeability were observed for PSM membranes, respectively, as well as more than 45% reduction in the thermal conductivity.

Keywords: *nanocomposites, polyaniline, silica, mesocomposite, membrane*

1. Introduction

Organic-inorganic nanoparticle composite materials have gained substantial industrial and academic interest in recent years. Incorporating inorganic nanoparticles into organic polymers will improve the mechanical, thermal, optical and barrier properties. Commonly used inorganic additives include clay [1, 2], SiO_2 [3–5], carbon nanotubes [6, 7], and carbon nanofibers [8], among others.

Polyaniline (PANI) is a potential material for commercial applications owing to its facile synthesis, relatively low cost, environmental stability, good processability, and unique optical, electrical and electrochemical properties [9, 10]. In recent decades, extremely promising applications have been reported for PANI in optical [11] and nanoelectronic devices [12], batteries [13], sensors [14], electrorheological materials [15, 16] and so on.

Mesoporous materials are a new class of nanoscale materials that possess large surface areas and have pore sizes that can be tuned within 2–10 nm in a very narrow distribution by varying the preparation conditions. Numerous potential applications of these materials are expected in the areas of catalysis, separation, adsorption and advanced materials. Recently, mesoporous silica-reinforced polymer composites have attracted considerable interest due to the possibility of improving the mechanical and thermal properties of polymers [17, 18]. Other interesting properties of these composites are, for example, low

*Corresponding author, e-mail: juiming@cycu.edu.tw

dielectric constants [19], low thermal expansion properties [20], and excellent friction and wear performances [21]. The incorporation of a guest monomer or polymer into the channels of mesoporous materials is a key factor contributing to the dispersion of additives in the polymer matrix and the enhancement of the properties of as-prepared composites.

There is a considerable amount of literature associated with the preparation and properties of polymer-silica meso- and nanocomposite materials. However, there are fewer reports on the systematic comparative studies on their preparation and properties. In recent years, our group has reported the preparation of PMMA-silica [22] and PS-silica [23] meso- and nanocomposite membranes (thermoplastic polymer systems) and compared the incorporation of silica and mesoporous silica particles. The mesocomposite membranes exhibited enhanced mechanical strength, thermal stability, thermal and electric insulation, optical clarity, and surface hydrophobic properties in comparison to nanocomposite membranes. In general, comparative studies on the physical properties of conducting polymer-silica mesocomposites and their corresponding nanocomposite membranes have seldom been reported.

Therefore, in this paper, we present a systematic comparative study on the preparation and properties of as-prepared polyaniline (PANI)-silica mesocomposite (PSM), nanocomposite (PSN) and PANI-raw silica (PRSN) membranes. First, we synthesized aniline-modified mesoporous silica (AMS) and raw silica (ARS) particles by conventional base-catalyzed sol-gel reaction of TEOS in the presence of PAPTMS. Non-modified raw silica (NRS) particles were also synthesized by the base-catalyzed sol-gel reactions. The as-prepared particles were then characterized by Fourier transformation infrared (FTIR), ^{13}C-nuclear magnetic resonance (NMR), and ^{29}Si-NMR spectroscopies. Subsequently, meso- and nanocomposite materials were prepared by *in situ* oxidation polymerization of aniline in the presence of as-prepared AMS, ARS or NRS particles. The dispersibility of silica particles in the PANI matrix was further studied by transmission electron microscope (TEM). Gel permeation chromatography (GPC) was used for determining the molecular weights of as-prepared samples. The effect of material composition on the thermal stability, mechanical strength, thermal transport, surface and gas permeability properties of PSM, PSN and PRSN membranes were investigated by thermo-gravimetric analysis (TGA), dynamic mechanical analysis (DMA), the transient plane source (TPS) technique, contact angle measurement and gas permeability analysis (GPA) technique, respectively.

2. Experimental

2.1. Materials and instrumentation

Aniline (Fluka, Germany, 98.0%) was used as a monomer and ammonium persulfate (APS, Fluka, Germany, 98.0%) as an oxidant for the preparation of polyaniline. Tetraethyl orthosilicate (TEOS, Fluka, Germany, 98%) and N-[3-(Trimethoxysilyl)propyl] aniline (PAPTMS, Aldrich, Germany) were used as a sol-gel precursor and silane coupling agent, respectively. D-(-)-Fructose (Aldrich, Germany, 99.0%), ethanol (EtOH, Riedel-de Haën, Germany, 99.8%), hydrochloric acid (HCl, Riedel-de Haën, Germany, 37%), ammonia solution (NH_3, Riedel-de Haën, Germany, 25%), and N-methyl-2-pyrrolidinone (NMP, Tedia, USA, 99.0%) were used without any further purification.

Brunauer-Emmett-Teller (BET, USA) characterizations were performed on a Micrometrics ASAP 2010 micropore analysis system at –196°C using a nitrogen adsorption-desorption isotherm method. The samples were degassed at 120°C and 1 Pa overnight prior to the measurement. Pore sizes were obtained from the maximum of the pore-size distribution using a BJH model applied to the adsorption data. Both ^{13}C and ^{29}Si MAS solid-state NMR experiments were performed on a 400 MHz Chemagnetics solid-state NMR spectrometer (BRUKER AVANCE 400, USA). ^{13}C MAS NMR spectra were obtained at 100.63 MHz using a MAS frequency of 7 kHz and applying 90° pulses at 2.0 s pulse delays. To enhance the carbon sensitivity, cross-polarization (CP) techniques were employed. ^{29}Si MAS NMR spectra were recorded at 79.49 MHz in 5.0 mm zirconia sample rotors spinning at 7 kHz, applying 90° pulses, 300 s pulse delays, and 5.0 ms contact time. FTIR spectra were obtained at a resolution of 4.0 cm^{-1} with a FTIR (JASCO FT/IR-4100, Japan) spectrophotometer at room temperature in a wavenumber range from 4000 to 400 cm^{-1}. The microstructures of PSM and PSN membranes were imaged with a JEOL-200FX TEM (Japan). The samples for the TEM study were cut into 60–90 nm thick-sections with a diamond knife. The number-average and weight-average molecular

weights of the polymers extracted from all composite samples and from the hybrid materials were determined on a Waters GPC-150CV (USA) equipped with a differential refractometer detector and a Styragel HT column using NMP as eluent and monodisperse polystyrenes as calibration standards. TGA was employed to record the thermal stability of the specimens. TGA scans were performed on a DuPont TA Q50 (USA) thermal analysis system in air atmosphere. The scan rate was 20°C/min in a temperature range from 30 to 800°C. DMA of the PSM and PSN membranes was performed in a temperature range from 40 to 300°C on a DuPont TAQ800 (USA) analyzer at a heating rate of 3°C/min and at a frequency of 1 Hz. The sample dimension was 10 mm×5 mm. Thermal transport measurements employed a Hot Disk Thermal Constants Analyzer TPS (Taiwan) supplied by Hot Disk Inc. Contact angles of the samples were measured using a First Ten Angstroms FTA 125 (Germany) with a membrane thickness of 40 μm. A Yanagimoto Co., Ltd. gas permeability analyzer (model GTR 10, Japan) was employed to perform oxygen/nitrogen gas permeation experiments.

2.2. Synthesis of aniline-modified raw silica (ARS) particles

Aniline-modified silica (denoted as ARS) was prepared by a sol-gel reaction of TEOS and PAPTMS under base-catalyzed conditions, as shown in Figure 1. The typical procedure is as follows: 300 mL ethanol, 5.2 g D-(-)Fructose and 4 mL 15 M NH_3 solution were mixed and stirred for 10 min at room temperature. Simultaneously, a mixture of 5.2 g of TEOS and 1 g of PAPTMS was stirred in another container at room temperature. Then, this solution was slowly added to the first solution and stirred overnight. The mixture was centrifuged in ethanol five times to remove NH3, followed by drying in a vacuum oven. Non-modified raw silica (NRS) particles were also prepared as a reference without the addition of PAPTMS monomer, as shown in Figure 1.

2.3. Synthesis of aniline-modified mesoporous silica (AMS) particles

Aniline-modified mesoporous silica (denoted as AMS) was obtained by NH_3-catalyzed sol-gel reaction of tetraethylorthosilicate (TEOS) and N-[3-(Trimethoxysilyl)propyl]aniline (PAPTMS) in the presence of non-surfactant template, D-(-)-Fructose, followed by the template removal by centrifugation, as shown in Figure 1. The procedure for the preparation of AMS in this work is as follows: 300 mL ethanol solution, 5.2 g D-(-)-Fructose and 4 mL 15 M NH_3 solution were mixed and stirred for 10 min at room temperature. Simultaneously, the mixture, of 5.2 g of TEOS and 1 g of PAPTMS was stirred in other container at room temperature. Then, this solution was slowly added into the first solution and stirred overnight. The mixture was centrifuged in

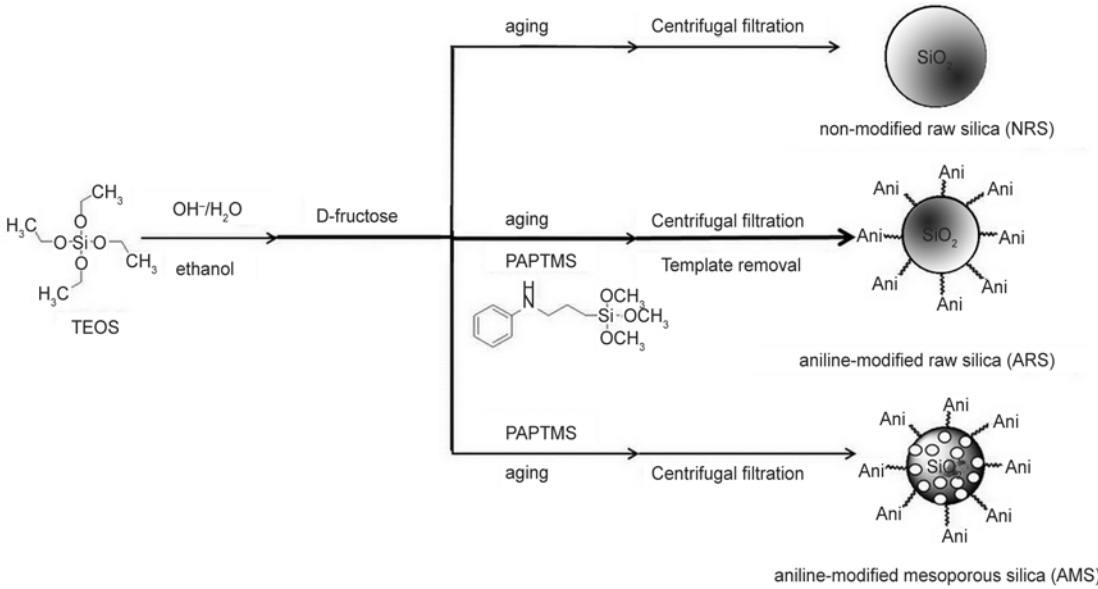

Figure 1. Synthesis of non-modified raw silica (NRS), aniline-modified raw silica (ARS) and aniline-modified mesoporous silica (AMS) particles

ethanol five times to remove NH_3 and in deionized water to remove D-(-)-Fructose, followed by drying in a vacuum oven.

2.4. Preparation of PSM and PSN materials

A typical procedure for the preparation of PSM and PSN materials was shown in Figure 2 and is given as follows: aniline monomer (0.1 mol) was added to 400 mL of 1.0 M HCl, and various amounts of AMS (1, 3 wt%), ARS (3 wt%) or NRS (3 wt%) were fully dispersed in the solution under magnetic stirring. After adding APS (0.025 mol) in 20 mL of 1.0 M HCl, the solution was stirred for 6 h on an ice bath. The as-synthesized HCl-doped PSM or PSN precipitates were then filtered and dried under dynamic vacuum at 40°C for 2 d. The final PSM or PSN materials were obtained in a base form by immersing them into 400 mL of 1.0 M NH_4OH under magnetic stirring for 4 h at room temperature, followed by the filtration and drying under vacuum at 40°C for 2 d.

2.5. Preparation of composite membranes

0.2 g sample of PSM or PSN material in a base form was dissolved in 10 mL of NMP under magnetic stirring at room temperature for 1 d. The solution was cast onto a substrate (e.g., glass), and the solvent was evaporated in an oven for 1 d. The sample-coated glass substrate was then immersed in distilled water to yield PSM and PSN membranes. The membrane thickness was about 45 μm.

3. Results and discussion

Aniline-modified mesoporous silica (AMS) nanoscale particles with a wormhole framework structure were prepared by an energy-saving and environmentally friendly non-surfactant template route, developed by Wei *et al*. [24]. First, a TEOS/PAPTMS feed ratio of 8/2 (i.e., AMS82) and an optically active D-(-)-Fructose non-surfactant as a template were used in the conventional base-catalyzed sol-gel reaction, followed by a template removal through

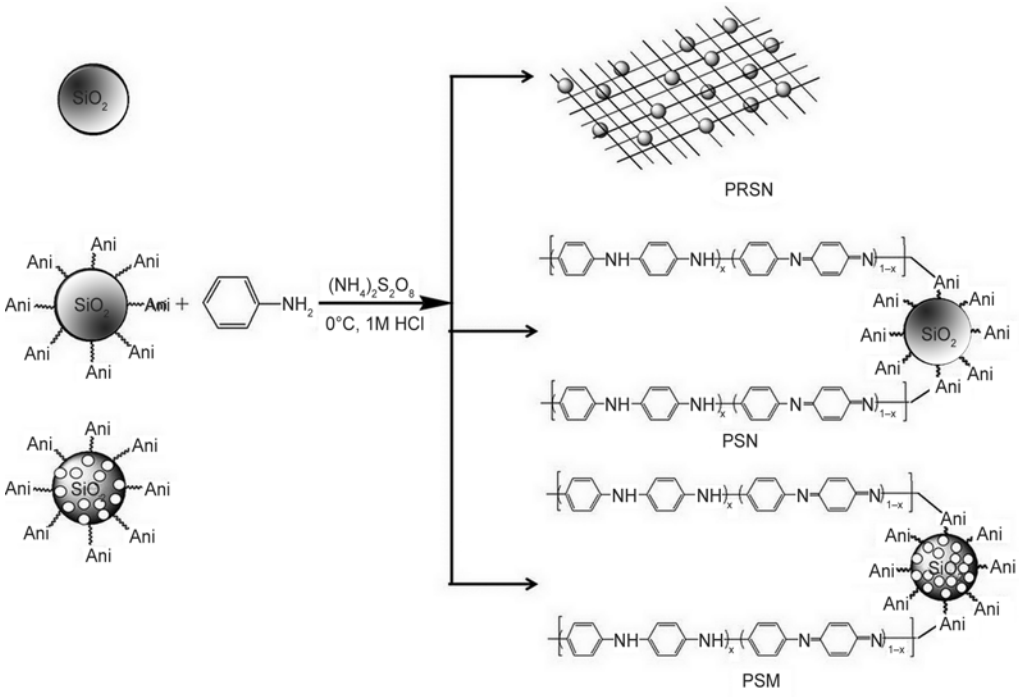

Figure 2. Preparation of PANI-raw silica (PRSN), and PANI-silica mesocomposite (PSM) and nanocomposite (PSN)

Table 1. Physical properties of nanoscale aniline-modified mesoporous and raw silica particles and PSM materials

Sample code	TEOS [mol]	PAPTMS [mol]	D-Fructose [wt%]	D_p [nm][a]	V_t]cm^3/g][b]	S_{BET} [m^2/g][c]
RS	0.0254	–	–	–	0.03	14.1
ARS82	0.0250	0.0004	–	–	0.03	8.2
MS	0.0254	–	2	3.3	0.70	587.0
AMS82	0.0250	0.0004	2	3.4	0.50	506.0
PSM3	0.0250	0.0004	2	12.6	0.20	51.4

[a]Pore diameter.
[b]Total pore volume calculated from $P/P_0 = 0.99$.
[c]BET surface area.

Soxhlet extraction. The aniline-modified raw silica (ARS) and non-modified raw silica (NRS) nanoscale particles were also prepared as references for systematic comparative studies. Specific surface area, ABET, determined from the linear part of BET plot, and pore size obtained from the maximum of pore size distribution using a BJH model applied to the adsorption data are summarized in Table 1. Subsequently, the selected amount of as-prepared AMS82/ARS82/NRS82 particles was reacted with aniline monomer by free radical solution polymerization in toluene with APS initiator to give a series of polymer-silica meso- or nanocomposite materials.

3.1. Characterization

3.1.1. Microstructure of nanoscale silica particles and corresponding PANI-silica meso- and nanocomposite membranes

BET surface areas and pore volumes of the samples were determined by N_2 adsorption-desorption isotherm measurements [25]. The isotherms of silica materials are shown in Figure 3. The aniline-modified silica particles showed relatively small BET surface areas and pore volumes compared to the non-modified silica particles (i.e., MS and RS), as summarized in Table 1. Moreover, MS particles prepared at 2 wt% D-(-)-Fructose template concentration exhibited type IV isotherms with type H_2 hysteresis loops, showing one capillary adsorption at partial pressures (P/P_0) of 0.4–0.8 (Figure 3a), and are attributed to the mesopores [26]. The characteristic feature of the isotherms above is the hysteresis loop, which is associated with the capillary condensation taking place in the mesopores [27, 28] and the limiting uptake at high partial pressures. The initial part of the MS (without PAPTMS) isotherm was attributed to monolayer-multilayer adsorption, as it follows the same path as the non-porous adsorbent with the same surface area. The characteristics of the remaining two isotherms are the hysteresis loops widely distributed to the lower partial pressure (P/P_0) range of 0.01–0.8. The samples with up to 20% PAPTMS show a steep increase in the adsorption at P/P_0 of 0.4–0.8, indicating that the obtained materials possess large mesopores and narrow pore-size distribution similar to the pure silica, as the high amount of large functional group silanes occupy larger pore volume. On the other hand, samples containing 20% PAPTMS have apparently lower absorption volumes and narrower pore diameter. Moreover, Barrett-Joyner-Halenda (BJH) pore diameter [29], BET surface area, and pore volume of AMS decreased with increasing aniline content, as shown in Figure 3b and Table 1. These results were attributed to the occupation of the pore surface by large organic molecules, as well as to the perturbation of aniline groups during the silicate condensation process [26]. Further compare the pore volume of AMS particles and PSM3 materials, the pore volume of PSM3 is reduced to 0.2 from 0.5 cm^3/g for AMS particles as a consequence of pore filling by PANI [30].

3.1.2. Spectroscopic studies of AMS82/ARS82/NRS82 particles

In this study, the as-prepared AMS particles were synthesized by base-catalyzed sol-gel reaction of TEOS in the presence of PAPTMS, and subsequently characterized by FTIR, ^{13}C-NMR and ^{29}Si-NMR spectroscopies. Figure 4 shows the representative FTIR spectra of D-(-)-Fructose and the as-prepared NRS, ARS and AMS particles. For example,

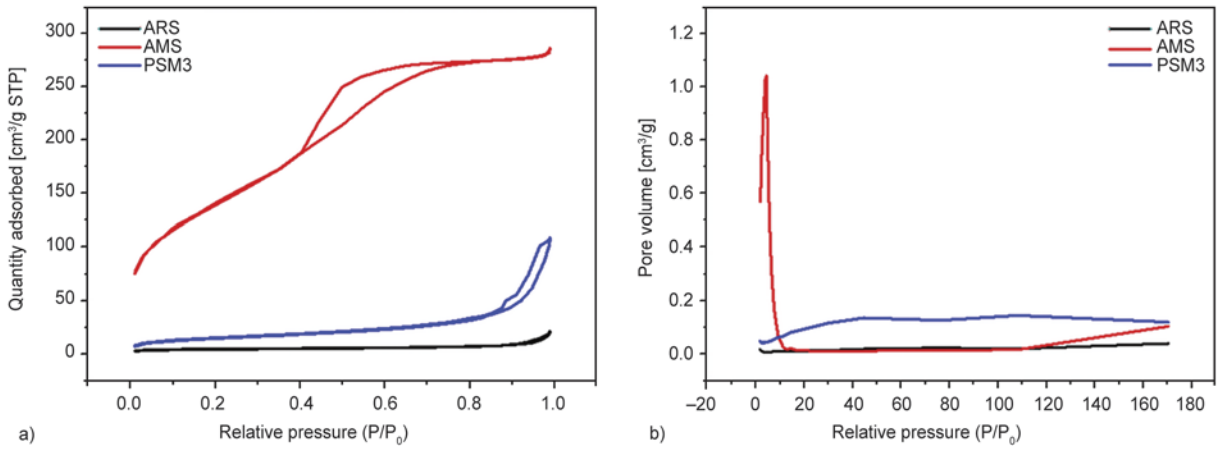

Figure 3. (a) N_2 adsorption/desorption isotherms and (b) pore size distributions of ARS, AMS particles and PSM3 materials

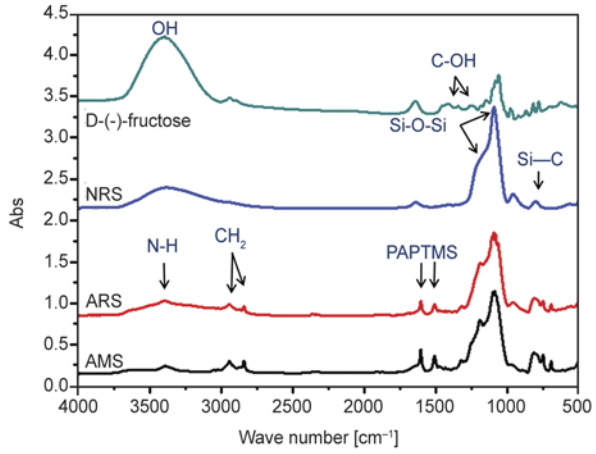

Figure 4. FTIR absorption spectra of D-(-)-Fructose, and NRS, ARS and AMS particles

the spectral bands characteristic of the aniline group of PAPTMS appearing at 1607 and 1505 cm^{-1} were assigned to the stretching of C=N and C=C, corresponding to quinone and benzene ring stretching deformations, respectively. The positions of the absorption peaks are similar to those reported in refs. [31–34]. The presence of organic groups in the materials after the hydrolysis and condensation was confirmed by solid-state NMR spectroscopy. Figure 5 shows the solid-state ^{13}C CP MAS NMR spectra of AMS particles, where the AMS particles exhibit additional resonance peaks at chemical shifts δ = 8.41, 21.15, 46.10, 117.14, 129.35 and 146.43 ppm. These peaks are attributed to the different carbon environments in the organosilane, denoted as groups 1–3 and 4–6 [35], indicating the incorporation of aniline functional groups. Moreover, solid-state ^{29}Si MAS NMR provided information about the silicon environment. The ^{29}Si MAS NMR spectra of AMS particles are presented in Figure 6. Two resonance peaks arising from the silicon environments of $Si(OSi)_4$ (Q^4, δ = –113.79 ppm)

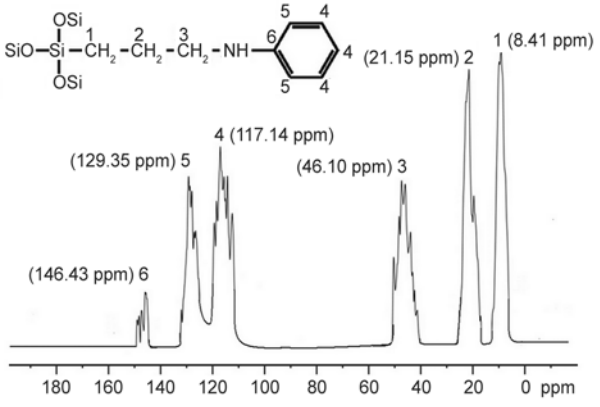

Figure 5. ^{13}C solid-state NMR spectra of AMS particles

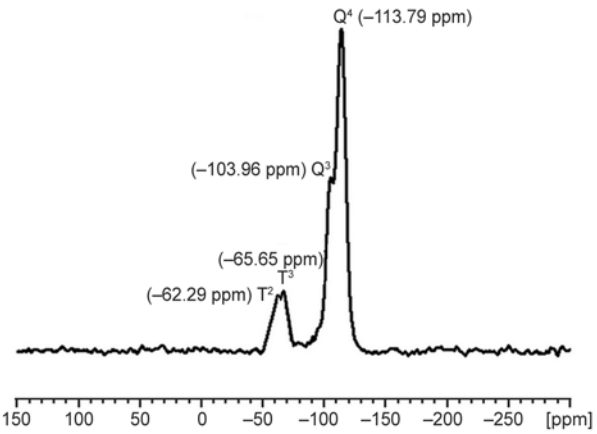

Figure 6. ^{29}Si solid-state NMR spectra of AMS particles

and $HOSi(OSi)_3$ (Q^3, δ = –103.96 ppm) can be observed [35]. In addition, the AMS particles display two more resonance peaks at δ = –65.65 ppm, assigned to $R\text{-}Si(OSi)_3(T^3)$, and at δ = –62.29 ppm, attributed to $R\text{-}Si(OH)(OSi)_2(T^2)$ [35]. These two peaks arise from the silicon atoms at different environments in the organosilane PAPTMS.

3.1.3. FTIR spectra of PANI-silica mesocomposites

The FTIR spectra of AMS particles, PANI and PSM3 are shown in Figure 7. The FTIR spectrum of AMS particles shows the absorption bands at 1096 cm^{-1} (asymmetric Si–O–Si stretch), 956 cm^{-1} (Si–OH vibrations) and 816 cm^{-1} (symmetric Si–O–Si stretch). In the case of PANI, the main peaks at 1588 and 1483 cm^{-1} can be assigned to the stretching vibrations of quinone and benzene rings, respectively. The peaks at 1282 correspond to the C–N stretching vibration. The in-plane bending of C–H is reflected in the 1155 cm^{-1} peak. The peak at 810 cm^{-1} is attributed to the out-of-plane bending of C–H. The FTIR spectrum of PSM3 implies that the mesocomposites contained the characteristic peaks of AMS and PANI. As expected, when com-

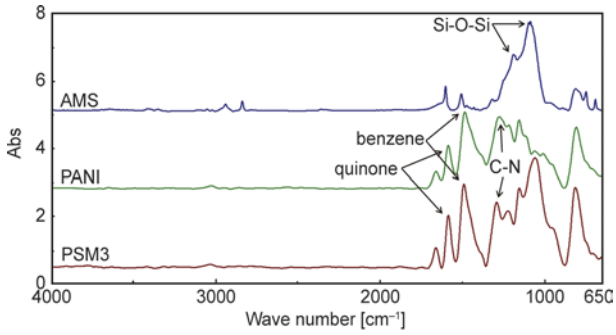

Figure 7. FTIR spectra of AMS particles, PANI and PSM3

paring the spectra of PANI and the mesocomposites, the absorption bands all shift to higher wavenumbers in the mesocomposites. These phenomena indicate that some interaction of PANI with the host [36, 37].

3.1.4. Morphological observations of silica particles and corresponding PANI-silica meso- and nanocomposite membranes

The morphology of the silica particles and their corresponding PANI-silica meso- and nanocomposites can be directly confirmed by TEM. Figure 8 shows the TEM images of the silica and mesoporous silica particles synthesized in this work. The NRS (Figure 8a), ARS (Figure 8b) and AMS particles (Figure 8c) have the sizes of about 250 and 300 nm, respectively, and they are spherical. The mesoporous silica nanospheres have cylindrical channels and highly ordered mesoporous structure (Figure 8c). Figure 9 shows the TEM images of PANI/silica meso- and nanocomposites. With the exception of the composites made from ARS and AMS particles (Figure 9b–c), the images exhibit silica and mesoporous silica nanoparticles with sizes ranging from about 200 to 300 nm, relatively well-dispersed in the polymer matrix. However, the TEM image of PRSN3 obviously shows the aggregation of silica particle into clusters, indicating the poor dispersibility of silica particles in the PANI matrix in contrast to aniline-modified silica and mesoporous silica nanoparticles, as shown in Figure 9a.

3.1.5. Molecular weights and polydispersity of composite membranes

Molecular weights of neat polymer and various composites were obtained by GPC analyses using THF as an eluent. All the GPC traces of samples exhibited a single peak, represented by the molecular weight values summarized in Table 2. The molecular weights of all composite materials were lower than that of neat PANI, indicating structurally restricted polymerization in the neighboring region of silica particles (e.g., NRS82/ARS82/AMS82) and/or silica-oligomer interactions, such as adsorption, during the polymerization reaction. For example, the values of weight-average molecular weight ($\bar{M}_w$), number-average molecular weight ($\bar{M}_n$) and polydispersity (PDI) of neat PANI are 25 600, 12 100 and 2.12, respectively. Upon the incorporation of 3 wt% of AMS82 particles into PANI (i.e., PMS3) by *in situ* solution polymerization, these values showed a clearly decreasing trend to 22 000, 10,500 and 2.09, respectively. Moreover, the decreasing trend of molecular weights and PDI of the nanocomposite system is very close to that of mesocomposite system, and thus, the reactive channel aniline groups of nanoscale mesoporous silica show a slight effect on the molecular weights and molecu-

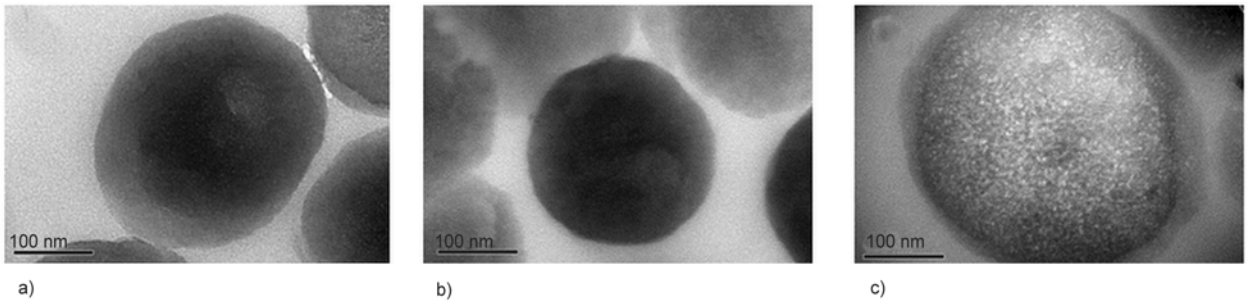

Figure 8. TEM images of (a) NRS, (b) ARS, and (c) AMS particles

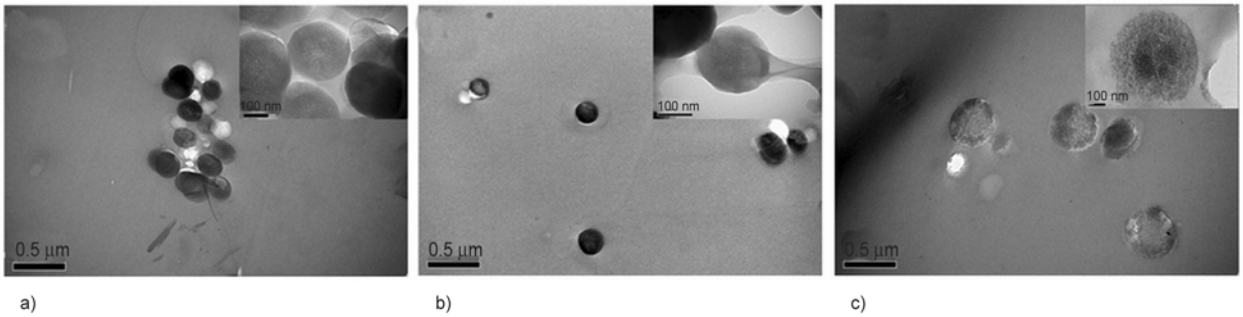

Figure 9. TEM images of (a) PRSN3, (b) PSN3 and (c) PSM3. Illustration is the large magnification of images (50 k).

Table 2. Molecular weight, thermal, mechanical, surface hydrophobic and gas permeability properties of PANI and composite membranes

Compound code	Feed composition [wt%]				Molecular weight			Thermal properties		Mechanical properties	Contact angle [°]	Permeability [barrer][e]		Permselectivity
	PANI	RS	ARS	AMS	$\bar{M}_w$	$\bar{M}_n$	PDI[a]	T_d [°C][b]	k [W/(m·K)][c]	E′ [MPa][d]		P_{O_2}	P_{N_2}	α_{O_2/N_2}
PANI	100	–	–	–	25 600	12 100	2.12	440.70	0.0933	2610	90±2	0.1972	0.0305	6.4585
PRSN3	97	3	–	–	21 200	11 200	1.90	460.60	0.1504	2720	93±2	0.1889	0.0292	6.4582
PSN3	97	–	3	–	23 200	10 500	2.22	470.50	0.1153	3020	92±2	0.1892	0.0293	6.4581
PSM1	99	–	–	1	25 000	13 100	1.91	480.30	0.0618	3240	85±2	0.3608	0.0567	6.3616
PSM3	97	–	–	3	22 000	10 500	2.09	490.90	0.0498	3320	80±2	0.3696	0.0602	6.1407

[a]PDI = $\bar{M}_w/\bar{M}_n$.
[b]As measured by TGA.
[c]As measured by Hot Disk.
[d]As measured by DMA.
[e]At 35°C, 1 barrer = 10^{-10} cm^3(STP) cm/cm^2 s cmHg.

lar weight distributions in all as-prepared composite materials.

3.2. Thermal properties

3.2.1. Thermogravimetric analysis

Figure 10 shows the thermal stabilities of the composite membranes determined by a thermogravimetric analyzer. Upon the addition of silica particles, all the composite membranes had higher thermal decomposition (T_d) temperatures than PANI membrane. Typically, the T_d values corresponding to the 10 wt% weight loss of the composite membranes shifted to higher temperature range with increasing mesoporous silica content, which confirms the enhanced thermal stability of the composite membranes, as shown in Figure 10 and Table 2. Moreover, with the same amount of silica particles, the PSM3 membrane showed higher T_d than PSN3 and PRSN3 membranes. Generally, PANI-silica membranes are expected to exhibit better thermal stability upon the incorporation of silica particles. The obvious differences in the increase in T_d (50.2°C increase for PSM3 membrane, 29.8°C for PSN3 membrane and 19.9°C for PRSN3 membrane) may be attributed to the following: each nano-scale AMS82 nanoparticle has abundant aniline groups on the surface and on the surface of internal pore channels. Therefore, the improvement in the thermal stability of the PSM membrane can be ascribed both to the good thermal stability of AMS and to the multilinkage that occurs between the PANI chains and AMS. Hence PANI chains not only bond to the surface of the AMS particles but also penetrate through the pore channels and are tethered to the channel surface.

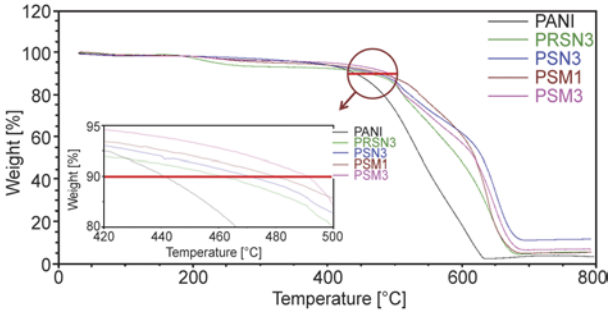

Figure 10. Thermal stabilities of the composite membranes

Moreover, the characteristic yield for all the PSM, PSN and PRSN membranes increases with respect to the AMS82 weight percentage. This may be due to the PANI main chains on the AMS surface and inside the AMS pores, as well as due to the fact that ARS and NRS surfaces are more difficult to decompose than PANI.

3.2.2. Thermal transport properties

In this study, the thermal transport properties of PSM, PSN and PRSN membranes measured by TPS technique are shown in Figure 11 and Table 2. For

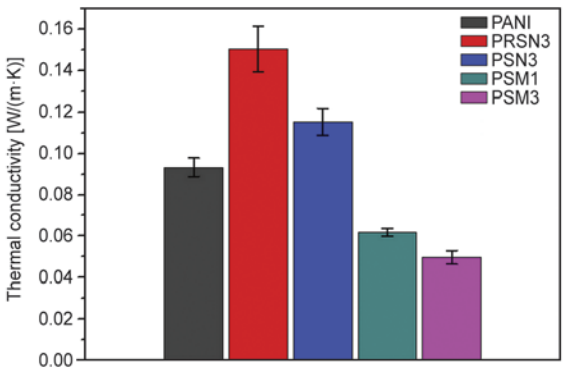

Figure 11. Thermal transport properties of the composite membranes

PSN and PRSN membranes, the incorporation of ARS and NRS particles in the PANI matrix revealed an obvious increase in thermal conductivity. For example, PANI exhibited thermal conductivity (k, W/(m·K)) of 0.0933 [38], which was lower than that of PSN and PRNS membranes. It should be noted that the k value of the PSM membrane containing 3 wt% of AMS particles was clearly lower than those of PSN3, PRSN3, and PANI membranes. This is probably attributed to the existence of pores/voids in the multilinkages between the PANI chains and the nanoscale internal channels of AMS particles, which may incorporate a relatively large amount of air (k = 0.029 at RT) [39] into the mesocomposite membranes, leading to the obvious decrease in the thermal conductivity [22].

3.3. Mechanical properties

To investigate the effect of silica and mesoporous silica on the mechanical properties of PSM, PSN and PRSN membranes, the composite membranes were studied by dynamic mechanical analysis (DMA). The storage modulus (E') curves for the composite membranes over the temperature range from 40 to 300°C are shown in Figure 12, and the results are listed in Table 2. It can be clearly seen that the incorporation of silica increased the E'. Near room temperature, the PANI membrane has lower E' (2610 MPa) than the composite membranes (>2720 MPa). With the same amount of silica particles, the membrane with incorporated mesoporous silica nanospheres (PSM3 membrane) shows the highest E' value compared with those with silica nanoparticles (PSN3 and PRSN3 membranes). The obvious difference in the mechanical strength enhancement of the membranes (27% for PSM3 vs. 16% for PSM3 and 4% for PRSM3 with AMS82, ARS82, and NRS82 particles in PANI, respectively) indicates that the reactive channel aniline groups of nanoscale mesoporous silica do show significant enhancement of the mechanical strength of as-prepared composites.

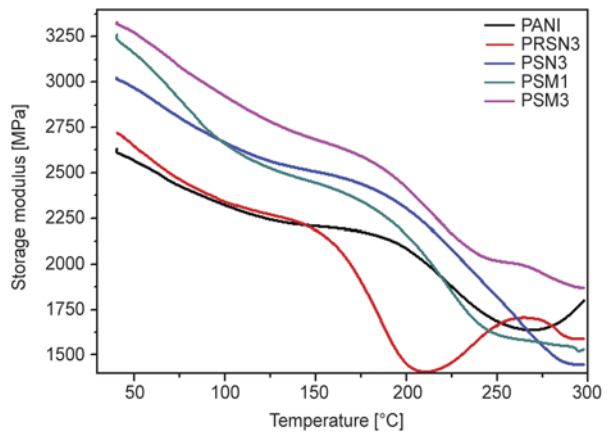

Figure 12. Mechanical properties of the composite membranes

3.4. Surface properties

To investigate the surface properties of the membranes, contact angle tests were carried out, and the results are given in Table 2. The measured contact angle of pure PANI was 90°. The contact angle of the composite membranes decreased with increasing mesoporous silica content. This trend is due to the relative hydrophilicity of mesoporous silica particles. With the same silica particle content, PSM3 membrane exhibited lower contact angle than PSN3 and PRSN3 membranes. This behavior was attributed to the different properties of silica particles, such as hydrophilicity and particle size.

3.5. Gas permeability properties

For the comparative studies on the gas permeability of PSM, PSN and PRSN membranes, gas permeability analysis (GPA) technique was used for measuring the permeability of gases such as O_2 and N_2. The gas permeability of various membranes is shown in Figure 13, and the results are listed in Table 2. The results show that when mesoporous silica particles were added, the permeability of the composite membranes showed an obvious increase from that of PANI membrane and increased with increasing mesoporous silica content. At the same silica loading, the permeability of PSM3 membrane for O_2 and N_2 was higher than those of PSN3 and PRSN3 membranes.

The selectivity of gas pairs (O_2/N_2) are also given in Table 2. In Table 2, the selectivity of the composite membranes shows a slight decrease over that of the

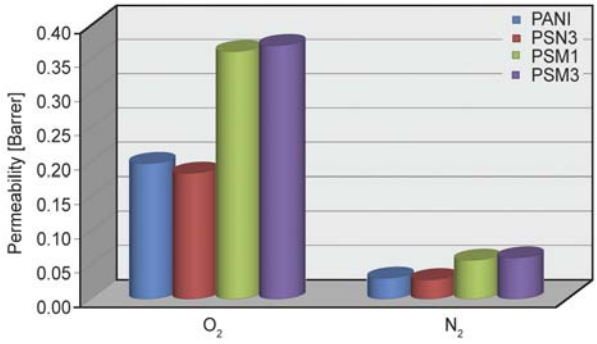

Figure 13. Gas permeabilities of the composite membranes

PANI membrane, as expected. This phenomenon could be attributed to the fact that some of the gas penetrants bypassed the silica particles completely in the MMMs because of the presence of voids, resulting in blocked passage through the silica particles.

4. Conclusions

In this study, conductive PSM, PSN and PRSN membranes have been prepared successfully. The dispersibility of silica particles in PANI matrix was observed by TEM. GPC was used for determining the molecular weights of as-prepared samples. The effect of material composition on the mechanical strength, thermal stability, thermal transport, surface and gas permeability properties of PSM, PSN and PRSN membranes were investigated by TGA, TPS technique, DMA, contact angle measurement, and GPA, respectively. It should be noted that at the same silica loading, PSM membranes exhibited better thermal stability (e.g., higher T_d), thermal insulation property (e.g., lower k), and mechanical strength (e.g., higher E'), as well as increased surface hydrophility (e.g., higher wettability of water droplets) and gas permeability as compared with those of PSN and PRSN membranes. The obvious differences in the physical properties of all composite membranes may be attributed to the presence of reactive channel aniline groups and unoccupied channel voids/pores in the nanoscale silica-based mesoporous materials.

Acknowledgements

We gratefully acknowledge the financial support of the Ministry of Education (MOE), Taiwan, R.O.C., NSC 101-2113-M-033-005-MY1, the Center-of-Excellence (COE) Program on Membrane Technology from MOE, R.O.C., the Department of Chemistry at Chung Yuan Christian University (CYCU) (CYCU-01RD-RA002-11235), the Center for Nanotechnology and Biomedical Technology at CYCU, and the Bureau of Energy, Ministry of Economic Affairs (MOEA), Taiwan, R.O.C., for its financial support under Contract 102-D0106.

References

[1] Schütz M. R., Kalo H., Lunkenbein T., Gröschel A. H., Müller A. H. E., Wilkie C. A., Breu J.: Shear stiff, surface modified, mica-like nanoplatelets: A novel filler for polymer nanocomposites. Journal of Materials Chemistry, **21**, 12110–12116 (2011).
DOI: 10.1039/C1JM11443C

[2] Nishida T., Obayashi A., Haraguchi K., Shibayama M.: Stress relaxation and hysteresis of nanocomposite gel investigated by SAXS and SANS measurement. Polymer, **53**, 4533–4538 (2012).
DOI: 10.1016/j.polymer.2012.07.038

[3] Hu X-L., Hou G-M., Zhang M-Q., Rong M-Z., Ruan W-H., Giannelis E. P.: A new nanocomposite polymer electrolyte based on poly(vinyl alcohol) incorporating hypergrafted nano-silica. Journal of Materials Chemistry, **22**, 18961–18967 (2012).
DOI: 10.1039/C2JM33156J

[4] Wang M. H., Ruan W. H., Huang Y. F., Ye L., Rong M. Z., Zhang M. Q.: A strategy for significant improvement of strength of semi-crystalline polymers with the aid of nanoparticles. Journal of Materials Chemistry, **22**, 4592–4598 (2012).
DOI: 10.1039/C2JM16097H

[5] Chen H., Zhang X., Zhang P., Zhang Z.: Facile approach in fabricating superhydrophobic SiO_2/polymer nanocomposite coating. Applied Surface Science, **261**, 628–632 (2012).
DOI: 10.1016/j.apsusc.2012.08.071

[6] Müller M. T., Krause B., Pötschke P.: A successful approach to disperse MWCNTs in polyethylene by melt mixing using polyethylene glycol as additive. Polymer, **53**, 3079–3083 (2012).
DOI: 10.1016/j.polymer.2012.05.041

[7] Tao F., Bonnaud L., Auhl D., Struth B., Dubois P., Bailly C.: Influence of shear-induced crystallization on the electrical conductivity of high density polyethylene carbon nanotube nanocomposites. Polymer, **53**, 5909–5916 (2012).
DOI: 10.1016/j.polymer.2012.10.026

[8] Liu T., Wood W., Li B., Lively B., Zhong W-H.: Effect of reinforcement on wear debris of carbon nanofiber/high density polyethylene composites: Morphological study and quantitative analysis. Wear, **294–295**, 326–335 (2012).
DOI: 10.1016/j.wear.2012.07.010

[9] Kohlman R. S., Joo J., Epstein A. J.: Physical properties of polymers handbook. American Institute of Physics, New York (1996).

[10] Trivedi D. C.: Handbook of organic conductive molecules and polymers. Wiley, New York (1997).

[11] Zhang L. J., Wan M. X., Wei Y.: Hollow polyaniline microspheres with conductive and fluorescent function. Macromolecular Rapid Communications, **27**, 888–893 (2006).
DOI: 10.1002/marc.200600134

[12] He H., Zhu J., Tao N. J., Nagahara L. A., Amlani I., Tsui R.: A conducting polymer nanojunction switch. Journal of the American Chemical Society, **123**, 7730–7731 (2001).
DOI: 10.1021/ja016264i

[13] Grgur B. N., Ristić V., Gvozdenović M. M., Maksimović M. D., Jugović B. Z.: Polyaniline as possible anode materials for the lead acid batteries. Journal of Power Sources, **180**, 635–640 (2008).
DOI: 10.1016/j.jpowsour.2008.02.022

[14] Milczarek G.: Electrocatalytic thin films based on nordihydroguaiaretic acid-functionalyzed polyaniline. Reactive and Functional Polymers, **68**, 1542–1548 (2008).
DOI: 10.1016/j.reactfunctpolym.2008.08.006

[15] Choi H. J., Kim J. W., To K.: Electrorheological characteristics of semiconducting poly(aniline-*co*-*o*-ethoxyaniline) suspension. Polymer, **40**, 2163–2166 (1999).
DOI: 10.1016/S0032-3861(98)00418-2

[16] Kim J. W., Kim S. G., Choi H. J., Jhon M. S.: Synthesis and electrorheological properties of polyaniline-Na^+-montmorillonite suspensions. Macromolecular Rapid Communications, **20**, 450–452 (1999).
DOI: 10.1002/(SICI)1521-3927(19990801)20:8<450::AID-MARC450>3.0.CO;2-N

[17] Klaysom C., Moon S-H., Ladewig B. P., Lu G. Q. M., Wang L.: The influence of inorganic filler particle size on composite ion-exchange membranes for desalination. The Journal of Physical Chemistry C, **115**, 15124–15132 (2011).
DOI: 10.1021/jp112157z

[18] Huang J., Zhang K., Wang K., Xie Z., Ladewig B., Wang H.: Fabrication of polyethersulfone-mesoporous silica nanocomposite ultrafiltration membranes with antifouling properties. Journal of Membrane Science, **423–424**, 362–370 (2012).
DOI: 10.1016/j.memsci.2012.08.029

[19] Suzuki N., Kiba S., Yamauchi Y.: Low dielectric property of novel mesoporous silica/polymer composites using smart molecular caps: Theoretical calculation of air space encapsulated inside mesopores. Microporous and Mesoporous Materials, **138**, 123–131 (2011).
DOI: 10.1016/j.micromeso.2010.09.020

[20] Suzuki N., Kiba S., Kamachi Y., Miyamoto N., Yamauchi Y.: Mesoporous silica as smart inorganic filler: Preparation of robust silicone rubber with low thermal expansion property. Journal of Materials Chemistry, **21**, 5338–5344 (2011).
DOI: 10.1039/C0JM03767B

[21] Romanes M. C., D'Souza N. A., Coutinho D., Balkus K. J., Scharf T. W.: Surface and subsurface characterization of epoxy-mesoporous silica composites to clarify tribological properties. Wear, **265**, 88–96 (2008).
DOI: 10.1016/j.wear.2007.08.022

[22] Huang K-Y., Weng C-J., Huang L-T., Cheng T-H., Wei Y., Yeh J-M.: Systematically comparative studies on the preparation and physical properties of PMMA–silica mesocomposite and nanocomposite membranes. Microporous and Mesoporous Materials, **131**, 192–203 (2010).
DOI: 10.1016/j.micromeso.2009.12.022

[23] Weng C-J., Huang K-Y., Chiu W-L., Yeh J-M., Wei Y., Liu S-P., Hwang S-S.: A comparative study of the preparation and physical properties of polystyrene–silica mesocomposite and nanocomposite materials. Polymer International, **60**, 1129–1135 (2011).
DOI: 10.1002/pi.3052

[24] Wei Y., Jin D., Ding T., Shih W-H., Liu X., Cheng S. Z. D., Fu Q.: A non-surfactant templating route to mesoporous silica materials. Advanced Materials, **10**, 313–316 (1998).
DOI: 10.1002/(SICI)1521-4095(199803)10:4<313::AID-ADMA313>3.0.CO;2-M

[25] Lowell S.: Introduction to powder surface area. Wiley, New York (1979).

[26] Cheng C-F., Cheng H-H., Cheng P-W., Lee Y-J.: Effect of reactive channel functional groups and nanoporosity of nanoscale mesoporous silica on properties of polyimide composite. Macromolecules, **39**, 7583–7590 (2006).
DOI: 10.1021/ma060990u

[27] Ying J. Y., Mehnert C. P., Wong M. S.: Synthesis and applications of supramolecular-templated mesoporous materials. Angewandte Chemie International Edition, **38**, 56–77 (1999).
DOI: 10.1002/(SICI)1521-3773(19990115)38:1/2<56::AID-ANIE56>3.0.CO;2-E

[28] Corma A.: From microporous to mesoporous molecular sieve materials and their use in catalysis. Chemical Reviews, **97**, 2373–2420 (1997).
DOI: 10.1021/cr960406n

[29] Barrett E. P., Joyner L. E., Halenda P. P.: The determination of pore volume and area distributions in porous substances. I. Computations from nitrogen isotherms. Journal of the American Chemical Society, **73**, 373–380 (1951).
DOI: 10.1021/ja01145a126

[30] Cho M. S., Choi H. J., Ahn W-S.: Enhanced electrorheology of conducting polyaniline confined in MCM-41 channels. Langmuir, **20**, 202–207 (2004).
DOI: 10.1021/la035051z

[31] Nishio E., Ikuta N., Hirashima T., Koga J.: Pyrolysis-GC/FT-IR analysis for silane coupling treatment of glass fibers. Applied Spectroscopy, **43**, 1159–1164 (1989).
DOI: 10.1366/0003702894203589

[32] Subramani S., Cheong I. W., Kim J. H.: Synthesis and characterizations of silylated polyurethane from methyl ethyl ketoxime-blocked polyurethane dispersion. European Polymer Journal, **40**, 2745–2755 (2004).
DOI: 10.1016/j.eurpolymj.2004.07.018

[33] Subramani S., Lee J. M., Lee J-Y., Kim J. H.: Synthesis and properties of room temperature curable trimethoxysilane-terminated polyurethane and their dispersions. Polymers for Advanced Technologies, **18**, 601–609 (2007).
DOI: 10.1002/pat.860

[34] Trchová M., Šeděnková I., Tobolková E., Stejskal J.: FTIR spectroscopic and conductivity study of the thermal degradation of polyaniline films. Polymer Degradation and Stability, **86**, 179–185 (2004).
DOI: 10.1016/j.polymdegradstab.2004.04.011

[35] Serrano D. P., Aguado J., Morales G., Rodríguez J. M., Peral A., Thommes M., Epping J. D., Chmelka B. F.: Molecular and meso- and macroscopic properties of hierarchical nanocrystalline ZSM-5 zeolite prepared by seed silanization. Chemistry of Materials, **21**, 641–654 (2009).
DOI: 10.1021/cm801951a

[36] Weng S., Lin Z., Zhang Y., Chen L., Zhou J.: Facile synthesis of SBA-15/polyaniline nanocomposites with high electrochemical activity under neutral and acidic conditions. Reactive and Functional Polymers, **69**, 130–136 (2009).
DOI: 10.1016/j.reactfunctpolym.2008.12.001

[37] Feng X., Yang G., Liu Y., Hou W., Zhu J-J.: Synthesis of polyaniline/MCM-41 composite through surface polymerization of aniline. Journal of Applied Polymer Science, **101**, 2088–2094 (2006).
DOI: 10.1002/app.23836

[38] Kaul P. B., Day K. A., Abramson A. R.: Application of the three omega method for the thermal conductivity measurement of polyaniline. Journal of Applied Physics, **101**, 083507/1–083507/8 (2007).
DOI: 10.1063/1.2714650

[39] Lu X., Nilsson O., Fricke J., Pekala R. W.: Thermal and electrical conductivity of monolithic carbon aerogels. Journal of Applied Physics, **73**, 581–584 (1993).
DOI: 10.1063/1.353367